Winter 12-15-2022

Functionalized Plasmonic Nanostructures for Ultrasensitive Single Cell Analysis

Priya Rathi
Washington University in St. Louis

WASHINGTON UNIVERSITY IN ST. LOUIS

Department of Chemistry

Dissertation Examination Committee:
Richard Loomis, Chair
Meredith Jackrel
Jeremiah J. Morrissey
Bryce Sadtler
Srikanth Singamaneni

Functionalized Plasmonic Nanostructures for Ultrasensitive Single Cell Analysis

by
Priya Rathi

A dissertation presented to
Washington University in St. Louis
in partial fulfillment of the
requirements for the degree
of Doctor of Philosophy

December 2022
St. Louis, Missouri

Table of Contents

List of Figures

List of Abbreviations

AFM	Atomic force microscopy
AuNPs	Gold nanoparticles
AuNRs	Gold nanorods
FTIR	Fourier-transform infrared spectroscopy
NIR	Near infrared
PBS	Phosphate-buffered saline
PDMS	Polydimethylsiloxane
SEM	Scanning electron microscopy
TEM	Transmission electron microscopy
UV-vis	Ultraviolet-visible
XPS	X-ray photoelectron spectroscopy
LSPR	Localized surface plasmon resonance
TMPS	Trimethoxypropylsilane
APTMS	(3-aminopropyl) trimethoxysilane,
XPS	X-ray photoelectron spectroscopy
ExM	Expansion microscopy

LSPR	Localized surface plasmon resonance
LOD	Limit-of-detection
BSA	Bovine serum albumin
ELISA	Enzyme-linked immunosorbent assay
FLISA	Fluorophore-linked immunosorbent assay
PEF	Plasmon enhanced fluorescence
EM field	Electromagnetic field
IL-6	Interleukin 6
LPS	Lipopolysaccharide
TNF-α	Tumor necrosis factor-α
ICC	Immunocytochemistry
IF	Immunofluorescence
CLSM	Confocal laser scanning microscopy
BMDCs	Bone marrow-derived dendritic cells
BMDMs	Bone marrow-derived macrophages
MEF	Metal enhanced fluorescence
SD	Standard deviation

Acknowledgments

I would like to express my deepest gratitude towards my advisor Dr. Srikanth Singamaneni for his unconditional support and guidance during my Ph.D. research at Washington University in St. Louis. I consider myself to be extremely lucky to have been a part of Dr. Singamaneni's group and worked on some of the most exciting and stimulating research projects throughout my Ph.D. I am grateful for Dr. Singamaneni's trust and belief in me for leading new projects and helping me push beyond my capabilities. I am thankful to my collaborators for providing insightful recommendations and directions: Prof. Baranidharan Raman, Prof. Parag Banerjee. I am sincerely thankful to my Ph.D. committee members: Dr. Richard Loomis, Dr. Bryce Sadtler, Dr. Meredith Jackrel for their valuable time and support during my research. I feel honored to be associated to the McDonnell International Scholars Academy, where I have met and engaged with the brightest minds from across the globe. I have learnt a great deal from the leaders at Washington University and MISA, for which I will forever be grateful.

I thank my fellow researchers for their continued support in conducting collaborative research. My research colleagues and friends in Soft Nanomaterials lab have been supportive in multiple ways – I especially thank Dr. Jeremiah Morrissey, Dr. Anushree Seth, Mr. Prashant Gupta, Dr. Zheyu (Ryan) Wang, Dr. Jingyi Luan, Dr. Qisheng Jiang, Dr. Sisi Cao, Dr. Brendan Watson, Dr. Rohit Gupta, Dr. Hamed Gholami Derami, Mr. Avishek Debnath, Ms. Yixuan Wang, Mr. Yuxiong Liu, Ms. Samhitha Kolla, Ms. Samyuktha Kolluru, Mr. Harsh Baldi and esteemed alumni.

I am grateful for the unconditional love and support from my parents, my families, and my husband, Dr. Girish Sharma who is my biggest cheerleader. Some of my closest friends in St. Louis and India have played an important role in my life, and I will always cherish our moments.

Priya Rathi

Washington University in St. Louis

December 2022

Dedicated to my parents and grandparents.

ABSTRACT OF THE DISSERTATION

Functionalized Plasmonic Nanostructures for Ultrasensitive Single Cell Analysis

by

Priya Rathi

Doctor of Philosophy in Chemistry

Washington University in St. Louis, 2022

Dr. Richard Loomis, Chair

Dr. Meredith Jackrel,

Dr. Jeremiah J. Morrissey

Dr. Bryce Sadtler,

Dr. Srikanth Singamaneni,

Ultrasensitive detection and quantification of soluble, secreted and cell surface-bound proteins is critical for advancing our understanding of cellular systems, enabling effective drug development, novel therapies, and bio-diagnostics. However, exiting technologies are largely limited by their sensitivity, making the detection and quantification of low-abundant proteins extremely challenging. This forms a major barrier in various fields of biology and biomedical sciences.

In this work, we introduce novel cellular analysis methodologies based on plasmon-enhanced fluorescence for analyzing cell structure and probing surface and secreted proteins from cells. In the first part, we introduce plasmon-enhanced expansion microscopy and demonstrate the effectiveness of employing an ultrabright plasmonic nanolabel in probing hippocampal neurons

and quantifying the morphological markers at high resolution. In the second part of this thesis, we introduce plasmon-enhanced FluoroDOT assay for ultrasensitive detection of cell secreted proteins. The plasmonic nanolabels enabled significantly improved signal-to-noise ratio compared to conventional fluorophores, therefore enabling detection and quantification of cell secreted proteins at extremely low concentrations of chemical or biological stimuli. In the third part, we establish plasmon-enhanced flow cytometry as a novel methodology to probe and analyze cellular surface proteins, enhancing the sensitivity of the approach in delineating cell populations with different protein levels. Overall, we establish the proof-of-concept for various plasmon-enhanced cellular analysis and biodetection methods that can be potentially useful in advancing the field of biological and biomedical sciences.

Chapter 1: Introduction

.

1.1 Background and motivation

1.1.1 Plasmon-enhanced fluorescence

Fluorescence-based bio-detection technologies are one of the most widely used methodologies employed for understanding biological systems including biomolecules, sub-cellular organelles, cells, and tissues.[1] For example, fluorescence-based methodologies such as immunoassay, immunofluorescence, fluorescence in-situ hybridization, expansion microscopy, flow cytometry, etc. are routinely employed in a wide range of biological and life science studies.[1-4] Although broadly applied, conventional molecular fluorophores often suffer from weak fluorescence signal and poor stability. Therefore, designing ultrabright fluorescent nanolabels that are compatible across multiple biodetection platforms will transform the field of fluorescence-based technologies for biomedical applications.

Owing to their unique optical properties, metal nanostructures are known to greatly enhance the fluorescence emission from organic and inorganic emitters that are in proximity to their surface.[5] Specifically, the localized surface plasmon resonance of the metal nanostructures enhances the excitation field and the radiative decay rates of the fluorophores, both of which enhance the fluorescence signal.[6] Therefore, interactions between surface plasmon on metallic nanoparticles and fluorophores is observed to lead to a decrease in fluorescence lifetime (increase in quantum yield), increased photostability, and increased spontaneous emission rate.[7]

Metal-enhanced fluorescence can be harnessed to improve the sensitivity of fluorescence-based bioassays[5,6,8]. Therefore, a wide range of novel nanomaterials based on metal-enhanced

fluorescence have been explored as biosensing plasmonic substrates enabling fluorescence enhancement and reduction in background signal intensities[9,10]. For example, surface plasmon resonance-based biosensors have been developed and employed for sensitive and specific detection of RNA, DNA, bacteria, small molecules, and chemical analytes[9,11-15]. Despite these achievements, plasmonic-enhanced fluorescence has been limited to substrate-bound detection methodologies, therefore there is an imminent need for designing colloidally stable plasmonic fluorescent nanostructure exhibiting excellent fluorescence, photostability and sensitivity. Such a novel ultrabright plasmonic nanolabel would be applicable to wide range of cellular analysis including bioassays, fluorescence microscopy, and flow cytometry. Though these methodologies are routinely employed to investigate cellular structures for surface, cytoplasmic or secreted proteins, most of them suffer from weak fluorescence readout, poor sensitivity, high variability, and ineffective integration with rare cell populations[16-18]. Therefore, ultrabright nanostructures offering feasible integration with a wide range of biodetection techniques are considered to be valuable.

1.1.2 Single cell analysis

Sensitive and precise investigation of physiological and pathological processes including cellular processes such as signaling, activation, differentiation, etc. and cell-cell interactions is essential for understanding biological systems.[19] Single cell analysis is of critical importance in understanding cellular heterogeneity, characterizing cells, and quantifying sub-populations for designing novel diagnostic tools and therapies. Cellular studies encompass visualization via fluorescence-based microscopy imaging, cell sorting and analysis via flow cytometry and

DNA/RNA sequencing assays, providing an insight into the cell-cell interactions, interfaces, and environments.[16,20]

Systematic investigation of cellular heterogeneity in DNA, proteins, and metabolites has been instrumental in identification of previously unknown cell populations, advancing the field.[21-23] For example, detection of biomarkers in peripheral fluids, and proteins secreted by cells or expressed on cell surface offer a unique insight into cell-to-cell heterogeneity that drives cellular processes.[24-26] However, identification and quantification are challenged by the limited understanding of cell surface proteome. Moreover, the expression of cell proteome can range from <100 copy numbers per cell to >10,000 copy numbers per cell highlighting the variability in protein abundance, often correlated to their function.[27] Therefore, low-abundant cellular proteins are often disregarded in commonly employed methodologies including fluorescence microscopy, ELISA, mass spectrometry, flow cytometry, and ELISpot owing to their poor sensitivity in delineating small differences between cell subpopulations expressing differential levels of protein biomarkers. Moreover, cellular analysis faces the pertinent challenge of low throughput forbidding the analysis of millions of cells and therefore bypassing rare cell populations.

Though fluorescence-based bio-detection has enabled improved visualization of cellular structures by tagging them with fluorescent nanolabels, several challenges remain persistent. The qualitative and quantitative analysis of biological specimens is impeded using weak fluorophores, insufficient labeling, and high background autofluorescence signal, in addition to the poor sensitivity of conventional tools. For example, conventional Recent advancements in technology and novel computational insight have resulted in high-resolution techniques including cytometry by time-of-flight (CyTOF), super-resolution microscopes (e.g., STED,

STORM, MINFLUX), however require long analysis times and lack in sensitivity, ease of availability, and low throughput.[28-31] Therefore, analyzing cells at singular level necessitates the use of powerful tools that must encompass bright fluorescent nanolabels, sensitive detection and analysis platforms, and advancements in computational expertise.

1.2 Research goals and objectives

This research aims to harness metal-enhanced fluorescence in plasmonic nanostructures to establish novel nanolabels and overcome limitations associated with conventional fluorophores for high-resolution imaging and analysis of cellular systems. Toward this goal, we have pursued the following three main objectives: 1) Introduce plasmon-enhanced expansion microscopy to overcome the signal dilution associated with conventional fluorophores; 2) Introduce plasmon-enhanced FluoroDOT assay for ultrasensitive and high-resolution imaging of cell-secreted proteins; 3) Introduce plasmon-enhanced flow cytometry for ultrasensitive detection and quantification of cell surface antigens via. Taken together, these sensitive and specific methodologies may be applicable in probing a wide variety of cellular systems, further advancing the field of biological and molecular sciences. We have accomplished several specific technical tasks noted below to realize these objectives.

1.2.1 Objective 1

Introduce plasmon-enhanced expansion microscopy to overcome the signal dilution associated with conventional fluorophores

Task 1: Introduce ultrabright plasmonic nanostructure as a universal fluorescent nanolabel in expansion microscopy (ExM)

Task 2: Validate the compatibility of plasmonic-fluors in ExM.

Task 3: Determine the improvement in the quantification of morphological maturation parameters of neurons using plasmon-enhanced ExM (p-ExM).

1.2.2 Objective 2

Introduce plasmon-enhanced FluoroDOT assay high-resolution imaging and quantification of cell-secreted proteins

Task 1: Compare the brightness and signal-to-noise ratio of plasmonic-fluors to conventional fluorophores as nanolabels in cell secretion assay.

Task 2: Demonstrate multiplexed FluoroDOT assay for simultaneous detection and quantification of multiple secreted proteins.

1.2.3 Objective 3

Introduce plasmon-enhanced flow cytometry for ultrasensitive detection and quantification of cell surface antigens

Task 1: Determine the improvement in bioanalytical parameters of plasmon-enhanced flow cytometry compared to conventional flow cytometry using BMDCs as a model system

Task 2: Design and optimize antibody-conjugated plasmonic-fluor for multiparameter flow cytometry

Chapter 2: Plasmon-enhanced expansion microscopy

2.1 Introduction

Understanding the structure and structure-function relationships at various length scales is of paramount importance in various fields of biology and life sciences. Optical microscopy is one of the most commonly used techniques to probe the structure and function of biological systems. The resolution of conventional optical microscopes, largely governed by the wavelength of the light, refractive index of the surrounding medium and the numerical aperture of the lens, is often limited to ~250 nm[32,33]. Electron microscopes, on the other hand, can achieve a spatial resolution of a few Å, which enables the visualization of ultra-fine structural details of cellular and sub-cellular structures[34]. However, the sample preparation for electron microscopy is complex, involving fixation to stabilize the sample under high vacuum, microtoming to achieve thin sections for electron penetration, and staining for better visualization. Additionally, electron microscopy imaging often involves long imaging and analysis times resulting in low throughput and can be very expensive.

Advances in optical microscope technology, detection methods, and novel computational methodologies led to the advent of super-resolution microscopy techniques such as stimulated emission depletion (STED) microscopy, stochastic optical reconstruction microscopy (STORM), and minimal photon fluxes (MINFLUX), which allow spatial resolution below the diffraction limit of light[29,35,36]. For example, STED microscopy works by reducing the excitation volume that minimizes the area generating fluorescence and introducing a donut-shaped laser beam that

selectively quenches the fluorescence from surrounding regions through stimulated emission depletion[29,35,37]. Therefore, only molecules at the center of the donut beam will emit light resulting in a higher resolution image, overcoming diffraction-limitation. STORM involves stochastically turning on specific fluorescent molecules within the diffraction-limited volume at specific time points, therefore unraveling the molecular localization over time and generating a super-resolution image[30,38]. MINFLUX combines fundamental approaches from STED and STORM, enabling high precision and high-resolution imaging[31,39]. These powerful imaging tools overcome the optical diffraction limit with a spatial resolution of ~20-120 nm[36,40]. However, limited availability of these tools (often in centralized facilities), low throughput, and longer imaging and analysis time scales hinder their wide-spread and routine use.

Expansion microscopy (ExM) is a super-resolution technique compatible with existing optical microscopes that has received wide attention, since its introduction in 2015[4,41]. ExM is based on the physical expansion of fluorophore-labeled biological specimens anchored to a swellable polymer gel, enabling ~70 nm lateral resolution[4,41]. The simple, inexpensive, and accessible nature of ExM has allowed biology and biomedical researchers to rapidly adopt this method and develop modified versions for their specific needs[42-44]. ExM relying on conventional molecular fluorophores suffers from significant degradation in fluorescence intensity (>50%) following the expansion process owing to (i) degradation of fluorescent dye when treated with proteinase K during digestion step in ExM protocol; and (ii) the physical expansion as a result of ExM, which results in the dilution of the fluorescence signal[41,45,46]. This reduction in the volumetric density of fluorophores significantly diminishes the quantitative and qualitative applications of ExM. In addition, commonly used fluorophores such as Alexa fluor 647 and Cy5 are known to be completely damaged during ExM process, precluding their use in ExM.[4,41] These considerations

highlight the need for ultrabright fluorescent labels in ExM that can mitigate the signal dilution challenges and promote more widespread adoption of the technology.

Here, for the first time, we demonstrate plasmon-enhanced expansion microscopy (p-ExM) by harnessing an ultrabright, fluorescent nanolabel, called plasmonic-fluor (PF). We investigate the compatibility of PFs with the ExM and stability of individual PFs against signal dilution after sample expansion. We also show the high fidelity and isotropic expansion of the sample comprised of hippocampal neurons labelled with PFs. p-ExM enabled improved spatial resolution and more accurate quantification of morphological parameters of the neuronal network compared to conventional confocal fluorescence microscopy. P-ExM complements conventional ExM (relying on molecular fluorophores) in overcoming the challenges associated with signal dilution and imaging low abundant cell surface markers.

2.2 Results and discussion

We have recently introduced an ultrabright nanoconstruct termed a plasmonic-fluor that exhibits ~7000-fold brighter fluorescence signal compared to its conventional counterpart[47]. Plasmonic-fluor is comprised of a plasmonic nanostructure as a fluorescence enhancer, molecular fluorophores as light emitters, a polymer spacer layer to avoid metal-induced quenching of the fluorescence, and bovine serum albumin (BSA) on the surface to minimize non-specific binding in bioassays, and a universal bio-linker (e.g., biotin, streptavidin) (**Fig. 1A**). We have demonstrated that plasmonic-fluors can replace conventional molecular fluorophores in various bioassays to enable nearly 1000-fold improvement in the limit-of-detection without significantly changing the workflow or read-out devices[25,26,47,48]. Plasmonic-fluors can be realized with any molecular fluorophore of choice by tuning the localized surface plasmon resonance (LSPR) wavelength of the plasmonic nanostructure to match the excitation/emission wavelength of the

fluorophore[25,47]. As such, plasmonic-fluors can be designed and synthesized to emit over a broad range of electromagnetic wavelength.

In this study, we harnessed negatively charged plasmonic-fluors comprised of IR-650 (called PF-650 henceforth) to demonstrate plasmon-enhanced expansion microscopy[49]. It has been previously reported that negatively charged nanostructures, irrespective of their size, shape and composition, specifically bind to neurons[50]. Plasmonic-fluor-650 is realized using Au@Ag nanocuboids with LSPR wavelength at ~650 nm as plasmonic nanoantenna (**Fig. 1B**). The resulting PFs are negatively charged with a ζ-potential of -28 ± 3 mV, owing to the presence of BSA on the outer surface (Fig. S1). Transmission electron microscopy (TEM) image shows PF-650 with a length of 110 ± 7 nm and a width of 62 ± 3 nm (**Fig. 1D**).

Briefly, expansion microscopy (ExM) protocol comprises of labeling biological specimens and anchoring them to a swellable polyelectrolyte gel, which when exposed to water, undergoes uniform physical expansion resulting in physical separation between labeled biomolecules[4,41]. We harnessed the specific interactions between the negatively charged PFs and hippocampal neurons to realize plasmon-enhanced expansion microscopy (**Fig. 1E**). Neuronal culture labelled with PFs, immunostained and fixed is introduced to an anchoring molecule (Acryloyl-X) in the first step of ExM (**Fig. 1F**). The anchor covalently binds with the tagged biomolecules and PFs. Subsequently, the PF-labelled neurons are exposed to a swellable polyelectrolyte gel precursor solution comprised of monomer precursors (sodium acrylate, acrylamide), cross-linker (N-N'methylenebisacrylamide), free-radical initiator (ammonium persulfate) and accelerator (tetramethylethylenediamine) resulting in the formation of a crosslinked polymer network[4,42]. Next, the polymer network-sample composite is subjected to proteinase K solution that cleaves non-anchored regions in the PF-labeled neuron sample to ensure isotropic expansion and

homogenization. Finally, the homogenized polymer network sample is immersed in water, resulting in swelling and isotropic physical expansion of the PF-hydrogel.

Conventional molecular fluorophores such as DyLight 405, AF546, and CF633 and fluorescent proteins such as GFP exhibit ~50% loss of fluorescence after subjecting to ExM protocol[4,41,45]. In some cases such as AF647 and Cy5, proteinase K digestion causes severe degradation of the fluorophores, forbidding their use in ExM[41]. Hence, it is important to probe the compatibility of PF with ExM protocol. To quantify the fluorescence retention of PFs following ExM protocol, PF-650 were sparsely immobilized on glass coverslip using biotin-streptavidin interaction (see Experimental section). Confocal fluorescence microscopy images revealed bright fluorescence signals from sparsely adsorbed individual PF-650 (**Fig. 2A, B**). Scanning electron microscopy imaging confirmed the uniform and sparse distribution of individual PF-650 on the surface (**Fig. 2C**). Glass coverslip substrate with such sparse distribution of PFs were subsequently subjected to standard expansion protocol and imaged using confocal microscope (**Fig. 2D, E**). We quantified the fluorescence signal retention by comparing the signal-to-noise ratio (SNR) in pre-ExM and post-ExM conditions. The SNR PF-650 was found to be 515 ± 52 in pre-ExM and 433 ± 45 in post-ExM conditions (**Fig. 2F**). The post-ExM fluorescence intensity accounts to nearly 85% retention in fluorescence signal, which confirms their applicability as labels in ExM. In contrast to many conventional molecular fluorophores, the PFs retained nearly 85% of the fluorescence signal after ExM protocol. This large retention of the fluorescence signal of PFs can be ascribed to the unique design of the fluorescent nanoconstruct in which the molecular fluorophores are protected against the harsh (bio)chemical conditions during gelation and swelling by the BSA coating.

Following the sample expansion, as expected, we noted a larger physical separation between PFs immobilized on the glass coverslip. It is worth noting that the fluorescence signal from PFs is not spatially diffused after ExM process as the molecular fluorophores are conjugated to the polymer spacer on the plasmonic core and remain intact after the ExM process. PFs serve as "digital nanolabels" allowing digitization of fluorescence signal from individual PFs.[26] Overall, excellent stability of fluorescence signal and localization of fluorescence signal of PFs after ExM makes them attractive nanolabels for ExM.

Next, we set out to demonstrate plasmon-enhanced ExM using PF-labeled hippocampal neurons wherein PFs specifically and spontaneously bind to neruons in a maturation-dependent manner (**Fig. 3, S2**).[49,50] SEM imaging revealed random orientations of PFs on the soma, and higher alignment along the length of neurites (**Fig. 3A**)[49]. As expected, we observed bright fluorescence signal from PFs adsorbed on the neuronal cell body and neurites with minimal background, indicating the specific binding of PFs to neuronss (**Fig. 3B**). Following the ExM procedure, confocal microscopy images revealed excellent retention of the structural details across a large sample size (~ 500 x 500 μm^2 in pre-ExM scale) (**Fig. 3C, E**). We observed a remarkable correlation of PF-labelled neurons in post-ExM with pre-ExM conditions over dimensions of 5300 X 2500 μm^2 (Fig. S2). Owing to the high density of PFs along the neurites, zoomed-in images of the neurites in the pre-ExM state showed a diffuse and continuous fluorescence signal along the neurites (**Fig. 3D**). On the other hand, zooming into the same region of interest in the post-ExM image revealed highly resolved individual PFs (**Fig. 3E**). In contrast to the pre-ExM image, the cross-sectional profile across the neurites obtained from the post-ExM image exhibited three distinct fluorescence signal peaks (**Fig. 3E, F**).

Next, we set out to determine the fidelity of p-ExM images by performing registration and distortion analysis, which provides quantitative correlation between pre-ExM and post-ExM images. We identified ~100 μm^2 arbitrary region on a PF-labelled neurons in pre-ExM and post-ExM images (**Fig. 3 A-D**). Using Elastix, we first performed a similarity transformation on post-ExM image to be matched and aligned to pre-ExM through iterations of isotropic scaling, rotation, and translation along the x- and y- directions (Figure S4)[42]. By incorporating the scaling factor derived from similarity registration in Elastix, we determined the corrected expansion factor (physical magnification factor) to be 4.0 ± 0.2 X (n=4), which closely matches with the established protocols[4,41]. Next, we performed a non-rigid b-spline transformation to further correct local deformations in the similarity-transformed post-ExM for better alignment with the pre-ExM condition (**Fig. 4E**). Subsequently, we plotted the distortion vector field between pre-ExM and post-ExM (**Fig. 4F-I**). We noted an excellent overlap between pre-ExM and transformed post-ExM images, highlighting the need for minimal deformation correction (Figure S5). The RMS error quantification revealed distortions of ~1.5 μm over length scales up to ~100 μm, corresponding to ~1.5% error (**Fig. 4J**).

As demonstrated above, PFs are highly compatible with ExM and exhibit excellent fluorescence retention and p-ExM offers a significant improvement in the spatial resolution compared to conventional confocal fluorescence microscopy. Building on these results, we set out to harness the improved spatial resolution of p-ExM to identify the previously unresolved fine structure of neurons and neural network. Towards this goal, we employed the filament tracer module in IMARIS software (Oxford Instruments) to quantify the morphological parameters of the neurons. We performed filament tracking analysis on pre-ExM and post-ExM images of the same set of PF-labelled neurons (n=5) (**Fig. 5A, D**). Filament tracking revealed a higher density of filaments

in post-ExM image compared to the pre-ExM image (**Fig. 5B, E**). Zoomed-in images reveal the improved spatial resolution offered by ExM, which enabled improved delineation of the fine neuronal features and analysis of the morphological parameters (**Fig. 5C, F**). We observed a significant increase in the total neurite length, total neurite area, and the number of neurite terminals in the post-ExM condition, indicative of the higher density of filaments being tracked and recognized (**Fig. 5G-I**). A 4-fold expansion of the sample led to nearly 1.7-fold increase in total neurite length and nearly 6-fold increase in total neurite area in post-ExM condition. We observed ~2.5-fold increase in the number of neurite terminal points in post-ExM condition owing to enhanced resolution. As opposed to ExM with conventional fluorophores that suffers from severe signal dilution, the fluorescence signal of individual plasmonic-fluors remains undiluted, thus enabling improved quantification of the morphological parameters. These results highlight the efficacy of p-ExM in tracing and mapping the structure of neurons and neuronal networks.

One of the important considerations in using bulky nanoparticles as labels is their slower diffusion compared to conventional molecular fluorophores, which prevents efficient labeling (**Fig. 6A**)[51,52 53]. The characteristic diffusion coefficient (D) relates inversely with the nanolabel size, therefore the use of bulky nanolabels leads to slower diffusion and the formation of a depletion zone immediately above the surface, consequently poor binding kinetics on the surface [54]. Therefore, on-surface bioassays and immunohistochemistry labeling often require significantly longer incubation times. To address diffusion limitations associated with the bulky nature of PFs and improve labeling efficiency of PFs in neuron cell culture, we adapted recently introduced cyclic draining and replenishment (CDR) method (**Fig. 6A**)[55]. Briefly, the substrate with the neuronal network is rotated during the PF labeling step resulting in cyclical draining and

replenishing of the PFs at the surface. After each CDR cycle, the concentration of the PFs at the neuronal surface is replenished to the bulk concentration of nanolabels, thus overcoming the depletion zone and accelerating the labelling process. We exposed the neural culture to PFs for different durations (2, 5, and 10 min) under static and rotation conditions. The ensemble fluorescence intensity was observed to increase by ~37% for 2 minutes, ~44% for 5 minutes, and ~83% for 10 minutes of rotational incubation when compared with static conditions (**Fig. 6B**). With an increase in the incubation time, we observed a rapid increase in the fluorescence from PF-labelled neurons in the rotation condition (**Fig. 6C-H**).

2.3 Conclusion

In conclusion, we introduced plasmon-enhanced expansion microscopy by harnessing the recently introduced PFs as nanolabels in expansion microscopy. Plasmonic-fluors, which are nearly 10,000-fold brighter compared to corresponding conventional fluorophores, exhibited excellent compatibility with expansion microscopy protocol. In contrast to most conventional molecular fluorophores, PFs retained nearly 85% of the fluorescence signal after gelation and swelling steps of ExM. We demonstrate that individual PFs that can be easily imaged using conventional epifluorescence microscopes are not prone to signal dilution, making them attractive digital nanolabels in ExM. Harnessing the selective binding of the negatively charged PFs to hippocampal neurons, we demonstrate the high fidelity of p-ExM over large areas of the sample. p-ExM enabled better visualization and analysis of the morphological features of the neural network as evidenced by the nearly 2.5-fold increase in the number of neurite terminal points identified by the filament tracking analysis. In addition to the passive labeling of the neurons harnessed here, antibody-conjugated PFs can serve as powerful nanolabels for imaging and analyzing low-abundant and sparsely dispersed cell surface markers, which cannot be

imaged using conventional molecular fluorophores due to their weak fluorescence signal. The high fidelity of p-ExM and remarkable uniformity of sample expansion makes this methodology attractive for probing the structure of neurons and neural networks.

2.4 Experimental section

Materials

Bovine serum albumin (BSA >98%, A7030), paraformaldehyde (PFA), 0.1% (w/v) poly-L-lysine (P982), triton X-100 (X-100), EDTA, disodium (E5134), tris(hydroxymethyl)aminomethane hydrochloride (Tris.Cl), sodium chloride (NaCl, S9888) were acquired from Sigma. NHS-PEG4-biotin, mouse anti-MAP2 primary antibody (2 µg/ml, monoclonal, MA5-12826) and Alexa Fluor 568 labelled Donkey anti-Mouse secondary antibody (2 µg/ml, A10037), 6-((acryloyl)amino)hexanoic acid, succinimidyl ester (acryloyl-X, SE 5 mg A20770), tetramethylethylenediamine (TEMED, 17919), ammonium persulfate (APS, 17874), proteinase-K recombinant (EO0492) were acquired from Thermo Fisher Scientific, USA). Sodium acrylate (R624) was acquired from AK Scientific. Acrylamide (1610140), N, N'-methylenebisacrylamide (1610201) were acquired from Bio-Rad.

Cell culture and nano-neuro interaction

All procedures have been approved by the Institutional Animal Care and Use Committee (IACUC) at Washington University in St. Louis. Briefly, hippocampal tissues were isolated from day E18 embryos of pregnant Sprague Dawley rat brains (Charles River, USA) and the isolated neurons were cultured as previously described[49]. Glass-bottom petridish were used for expansion microscopy experiments. 24-well polystyrene plates were used for studying labeling efficiency of PF under static vs rotational condition.

PF-650 with IR-650 dye were provided by Auragent Bioscience, MO, USA. The PFs were synthesized according to previously described procedure with slight modifications[47]. Negatively charged PF-650 dispersed in NbActiv4 medium were added to neuron culture on DIV 20 and later at a final concentration of O.D. ~5 and incubated for 1 hour at 37^{o}C and 5% CO_2. The cells were then fixed with PFA for 30 minutes, followed by washing with PBS three times. The nucleus was stained using DAPI as previously described[49].

Protocol for plasmon-enhanced expansion microscopy (p-ExM)

PF-labelled neuron cells after fixation and immunostaining on glass-bottom Petri dish were incubated with Acryloyl-X SE (0.1mg/mL in 1X PBS) for 1 hour at room temperature (RT) and overnight in 4 ^{o}C fridge. Prior to gelation step, samples were washed 2 times with fresh 1X PBS, with each wash lasting 15 minutes. In preparation for gelation step, Stock X, APS and TEMED were thawed and chilled in ice. The gelation solution was prepared by mixing Stock X, water, TEMED stock solution and APS stock solution in the ratio of 47:1:1:1 for a total of 150 µl to fabricate the gel in glass-bottom petridish. The solution was gently vortexed for 1-2 seconds and quickly added on top of the sample region. A coverslip wrapped in fresh, clean parafilm was gently placed on top of the sample region to prevent evaporation. Gelation step was allowed to proceed for 2 hours at 37^{o}C. Following the formation of gel, the Petri dish was filled with 3 ml of digestion buffer comprising of freshly added ~8mg/mL Proteinase K. Digestion was allowed to occur for overnight (>8 hours) at RT. Post-digestion, gels were transferred to larger Petri dish and immersed completely in water for a total of 2 hours, including 3-4 exchanges of water until expansion was complete. For post-ExM imaging and to prevent gel from slipping, the sample gels were mounted on glass slide coated with 0.1% (w/v) poly-L-lysine (PLL) solution. PLL was

drop-casted on clean glass slides and set aside for 20 minutes, followed by rinsing with water and drying with N_2 flow. The gel was then transferred to PLL-coated glass slide for confocal microscopy and imaging.

Confocal fluorescence microscopy

Specimens in pre-ExM and post-ExM conditions were imaged using BioTek Lionheart FX Automated Microscope with 10X objective. The imaging conditions were kept constant throughout the analysis of each specimen.

Material characterization

Transmission electron microscopy (TEM) micrographs were acquired using JEOL JEM-2100F field emission microscope. A drop of PF-650 aqueous dispersion was casted and dried onto a copper grid (Carbon Type-B, 200 mesh, Ted Pella, USA). The extinction spectra of plasmonic nanostructures were recorded using Shimadzu UV-1800 spectrophotometer. The zeta potential measurements were performed using Malvern Zetasizer (Nano ZS). Large area fluorescence images were obtained using LI-COR Odyssey CLx imaging system. Scanning electron micrographs (SEM) were acquired using a JEOL JSM-7001 LVF Field Emission scanning electron microscope. SEM images of PF-labelled neuron cells were acquired according to previously described procedure[49].

Determining the fidelity of p-ExM using Elastix

We used Elastix via a custom-written Python script for understanding the effect of PF on ExM by determining the correct expansion factor and analyzing expansion-associated distortions[42]. We first identified specific regions of interest from a large-scale pre-ExM and post-ExM image

for analysis through Elastix. Pre-ExM image was interpolated to achieve the estimated expansion as seen in post-ExM image. Gaussian blur was applied to the post-ExM image to remove the disparity between pre- and post-expansion images (blur size = 2.5). Next, similarity transformation was performed on blurred post-ExM image that modified four degrees of freedoms (DOF), namely expansion factor, rotation, translation in x, and translation in y. Therefore, it compensated for the isotropic scalation and location mismatch between the images. Any remaining distortions in the output of similarity transformation result were further subjected to non-rigid b-spline registration, to be matched and aligned to pre-ExM. Finally, the B-splined transformed points were used to generate the distortion maps between the pre-B-spline and post-B-spline images.

RMS error is defined as the absolute value of the difference of the distance between a pair of points in pre-ExM and the distance between same pair of points in post-ExM[4,42]. To calculate the RMS error, a set of coordinates were generated from the binary skeleton of the pre-ExM image using a gaussian blur. Then the points were deformed using custom-written Python script for Transformix and distance between the same sets of points were calculated. To create deformation vector plot, the x-y coordinates from b-spline registered image were plotted at the interval of 10 pixels[42].

Neuronal filament tracing in pre-ExM and post-ExM using IMARIS

Confocal fluorescence images of specific regions of interest were analyzed using filament tracer module in the IMARIS software (Oxford Instruments) using the Cy5 channel (PF-650). The analysis was performed on sparsely located neuron cells. The starting soma point of the neurons were detected by adjusting starting point threshold or provided manually to ensure the inclusion

of the specific cell analyzed or remove extra starting points. Next, the seeding points were provided by adjusting the seeding points that allow the tracing of all neuronal processes. The inclusion of background noise could give rise to erroneous neuronal processes; therefore, the thresholds were readjusted to achieve the best fit. For each cell studied in pre-ExM and post-ExM condition, we recorded morphological parameters for quantification (viz. filament length, filament area, and number of terminal points).

Static vs rotation incubation of neurons with plasmonic-fluors

DIV 21-25 neuron cells seeded on 24-well plates were labeled with PF-650 (as described above) for durations of 2 minutes or 5 minutes or 10 minutes, either under static condition or under rotation condition. PF-labeled neuron cells were fixed as per previously described methodology[49]. To place the 24-well plate under rotation, care was given to properly seal and separate the wells to prevent spillage. Rotation step was performed using a standard rotatory shaker (8 rotations per minute).

2.5 Figures

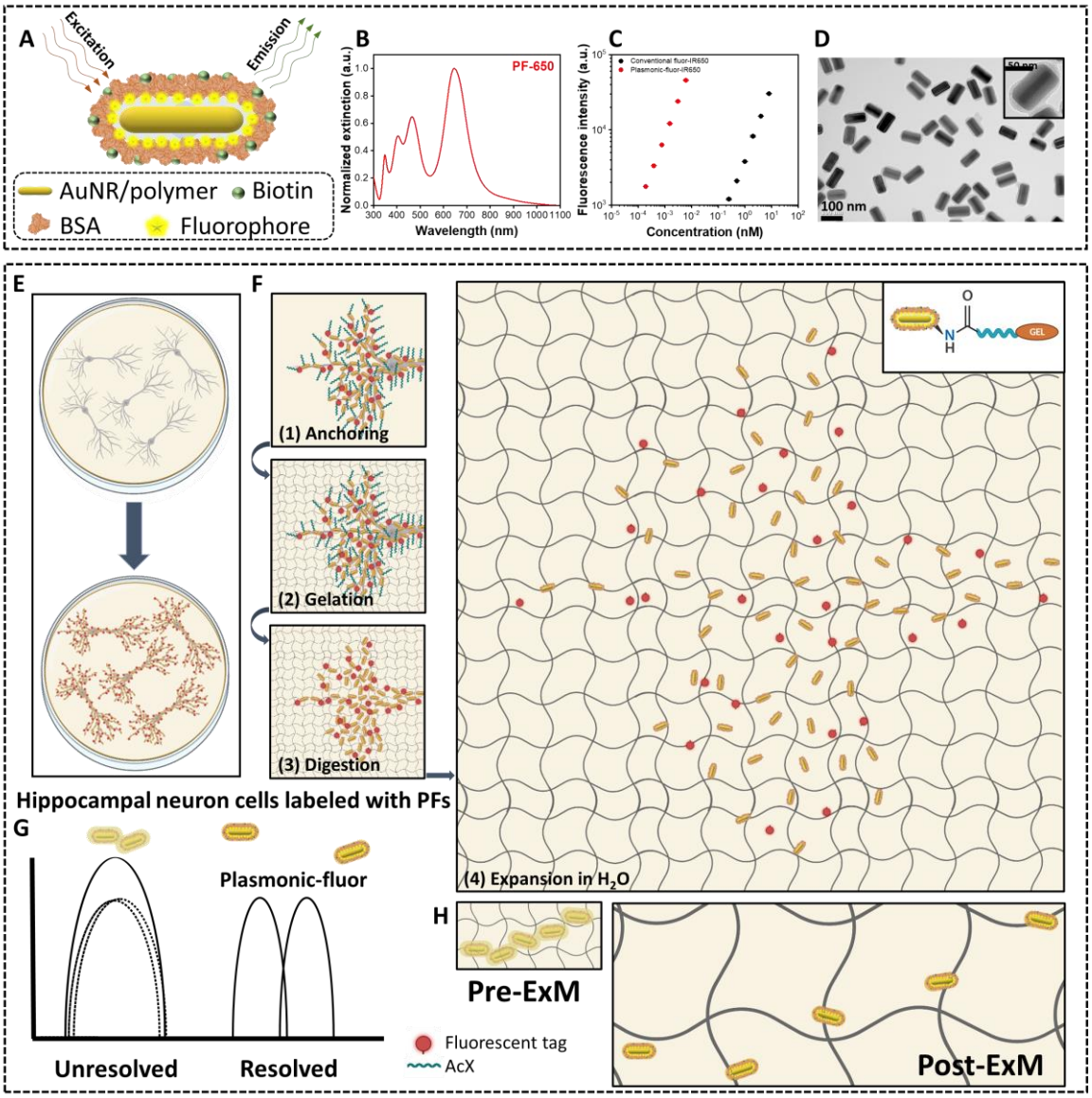

Figure 2.1 Plasmon-enhanced expansion microscopy. (**A**) Schematic illustration of PF-650 composed of plasmonic nanostructure (Au@Ag nanocuboid), spacer layer, and BSA-biotin-dye conjugate (IR-650), (**B**) Visible-NIR spectra of PF-650, (**C**) Fluorescence intensity of conventional-fluor-IR650 and PF-650 at different molar concentrations. The difference in slope of the two curves indicates that a single PF-650 is 1500-fold brighter than conventional-fluor-IR650. (**D**) TEM image of PF-650 with inset image showing the core nanostructure and outer shell comprised of polymer spacer and BSA-biotin-dye, (**E**) Schematic illustration to

demonstrate the specific and spontaneous passive binding of negatively charged PFs to hippocampal neuron cells, (**F**) Hippocampal neurons labelled with PFs are fixed, immunostained and subjected to standard expansion microscopy protocol steps: (**1**) anchoring acryloyl-x to serve as link between biomolecules and gel, (**2**) gelation step resulting in the formation of hydrogel, (**3**) digestion step resulting in the breakdown of non-anchored cellular structure while retaining the anchored biomolecules including PFs, (**4**) expansion of gel when exposed to water resulting in ~4X expansion. (**G**) Schematic showing improved spatial resolution of clustered PFs upon sample expansion. (**H**) Zoomed-in region depicting closely located PFs in the gel matrix that remains unresolved (left) until subjected to water resulting in the creation of physical space between PFs allowing enhanced resolution.

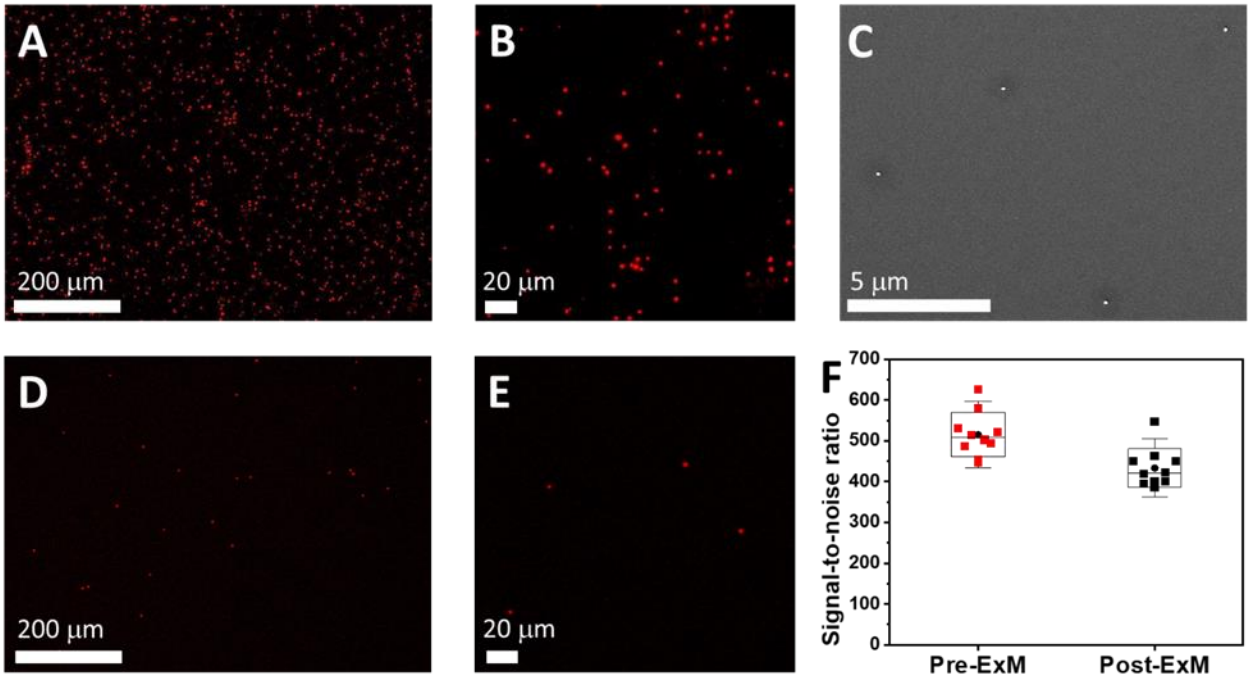

Figure 2.2 Stability of plasmonic-fluors in expansion microscopy (A) Confocal 10X fluorescence image of PF-650 immobilized on BSA-biotinylated glass coverslip in pre-ExM condition. (B) Zoomed-in confocal fluorescence image showing the sparsely adsorbed PF-650, with occasional occurrences of PFs in close proximity. (C) Scanning electron microscopy imaging of PF-650 from (A) showing well-dispersed PF-650, highlighting better resolving power of electron microscopy over light microscopy. (D) Confocal 10X fluorescence image of PF-650 immobilized on BSA-biotinylated glass coverslip in post-ExM condition. (E) Zoomed-in confocal fluorescence image highlighting the large physical separation created between individual PF-650 allowing them to be resolved and counted as digital nanolabels. (F) Signal-to-noise ratio (SNR) corresponding to PF-650 in pre-ExM and post-ExM conditions, exhibiting ~84% fluorescence retention in post-ExM condition.

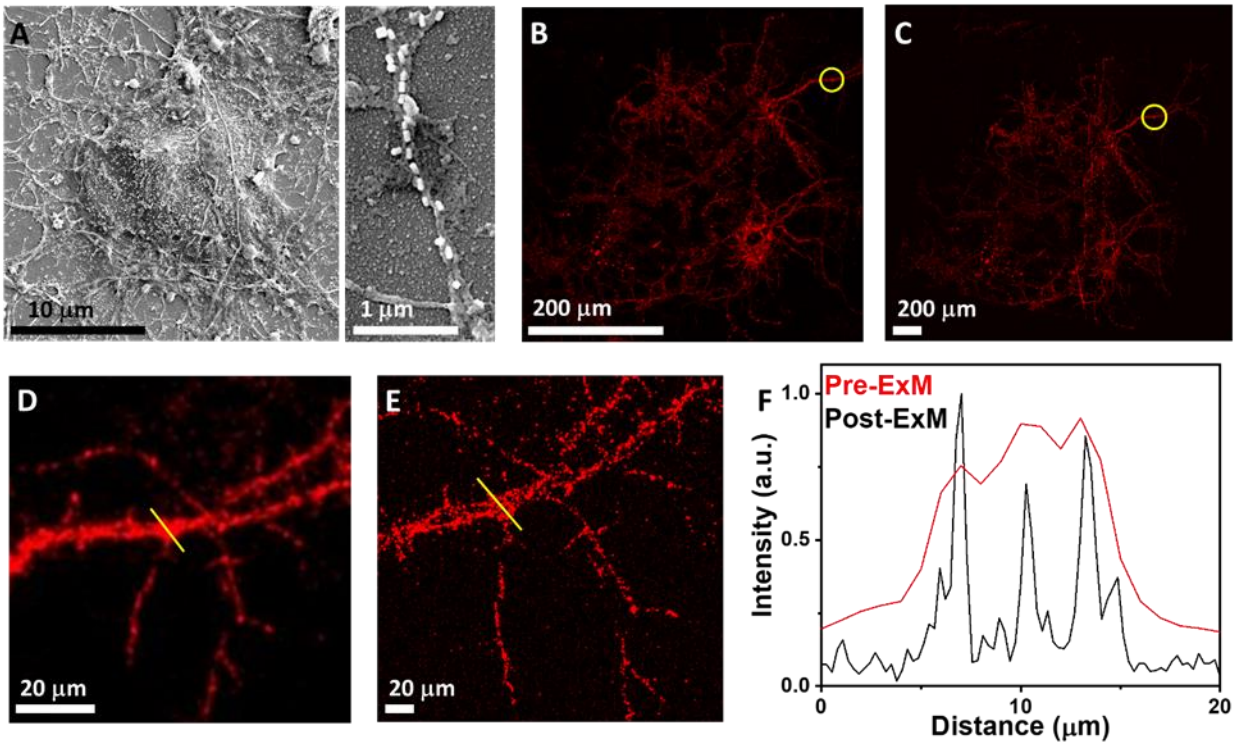

Figure 2.3 Improved spatial resolution of p-ExM. (**A**) SEM image depicting PFs decorating hippocampal neurons in a random orientation on the soma (left panel) and longitudinal alignment along the neurites (right panel). Confocal fluorescence image of cultured hippocampal neurons after 1-hour incubation with negatively charged PF-650 (red) (**B**) pre-ExM and (**C**) post-ExM. Zoomed-in images of (**D**) pre-ExM, (**E**) post-ExM corresponding to the highlighted regions in panels B and C, respectively. (**F**) Fluorescence intensity profile along the marked PF-labeled neurite region in pre-ExM and post-ExM imaging.

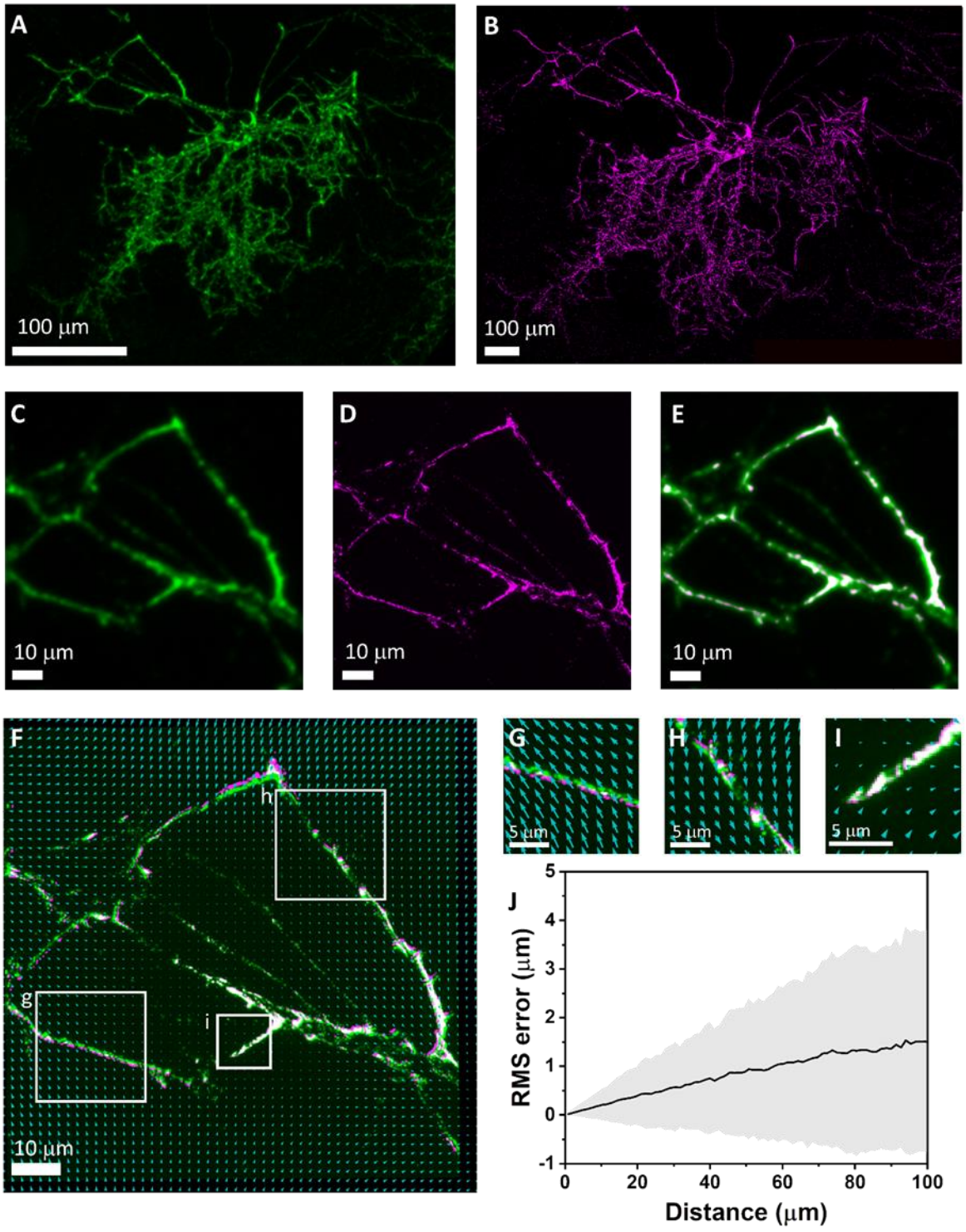

Figure 2.4 Fidelity of p-ExM. Confocal microscopy image of PF-labelled hippocampal neuron in (**A**) pre-ExM and (**B**) post-ExM conditions. Zoomed-in image of (**C**) pre-ExM condition interpolated to achieve the same scale as (**D**) post-ExM. (**E**) Image showing similarity

transformed and b-spline non-rigid registered post-ExM overlay on pre-ExM. (**F**) Overlay of post-ExM before and after b-spline non-rigid registration with the vector distortion analysis showing vector array indicative of transformation required for optimum fitting. (**G, H, I**) Zoomed-in images of arbitrarily identified boxed regions in F to study distortions. (**J**) RMS error measurement as a function of length measurement for post-ExM vs. pre-ExM in PF-labelled hippocampal neuron cells.

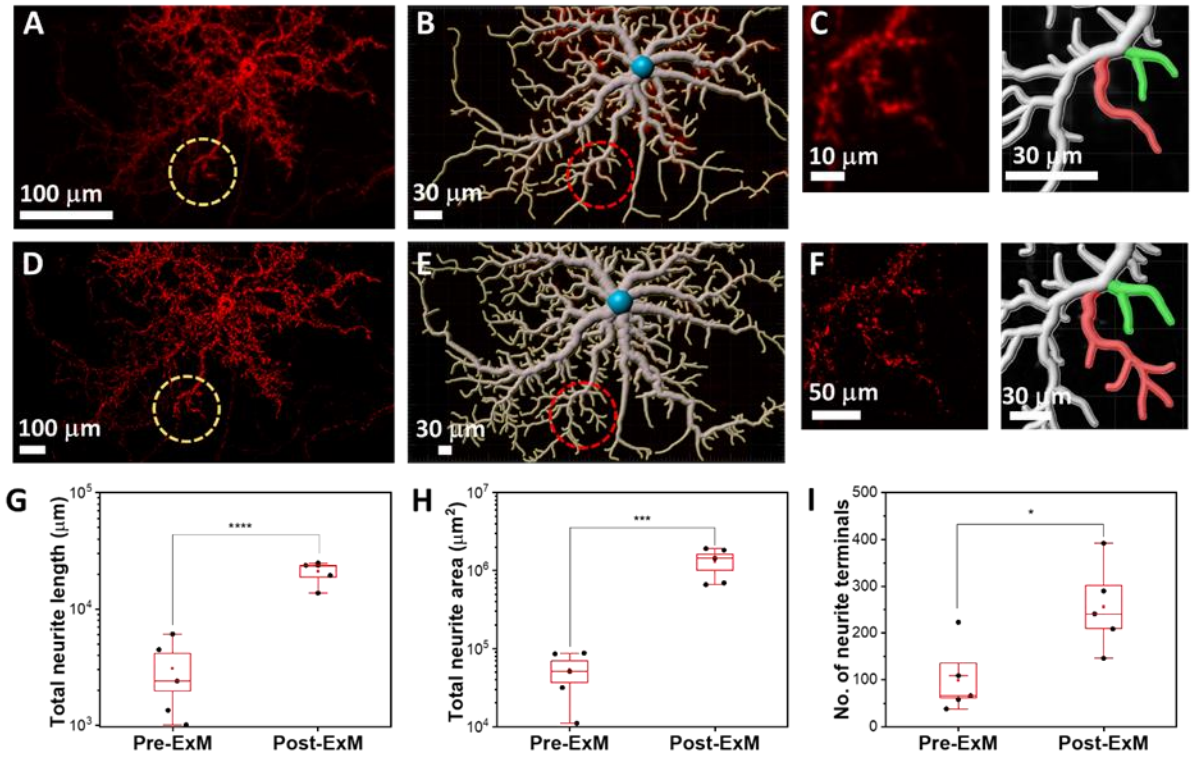

Figure 2.5 Quantification of neuronal morphological features using p-ExM. Confocal fluorescence image of PF-labelled hippocampal neurons at DIV 23 in (**A**) pre-ExM and (**D**) post-ExM conditions. Corresponding filament traced images generated via filament tracer module in IMARIS software (Oxford Instruments) for PFs channel in (**B**) pre-ExM and (**E**) post-ExM conditions. (**C**) Zoomed-in image of highlighted region in pre-ExM condition (left panel: from A and right panel: from B). (**F**) Zoomed-in image of highlighted region in post-ExM condition (left panel: from D and right panel: from E). Green highlighted filament marks the similarly identified region whereas red highlighted filament has 80% higher number of neurite terminals being identified in (**F**) post-ExM when compared to (**C**) pre-ExM condition. Whisker plot representing the morphological maturation parameters (**G**) total neurite length, (**H**) total neurite area, and (**I**) number of neurite terminal points in DIV 23 neurons in pre-ExM and post-ExM conditions,

obtained from filament tracking analysis. Unpaired two-sample t-test, n = 5 PF-labelled neuronal cells from DIV 23, * $p<0.05$, ** $p<0.01$, *** $p<0.001$, and **** $p<0.0001$.

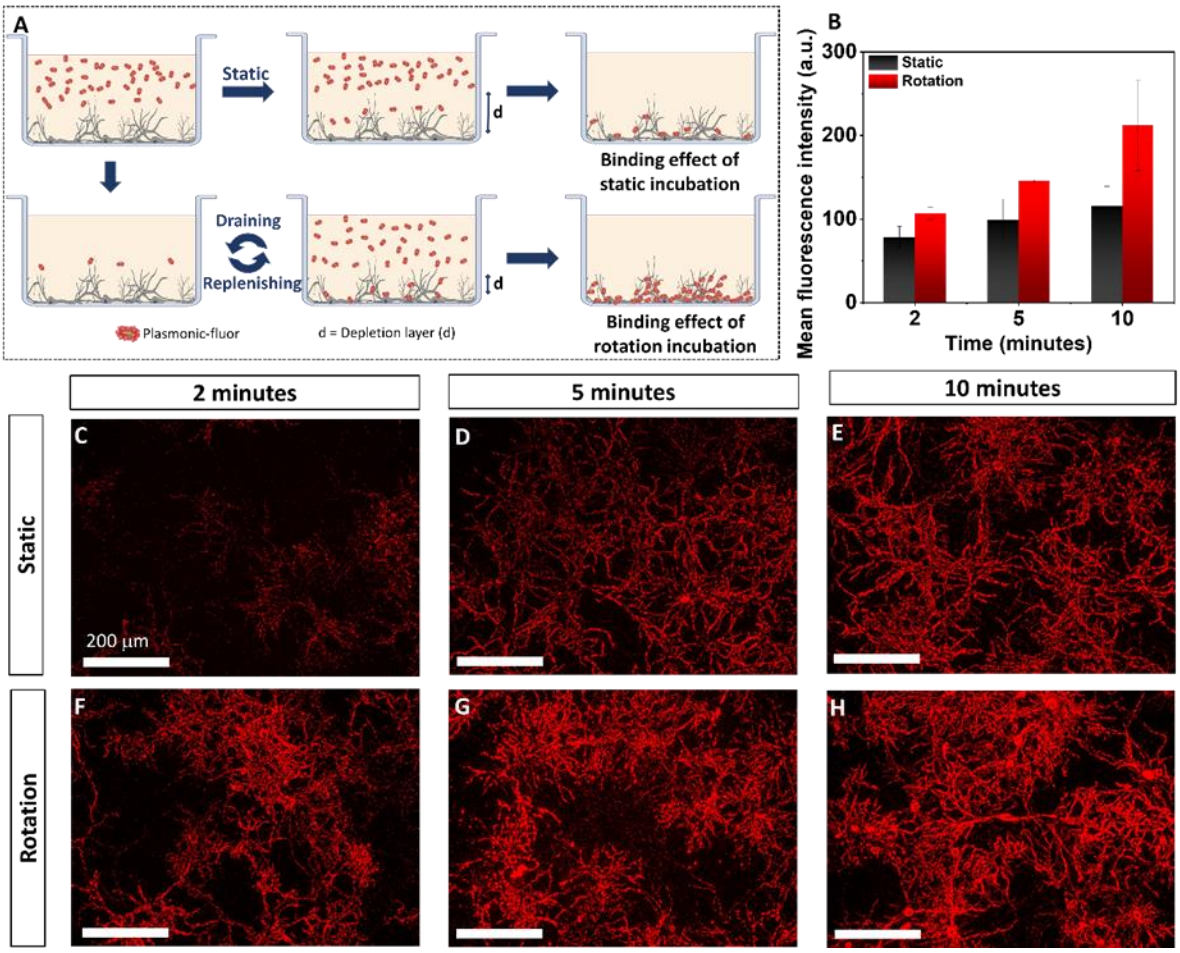

Figure 2.6 Improving PF-binding kinetics in neuron cells. (**A**) Schematic depicting the effect of static vs rotational incubation on labeling efficiency of PFs in neuron cells. Repeat cycles of draining and replenishing bulky nanolabels facilitates a reduction in the depletion layer and overcoming diffusion limitations. (**B**) Ensemble mean fluorescence intensity corresponding to static and rotational incubation in DIV 25 neuron cells (cell density ~20,000) (n=2). Confocal microscopy images (PF-channel) of PF-labelled neuron cells on DIV 25 under static incubation for (**C**) 2 minutes, (**D**) 5 minutes, and (**E**) 10 minutes. Confocal microscopy images (PF-channel) of PF-labelled neuron cells on DIV 25 under rotational incubation for (**F**) 2 minutes, (**G**) 5 minutes, and (**H**) 10 minutes.

Chapter 3: High-resolution imaging of protein secretion at single-cell level using plasmon-enhanced FluoroDOT assay

3.1 Introduction

Proteins secreted by cells into the extracellular space constitute 13-15% of the entire proteome and include growth factors, cytokines, chemokines, antibodies, extracellular matrix proteins, enzymes, hormones, and antimicrobial peptides.[17,56] Secretory proteins facilitate essential physiological and pathological processes such as cell-to-cell communication, cell signaling, activation, inflammation, coagulation, hemostasis, differentiation, migration, toxicity, and defense.[17] Understanding the cell secretome is essential in numerous life sciences disciplines, including immunology, oncology, neurobiology, microbiology, endocrinology, and stem cell biology. Researchers heavily rely on samples collected from cell culture supernatants and conventional immunoassays such as enzyme-linked immunosorbent assay (ELISA) to assess the changes in proteins secreted by cells after various physicochemical or biological stimuli. However, for attaining a detectable signal in ELISA, one needs to collect supernatant from thousands of cells, which have been incubated for an extended duration, typically ranging from 12 hours to several days. Implicit averaging in these methods results in loss of information related to cell-to-cell heterogeneity, cell-cell interaction, and the spatial distribution of secreted proteins. This particularly confounds analysis when working with cells having sub-populations and multi-modal populations. Furthermore, due to the low sensitivity of these techniques, there is little information on the kinetics of protein secretion, particularly at early time-points after

stimulation and under low levels of stimulation. A recent technology feature highlights the imperative for detecting and measuring proteins secreted at single-cell resolution without having to rely on mRNA analysis and mass spectrometry.[57] In more than 60% of the cases, mRNA levels do not correlate with protein abundance.[58,59] On the other hand, mass spectrometry requires specialized strategies to isolate and handle single cells and expensive instrumentation and training, making it unsuitable for routine single-cell secretome analysis.[60] Although ELISpot and FluoroSpot have emerged as powerful tools for studying protein secretions at the single-cell level, they result in low resolution images. The assay read-out is a colored or fluorescent "spot" on a white or dark background, either counted manually or with an ELISpot reader (Figure 1A). Each spot, which is often diffused, indicates a protein-secreting cell, and the size of the spot provides a qualitative and often vague estimate of the amount of protein secreted by the cell. In fact, several shortcomings, including large sample-to-sample and lab-to-lab variability in data acquisition and interpretation, and poor accuracy in quantification of the secretion parameters obligated extensive efforts to establish standardized and automated data acquisition and analysis procedures for evaluation of ELISpot assays.[61] Further, the inherently low signal warrants the use of specialized membrane-coated plates to retain more protein and long incubation time for a discernable signal. The requirement for a dedicated reader further impedes its widespread applicability in laboratory settings.

Here, we introduce an ultrasensitive method for detecting and quantifying protein secretion at a single-cell level. The high sensitivity of the assay stems from an ultrabright plasmon-enhanced fluorescent nanolabel called plasmonic-fluor and is reported to sensitively detect biomarkers for biomedical research and clinical diagnostics.[62-65] We and others have demonstrated that enhancement of the emission of fluorophores in proximity to plasmonic nanostructures such as

gold and silver nanoparticles is largely attributed to (i) the enhanced electromagnetic field at the surface of the plasmonic nanoparticles; and (ii) the decrease in the fluorescence lifetime due to the coupling between the excited fluorophores and the surface plasmons of the nanoparticles.[10,66-71] The reported plasmon-enhanced method, which we call "FluoroDOT assay" is better than conventional approaches as (i) it provides a high-resolution digital signal in the form of dots (particles) per cluster (spot) as opposed to analog signal in ELISpot and FluoroSPOT assays; (ii) it provides spatial information (directional/polarized secretion) which is lost in the 3D membrane of ELISpot and FluoroSPOT assay; iii) due to its high sensitivity, it can detect incipient protein secretions within 30 minutes to few hours, as compared to overnight or days of incubation for conventional assays; (iii) the assay can be read using a standard epifluorescence microscope with a 20x objective as opposed to requirement of a dedicated reader; (iv) the assay is performed on a glass-bottom plate and the cells can be fixed, stained and imaged. Retaining the cells and correlating their secretion provides significant advantage as it provides opportunity to reveal cellular and sub-cellular information (morphology of the cells, activation of fluorescent reporters, and/or correlation of functional significance of heterogeneity with protein secretion) which is difficult with conventional assays (Figure 1B, Table S1). For example, during innate immune responses, macrophages respond to a microbial challenge by inducing a variety of cytokines, including TNF-α, IL-1β, and IFN-α/β, amongst others. However, it has been challenging to assess whether secretion is driven by the majority of directly infected cells, a select subset of infected cells, or uninfected cells in the population. Most previous attempts to unravel single-cell protein secretion utilized microfluidics-based assays (micro-/nano-wells, micro-troughs, droplet platforms) or hyperspectral imaging. [72-77] A major advantage of droplet-based microfluidic channels or small volume microchamber system is its ability to assess real-

time single cell secretion.[78,79] Microfluidics based single cell secretion can achieve high-throughput measurements, however, they are prone to clogging by micron size fragments and dust affecting the reliability of the results. [80] Capillary-assisted microfluidics compartments can provide spatio-temporal dynamics of the single cell secretion but fail to describe the secretion pattern around the cell. [81] Some of these systems also incur high background due to absence of washing steps. [82] These methods have not been widely adopted as mainstream tools due to the compartmentalization of cells and sophisticated set-up, which hinders or eliminates the interaction between cells for orchestrated protein secretion.

Using an ultrabright and specific fluorescent nanolabel developed in our lab, we can image low to high abundant proteins secreted by single cells.[62] We extensively validated the assay by probing proteins secreted from macrophages, dendritic cells (DCs), and DC-T cell co-culture in response to diverse stimuli, including TLR4 stimulation, inflammasome activation, and Mycobacterium tuberculosis infection. Here we report high-resolution images of single-cell protein secretion, providing insight into cell-to-cell heterogeneity, directionality, and correlation with infectivity.

3.2 Results and discussion

First, we set out to compare FluoroDOT assay with standard ELISpot and FluoroSPOT assays. We used healthy adult human PBMCs (peripheral blood mononuclear cells) and treated them with stimulants (phorbol 12-myristate 13-acetate (PMA) and ionomycin) to trigger secretion of IFN-γ. To compare the three assays, we used biotinylated detection antibody followed by streptavidin-fluor (FluoroSPOT), streptavidin-HRP (ELISpot) and streptavidin-plasmonic-fluor (FluoroDOT). We observed clear differences between unstimulated and stimulated wells in all three assays **(Figure 1C, D, E)**. Higher magnification images of cells in FluoroDOT assay

revealed a digitized "dot pattern," corresponding to the proteins secreted by single cells. This was not apparent with the ELISpot or FluoroSPOT assay. The difference between the assays was not due to the distinct substrates the cells were grown on, as the amount of cytokine secreted on the glass substrate, used for FluoroDOT assay, and PVDF membrane, used in the ELISpot/FluoroSPOT assay, was same. The information deduced from FluoroDOT assay is digitized **(Figure S1 A, B, C)**, which allowed us to quantify the signal for the FluoroDOT assay using number of particles (dots) per cluster (spot) using a custom developed image processing algorithm.

Next, we determined if the FluoroDOT assay is uniquely attuned for plasmonic-fluors or if it can also be achieved using conventional fluorophores or previously known bright nanolabels such as quantum dots. For this purpose, we used a dendritic cell line (JAWS II), which secrete the pro-inflammatory cytokine TNF-α after stimulation with the toll-like receptor 4 (TLR4) agonist, lipopolysaccharide (LPS).[83] We seeded the cells on a TNF-α capture antibody-coated glass-bottom 96-well plate followed by LPS treatment at three different concentrations (20 ng/ml, 200 ng/ml, and 2000 ng/ml). After 90 minutes of incubation, the cells were fixed and incubated with biotinylated TNF-α detection antibody. Different wells were then treated with streptavidin-Cy5, streptavidin-quantum dot 655 (Strep-Qdot™ 655), or streptavidin-Cy5-plasmonic-fluor, and the nuclei were stained with DAPI. Using an epifluorescence microscope, we could not discern a signal from the conventional fluorophores, and a very faint signal was observed with Strep-Qdot™ 655 **(Figure S1D, E)**. In contrast, a robust signal was detected with the plasmonic-fluor, and, as expected, there was an increase in TNF-α secretion with increasing LPS concentration **(Figure S1F)**. We further performed imaging using a 60x objective. We observed that the "secretion dot pattern" obtained using the plasmonic fluor correlated well with the morphology

of the cell observed in bright field images. In contrast, no distinct secretion pattern was observed with the conventional fluor and the signal-to-noise ratio for both the conventional fluor and quantum dot was significantly lower compared to plasmonic-fluors. **(Figure 1F)**. The SNR ratio of the plasmonic-fluor was 680 ± 272, nearly 30-fold higher than the conventional fluor (23 ± 4) and 8-fold higher compared to quantum dots (78 ± 50) **(Figure 1G)**. For the conventional fluor, the small molecule diffused inside of the cells leading to a small but finite level of non-specific signal seen in the absence of biotinylated antibody. We also assessed the performance of Strep-Qdot™ 655 using a Qdot specific filter cube (Chroma qDOT655 filter cube). Again, we observed that the SNR of the Strep-Qdot™ 655 images were significantly lower than the Cy5-plasmonic-fluor (**Figure S2**). Due to compatibility issues of the Qdot specific filter, we used a different excitation source for collecting images shown in **Figure S2** compared to those shown **Figure 1F** and **S2**. Thus, the absolute SNR in **Figure 1F** and **Figure S2** are different, but in both cases, we observed a 8-15 fold higher SNR with the Cy5-plasmonic-fluor as compared to the Strep-Qdot™ 655. In addition, as opposed to Qdots, individual Cy5-plasmonic fluors could be resolved using a 20x objective, 0.75 NA. Finally, we observed that quantum dots suffered from substantial blinking (fluorescence intermittency), as previously reported. [84,85] To validate that the fluorescent dots observed are indeed single plasmonic-fluors, we correlated the fluorescence image and scanning electron microscopy (SEM) image obtained from the same location and found a one-to-one correspondence **(Figure 2A)**. Transmission electron microscopy (TEM) images further revealed the size and shape of individual plasmonic-fluors **(Figure 2B)**.

We further compared the fluorescence intensity of a defined molar concentration of plasmonic-fluors with that of conventional fluorophore. The fluorescence intensity increased linearly with increasing concentrations of both conventional fluorophore and plasmonic-fluors (both Cy5 and

Cy3) with at least three orders of magnitude difference in molar concentrations for similar fluorescence intensity. Notably, the slope of Cy5-plasmonic-fluor and Cy3-plasmonic-fluor were nearly 16,000- and 26,400-fold steeper than that of Cy5 and Cy3, respectively **(Figure 2C, Figure S4A).** In our previous work, we have shown that a single plasmonic-fluor is comprised of ~200 molecular fluorophores.[62] The fold increase in brightness (16,000) is significantly higher than the number of fluorophores on a single plasmonic-fluor. This large enhancement in the brightness of the plasmonic-fluors compared to their conventional counterparts is critical for the high-resolution images in the FluoroDOT assay.

To confirm the analyte dose-dependent increase in the fluorescent dots, we performed a standard fluorescence-based sandwich immunoassay and correlated the particle count with that of concentration of the analyte (TNF-α, IL-6, and IFN-γ). We counted the particles using a custom-build algorithm. We observed excellent particle count-dose dependence with a correlation coefficient of >0.99 for all three analytes (limit of detection (LOD) was: TNF-α - 670 fg/ml; IL-6- 8 fg/ml, IFN-γ- 3.17 pg/ml) **(Figure S4B,C)**. To conclude, using JAWS II DCs, we established the assay's sensitivity by demonstrating its ability to image cytokine secretion.

Interestingly, with certain cell types, we did not observe secreted TNF-a in the region overlaping the cell body. For tightly adherent cells such as macrophages and dendritic cells, no signal was observed beneath the cell body, whereas for loosely adherent or suspension cells (PBMCs), we did detect a signal beneath the cell body. This suggested to us that either the adherent cells do not secrete in the region in where they are adhered to the surface or that the capture antibody is not stable in that area. To distinguish these possibilities, we used JAWS II dendritic cells and stimulated them with LPS (200 ng/ml), followed by washing with PBS after 1 hour. We performed the experiment with and without fixing the cells (after the cells had secreted the

cytokine and before adding the detection antibody). When the cells were not fixed, the cells were washed off during the subsequent processing and were not visible in the bright field image. Irrespective of whether the cells were fixed or not fixed, the TNFα secretion resembled a doughnut, with the empty space corresponding to where the cell body is present in the fixed samples, as shown in as shown in **Figure S3 A-C**. We defined the boundary of the cell based on bright field microscopy images. To determine whether the capture antibody beneath the cell is stable after the adhesion of cells, we used the unfixed samples, and we washed away the cells prior to adding 100 pg/ml of recombinant TNFα to the well. We observed that the capture antibody in the empty space where the cell body had been is still able to bind recombinant TNFα (**Figure S3D**). In contrast, if the cell was fixed onto the plate prior to addition of TNFα, the spiked TNFα was not able to access the capture antibody beneath the cells, further confirming that the adhesion of the cell to the substrate prevents the access of secreted protien to capture antibody beneath the cell body (**Figure S3E**). Since the membrane staining was not used to define the boundaries of the cell, it is possible that the signal shown as secreted protein is on the cellular membrane at the extreme periphery of the cell. A membrane counter stain is required to study it in greater detail.

One of the fundamental questions in many cell biology studies is the degree of heterogeneity in cellular responses. When cells are subject to a stimulant, do all the cells respond similarly, or does a small subpopulation of cells exuberantly respond, or is it a combination of both and to what extent does the heterogeneity depend upon the dose of stimulant? We used the plasmon-enhanced FluoroDOT assay to examine the dose-response to LPS treatment, with detailed assessment of the kinetics and cell-to-cell heterogeneity of the response. Using JAWS II DCs and LPS as a stimulant, the FluoroDOT assay revealed no significant secretion of TNF-α for an

incubation duration of 90 minutes at 2 ng/ml of LPS. We observed substantial secretion at 20 ng/ml of LPS, which continued to increase with increasing LPS concentration **(Figure 3A, S5A)**. Similarly, using LPS concentration of 200 ng/ml, we found that TNF-α secretion was detectable after 40 minutes and increased at longer incubation time (60 and 90 minutes) **(Figure 3C, S5B)**. Based on the images, we observed that both the number of cells secreting TNF-α and the amount of TNF-α secretion per cell increased with increasing dose and duration of LPS treatment **(Figure 3B)**. This information cannot be derived from ELISA, which relies on the analysis of the cell culture medium, as the amount of secretion with low dose and short duration of stimulation was below its detection limit **(Figure S6)**. We developed an algorithm to identify clusters of dots and count both the number of clusters in an image and the number of dots within each cluster. Using this algorithm, we quantified TNF-α secreting cells, as indicated by the number of clusters **(Figure 3D, F),** and amount of TNF-α secretion from each cell based upon the number of dots (i.e. particles) in each cluster **(Figure 3E, G)**. The quantitative data corroborated our observations as the difference between treated and untreated cells was only statistically significant when the LPS dose was higher than 20 ng/ml for 90 min incubation or the duration of treatment was more than 40 minutes with 200 ng/ml LPS. Interestingly, we observed that heterogeneity in cell secretion reflected not only the amount of secretion but also the directionality. The presence of capture antibody in the immediate vicinity of the secreting cell enables continuous capture of the secreted cytokine, thereby limiting diffusion of the analyte and retaining spatial information on the source of secretion. Interestingly, we found that at 20 ng/ml dose of LPS, approximately 55% of the cells exhibited isotropic secretion, whereas ~ 45% of the cells secreted TNFα preferentially on one side after 90 minutes **(Figure S6C and D**). There were no significant differences in the fraction of cells exhibiting isotropic secretion at 200 ng/ml or

2000 ng/ml LPS, suggesting that the phenomena is not related to limiting ligand. The percentage of cells with anisotropic secretion was also relatively stable from 20 to 90 minutes. We also observed "doublet clusters" from cells that were either seeded close to each other or were undergoing cell division **(Figure S7E)**. These intricate details of the secretion pattern revealed by the FluoroDOT assay are not achievable by conventional ELISpot and FluoroSPOT assays.

Next, we set out to investigate if the FluoroDOT assay can reveal proteins secreted through a non-conventional pathway in primary cells. IL-1β is secreted in response to activation of the NOD-like receptor pyrin domain-containing 3 (NLRP3) inflammasome [86]. IL-1β lacks a classical secretion signal and is secreted by a non-conventional transport pathway that involves caspase-dependent cleavage and Gasdermin-D [87]. IL-1β secretion depends upon a priming signal and inflammasome activation [88]. We treated alveolar macrophages with LPS, followed by nigericin, which leads to cleavage of pro-IL-1β and secretion of IL-1β in the extracellular space **(Figure 4A)**.[89] Using the FluoroDOT assay, we detected IL-1β secretion 30 minutes after NLRP3 activation by nigericin. In contrast, TNF-α secretion was detected in response to 4 hours of LPS treatment **(Figure 4B, S7 A, B)**. While most cells secreted TNF-α in response to LPS, less than half of the cells responded with IL-1β secretion. As we had seen in the JAWS II cells, the alveolar macrophages secreted TNF-α in both isotropic and anisotropic manner. In contrast, the majority of cells (82%) showed isotropic secretion of IL-1β. We confirmed the correlation between particle count and concentration of IL-1β by plotting a standard curve and found the LOD to be 3 fg/ml **(Figure S7 C, D)**. Using the algorithm, we determined the number of IL-1β secreting cells along with the amount of IL-1β secreted by each cell as indicated by the number of clusters and number of particles/clusters, respectively **(Figure 4C, D)**. The larger amount of TNF-α as compared IL-1β secreted was confirmed by measuring the cytokine concentration in

cell culture supernatant collected from 150,000 cells using ELISA **(Figure S7 E)**. These results suggest that the plasmon-enhanced FluoroDOT assay enables the quantification of the distinct and specific secretion of corresponding cytokines without cross-interference after treatment with two different stimulants.

As a proof-of-concept, we investigated the feasibility of spectrally multiplexed analysis of two proteins at a single-cell level. For this purpose, we conjugated the detection antibody for TNF-α and IL-6 to Cy5-plasmonic-fluors and Cy3-plasmonic-fluors, respectively. We first confirmed the specificity of individual plasmonic-flours to their respective analyte by spotting the capture antibody for analytes (*i.e.* IL-6 and TNF-α) within the same well of a microtiter plate **(Figure S8 A)**. As anticipated, both plasmonic-flours specifically recognized their respective analytes in single capture antibody and double-capture antibody-coated regions of the plate **(Figure S8 B)**. Further, we performed multiplexed plasmon-enhanced fluorescent immunosorbent assay and observed a standard curve with a good correlation (R^2 =0.9942, LOD= 15.1 pg/ml for TNF-α and R^2= 0.9958, LOD= 2.5 pg/ml for IL-6, respectively) between the particle count and concentration of the protein analyte **(Figure S8 C, D)**. The multiplexed assay requires coating of both capture antibodies in a defined area, while the same area is available for coating a single capture antibody for a singleplexed assay. Due to differences in the amount of available capture antibody, the sensitivity of multiplexed assay is reduced compared to a singleplex. Using LPS-stimulated JAWS II DCs, we assessed the concurrent secretion of TNF-α and IL-6 at a single-cell level. We observed an increase in the overall secretion of both cytokines with the increasing duration of LPS incubation from 30 minutes to 3 hours **(Figure 5A)**. We noted significant heterogeneity in the secretion of both cytokines in terms of the amount of secretion (given by the number of particles) and temporal dynamics **(Figure 5B)**. Interestingly, we observed significant

cell-to-cell variation, even after 30 minutes of LPS treatment, such that some cells started secreting TNF-α, while no secretion for IL-6 was observed for the same cells **(Figure 5C)**. At longer durations (2 and 3 hours), we observed more predominant IL-6 secretion compared to TNF-α. Our observations align with previous findings in which mRNA quantification and ELISA-based assay showed TNF-α and IL-6 were produced with distinct kinetics in LPS-treated, activated DCs [90]. Thus, using the multiplexed FluoroDOT assay, we were able to ascertain population dynamics of two proteins secreted from single cells simultaneously. While as a proof-of-concept we have demonstrated cytokine secretion for two proteins, it is worth noting that the plasmonic-fluor can be generated with any molecular fluorophore, thus enabling higher multiplexing capability (up to 6 colors with minimal spectral overlap) [62,91]. The LSPR (localized surface plasmon resonance) wavelength of the plasmonic nanostructures is highly sensitive to its composition, size, and shape **(Figure S4B)**, and can therefore be tuned over a wide range covering visible to near-infrared wavelength.

While the previous assays revealed heterogeneity when cells were exposed to a homogeneous stimulus, during actual infections, only a subpopulation of cells will be infected, and the resultant heterogeneity in secretion is likely to be more complex. One of the major advantages of the plasmon-enhanced FluoroDOT assay is its ability to retain the cells on the plate by fixing them and later imaging. Taking advantage of this feature, we next set out to study the impact of infection by *Mycobacterium tuberculosis* (*Mtb*) on TNF-α secretion by bone marrow-derived macrophages (BMDMs) **(Figure 6A)**. We infected BMDMs with dsRed-expressing *Mtb* and observed increased secretion of TNF-α by *Mtb*-infected cells compared to uninfected cells **(Figure 6B)**. We could readily detect TNF-α secretion by the FluoroDOT assay at 6 hours after infection, when TNF-α was undetectable by conventional ELISA, underscoring the sensitivity of

the assay. Remarkably, the TNF-α secretion pattern faithfully followed the elongated morphology of the BMDMs, and there was significant heterogeneity in terms of the direction in which secretion occurred. We observed that some of the infected cells secreted TNF-α, while there were other infected cells that did not secrete the cytokine (**Figure 6C)**. Thus, we verified the utility of the FluoroDOT assay for studying single-cell protein secretion within the context of infection and unraveling the underlying heterogeneity. Detailed investigation of protein secretions in single cells will help build enhanced models for understanding host-pathogen interaction in immune cells, emphasizing the value of extending the analysis beyond bulk measurements [92,93].

Lastly, we examined the FluoroDOT assay's applicability in a multi-cellular system by co-culturing bone marrow-derived dendritic cells (BMDCs) infected with *Mtb* along with antigen-specific $CD4^+$ T cells that expressed GFP under control of the Nur77 promoter [94]. We used $CD4^+$ Th1 effector cells from transgenic mice (called P25 cells) that express a T cell receptor (TCR) specific for peptide 25 (amino acids 240-254) of *Mtb* Ag85B [95]. In response to co-culture with *Mtb*-infected BMDCs, the P25 cells secrete IFN-γ and induce GFP expression **(Figure 7A)**. As a negative control, we infected MHC-mismatched (MM) BMDCs ($H\text{-}2^k$ rather than $H\text{-}2^b$). Before performing the experiment with *Mtb*, we first set out to estimate the minimum duration of co-culture required for detectable IFN-γ secretion using P25 peptide. We found that after 2-3 hours of BMDC-T cell co-culture, clusters of IFN-γ secretions were evident **(Figure S9)**. Next, we performed the FluoroDOT assay on *Mtb*-infected BMDCs co-cultured with T cells for 3 hours, and we observed distinct clusters of IFN-γ secretion in wells with WT BMDCs while almost no secretion was seen with the MM control BMDCs **(Figure 7B, C, Figure S10 A, B)**.

Additionally, we did not observe IFN-γ secretion with BMDCs only, T cells only, or BMDCs and T cells without infection or peptide.

We observed clusters of BMDCs and GFP expressing $CD4^+$ T cells with IFN-γ secretion surrounding them after 3 hours of incubation, further confirming the specificity of the assay **(Figure 7D)**. We detected IFN-γ secretion in the FluoroDOT assay after 3 hours of co-culture, when it was undetectable in cell culture supernatants by ELISA. Finally, we compared the number of particles in each cluster for WT and MM and found that the number of particles/clusters in WT BMDCs was significantly higher than that of MM BMDCs **(Figure 7E)**. We demonstrated the ability to correlate functional heterogeneity of cells in an antigen presentation assay for studying IFN-γ release. Using GFP-expressing cells, we further validated our findings that IFN-γ secretion was indeed a result of $CD4^+$ T cell activation and studying co-regulation of genes is achievable using this assay.

3.3 Conclusion

ELISpot is a widely employed bioanalytical method, used in both research and clinical settings for a wide range of applications such as screening antigen-specific immune cells and functional T cells in cancer patients. It is used to assess response to immunotherapy, diagnose tuberculosis (T-SPOT.TB assay), map T cell responses against HIV, detect antibody secreting cells in blood after vaccination, and for functional analysis of circulating tumor cells (CTCs) to understand drug susceptibility [75,76,96-100]. Despite its enormous utility, this method has not undergone significant technological advances in spatial resolution or sensitivity over the past three decades. ELISpot assays thus remain severely limited by the inability to spatially resolve protein secretion, discrepancies in assay read-out, and false negatives in clinical diagnosis [61,101]. We introduce a simple, yet powerful, ultra-resolved digital version of ELISpot and FluoroSpot assay

called FluoroDOT assay. The unmet need for an exceptionally bright fluorescent tag capable of detecting single-molecule fluorescence is served by plasmonic-fluors, which outperform conventional fluorophores and quantum dots. Using plasmonic-fluors, we improved the limit-of-detection of the FluoroDOT assay by more than two orders of magnitude compared to conventional biolabels [62]. We are able to digitalize the signal and count the fluorescent dots in contrast to integrating the signal as in case of ELISpot and FluoroSpot, which can be considered as analog version of this assay. This method will provide deeper insights into how the mechanotransduction, polarization, and adhesion properties of cells correlates with single-cell protein secretion, and application of this method for studying inflammasome-mediated protein secretion in diverse cell types including immune cells and endothelial cells [102,103]. Since heterogeneity is a fundamental characteristic of cellular systems, single-cell technologies and measurements are of immense value for an in-depth understanding of individual cells, facilitating disease model development, drug discovery, and meaningful biological insights beyond ensemble population averages [104,105]. We noted cell-to-cell heterogeneity in response to LPS treatment **(Figure 3 and S5)**, inflammasome activation **(Figure 4)**, and cytokine response to Mtb infection **(Figure 6)**. We found a difference in the secretion pattern of TNF-α and IL-1β. While many cells secreted TNF-α in an anisotropic manner, this was not the case with IL-1β secretion. These proteins are secreted in very different manners: TNF-α secretion depends upon cleavage of the membrane-bound precursor by the metalloprotease, TNF alpha converting enzyme (TACE), whereas IL-1β secretion depends upon Gasdermin-D pores. The anisotropic nature of TNF-α secretion suggests that some required component is polarized in the cell, perhaps reflecting underlying polarity associated with dendritic cell migration.[106] While the underlying reason behind the anisotropic secretion is a subject of future study, the ability of the FluoroDOT

assay to faithfully capture these events further highlights its utility in biomedical research. The FluoroDOT assay enables the visualization of heterogeneity, infectivity, and directionality, and it can be implemented for better understanding of host-pathogen interaction, neuronal secretions, and tumor cytotoxicity. As proof of principle, we demonstrate that it can be applied to study cytokine secretion during *Mtb* infection. There is an increasing appreciation that TB infection is characterized by bacterial and host heterogeneity [92,107-109]. However, the ability to assess protein secretion at a single-cell level has lagged behind single-cell technologies to assess mRNA or intracellular protein abundance of both the bacilli and host. The high resolution achieved here can be applied to determine the relationship between bacterial and host heterogeneity, mapping the spatial distribution of protein secretion in a multiplexed and multi-cellular situation to decode critical information on cellular behavior.

Overall, we developed an ultrasensitive digitized FluoroDOT immunoassay for detection of protein secretions from cells. The assay can employed for multiplexed detection of proteins. It can provide detailed spatial mapping of the secretion around the cells along with the sub-cellular information. When compared to any of the conventionally used approaches, we believe FluoroDOT assay will lead to transformative advances in single-cell secretion studies as it is versatile, low-cost, and is readily adaptable in any laboratory setting with regularly used supplies and reagents (glass-bottom 96-well plate, ELISA reagents), commercially available plasmonic-fluor (Auragent Bioscience LLC), and a standard epifluorescence microscope. Considering the evolving landscape of cellular traits, this method holds the potential to provide a comprehensive understanding of single-cell secretome.

3.4 Experimental section

- **Cell lines:**

Mouse JAWS II dendritic cells (immature, monocytes ATCC® CRL-11904™) were cultured in alpha minimum essential medium with ribonucleosides, deoxyribonucleosides, 4 mM L-glutamine, 1 mM sodium pyruvate and 5 ng/ml murine GM-CSF, 10% heat-inactivated fetal bovine serum, 50 IU/ml of penicillin, 50 μg/ml of streptomycin.

- **Primary cells**:

i) *Blood sampling and isolation of peripheral blood mononuclear cells (PBMCs) processing:* Heathy individuals consented for blood samples. All samples were collected in accordance with the procedures approved by the Institutional Review Board at Washington University in St. Louis. Donor's demographic data was deidentified. Samples were obtained in sodium heparin tubes. Fresh whole blood samples were processed within 90 min of collection as previously described.[110] Briefly, blood was diluted in an equal volume of PBS and layered carefully on Ficoll Paque PLUS (GE Healthcare). The PBMC fraction was isolated following centrifugation at 500 × *g* for 30 minutes at room temperature. The number of total PBMCs was determined with a Vi-CELL Viability Analyzer (Beckman Coulter, Brea, CA).

ii) *Isolation of alveolar macrophages (AM):* To obtain AMs, bronchoalveolar lavage (BAL) was performed in anesthetized mice lungs using 26G catheters via intra-tracheal route. DPBS containing 0.6 mM EDTA and 1% FBS was used as BAL buffer. Three washes were performed with 1 ml of BAL buffer. DMEM (Dulbecco's Modified Eagle Medium) with 10% FBS,

Glutamax (1:100) and freshly prepared HEPES (4-1-piperazineethanesulfonic acid) buffer (1:100) was used to culture the cells.

iii) *Isolation and culture of BMDMs and BMDCs:* For BMDCs, the bone marrow cells were collected and cultured for seven days in 100 mm Petri dishes containing 10 ml of RPMI medium supplemented with 10% heat-inactivated fetal bovine serum, 50 IU/ml of penicillin, 50 μg/ml of streptomycin and 20 ng/ml of mouse recombinant granulocyte-macrophage colony-stimulating factor (R&D Systems). For differentiation into BMDMs, DMEM medium was supplemented with 10% FBS and 20% L929-conditioned medium for 7 days. The concentration of L929-conditioned medium was reduced to 10% before infections. The GMCSF was removed before infections. Murine hematopoietic stem cells were isolated from the tibia and femurs of 6- to 12-week-old C57BL/6 or MHC-II mismatch mice, obtained from the Jackson laboratory and processed as described above.

iv) Bacterial Strains and Growth Conditions: Mtb strain H37Rv expressing DsRed (selected with 25ug/ml kanamycin) was grown at 37°C in 7H9 medium (Middlebrook 7H9 broth; Difco) supplemented with 0.05% Tyloxapol (Sigma), BBL Middlebrook OADC (oleic acid-albumin-dextrose-catalase) enrichment, and 0.2% glycerol (Sigma). For making single cells, *Mtb* were passed through a 5 μm filter before infection.

- **Mice:**

Female C57BL/6 (H-2b) mice that were 6- to 12-weeks of age were purchased from Jackson Labs. The mice were maintained under pathogen-free conditions. All experiments employing mice were performed in accordance with laboratory animal protocol approved by the School of Medicine Animal Studies Committee of Washington University in St. Louis. Mice were

euthanized using CO_2 asphyxiation and cervical dislocation. The euthanized mice were kept in 70% (v/v) ethanol for 1 min. Both the femurs and tibiae were isolated, and the muscle attachments were carefully removed using gauze pads. Both ends of the bones were cut with scissors and the marrow was centrifuged in an adapted centrifuge tube (0.65 ml tube with a hole inserted in 1.5 ml tube) at 1,000 rpm for 10 seconds. The pellet was resuspended by vigorous pipetting in RPMI 1640 medium. The cells were passed through a 70 μm cell strainer to prepare a single-cell suspension. After one wash (1,100 rpm, 5 min), red blood cells (RBC) were depleted with RBC lysis buffer (Millipore Sigma, St. Louis, MO, USA).

Plasmonic-fluor procurement and characterization*:* Streptavidin-conjugated Cy3-plasmonic-fluor (PF550^{TM} ultrabright fluor) and streptavidin-conjugated Cy5-plasmonic-fluor (PF650^{TM} ultrabright fluor) was purchased from Auragent Biosceince LLC (St. Louis, USA). The extinction was measured using a Shimadzu UV-1800 spectrophotometer. SEM images were obtained using a FEI Nova 2300 field-emission scanning electron microscope at an acceleration voltage of 10 kV. TEM images were obtained using a JEOL JEM-2100F field emission instrument. A drop of aqueous solution was dried on a carbon-coated grid, which had been made hydrophilic by glow discharge. Molar concentrations of plasmonic-fluors was calculated as described previously.[62] Fluorescence intensity was recorded using Azure Biomolecular Imager: Sapphire RGBNIR (Azure Biosystems, Inc. Dublin, USA) and the images were analyzed using Licor Image Studio Lite.

Standard curve using plasmonic-fluors*:* Mouse TNFα DuoSet ELISA kit (R&D systems, catalog number DY410, lot number P189768), mouse IL-6 DuoSet ELISA kit (R&D systems, catalog number DY406, lot number P234212), mouse IFNγ DuoSet ELISA kits (R&D systems, catalog number DY485-05, lot number P234214) and mouse IL-1β (Invitrogen, catalog number

88-7013-88 and lot number 183204000) were used to perform the assays. Glass-bottom 96-well black plate (P96-1.5H-N, Cellvis, Mountain View, USA) was first coated with capture antibodies as per manufacturer's instructions (100 µl/well) and incubated overnight at 4^{o}C. The plate was washed three times with 1x PBST (1x PBS with 0.05% Tween-20) and then blocked with 200 µl of reagent diluent (1x PBS in 1% BSA, 0.2µm filtered). After blocking the plates were washed three times with PBST, and serial dilutions of standard protein was added to different wells in duplicates and incubated for 2 hours at room temperature. The plates were washed three times with PBST and then incubated for 2 hours with 100 µl of biotinylated detection antibody as per the manufacturer's instructions. The plates were washed three times with PBST and streptavidin Cy5-plasmonic-fluor (extinction 0.5) for 30 minutes at room temperature in dark. Finally, the plates were washed three times in PBST and imaged using Nikon TsR2 epifluorescence microscope.

FluoroDOT assay on JAWS II DC*:* Mouse TNFα DuoSet ELISA kits (R&D systems, catalog number DY410, lot number P189768) was used to perform the assays. Glass-bottom 96-well black plate (P96-1.5H-N, Cellvis, Mountain View, USA) was first coated with capture antibodies (0.8 µg/ml in PBS), 100 µl/well and incubated overnight at 4^{o}C. The plate was washed three times with 1x PBS and then blocked with 200 µl of reagent diluent (1x PBS in 1% BSA, 0.2µm filtered). After blocking, the plates were washed three times with PBS. JAWS II DCs were seeded on the capture coated plates, at the seeding density of 5,000 cells/well in 100 µl of medium followed by incubation at 37^{o}C in 5% CO_2 for 30 minutes. All the non-adherent cells were removed by taking out the medium and replacing it with 100 µl of fresh medium containing varying amounts of LPS ranging from (0 to 2000 ng/ml). The cells were incubated at 37^{o}C in 5% CO_2 for varying durations from 20 minutes to 90 minutes. After completion of the incubation

duration, the medium was decanted, and the cells were fixed using 100 µl/well of 4% neutral buffered formalin (NBF) for 20 minutes at room temperature. The plates were then washed three times with PBS and incubated with biotinylated detection antibodies, 75 ng/ml in reagent diluent for 2 hours at room temperature. The plates were washed three times using PBS and then were incubated with 100 µl/well of streptavidin Cy5-plasmonic-fluors (extinction 0.5) for 30 minutes at room temperature in dark. For comparison, 100 µl of 1 µg/ml of streptavidin-Cy5 (Thermo Fisher Scientific, catalog number SA1011) as conventional fluorophore and 1 nM of streptavidin QD 655^{TM} (Thermo Fisher Scientific, catalog number Q10123MP) was added to each well for 30 minutes at room temperature in dark. The plates were washed with PBS three times, and the nuclei of the cells were stained with 300 nM DAPI solution (Millipore Sigma, St. Louis, MO, USA) for 5 minutes at room temperature in dark. Finally, the plates were washed three times in PBS and imaged using Nikon TsR2 epifluorescence microscope. For ELISA, culture supernatants of JAWS II DC after treatment described above were collected and TNFα concentration was measured using mouse TNFα DuoSet ELISA kits (R&D systems, catalog number DY410, lot number P189768) as per manufacturer's instructions.

Epifluorescence microscopy: All images were acquired on a Nikon Eclipse Ts2R-FL epifluorescence illumination microscope with a 20x, 0.75–numerical aperture (NA) lens and 60x, 1.4-NA. The microscope is attached to Hamamatsu digital camera (ORCA-Flash 4.0) with aura light engine. We used NIS-Elements AR 5.11.01 64-bit software to acquire images. Bright field and fluorescence images were collected in four channels corresponding to DAPI, Cy5, TRITC and GFP. For Cy5, TRITC and GFP, 200 ms exposure time was used and for DAPI exposure time of 50 ms was used. All images were saved as .tif files and further processed.

Image Processing and calculation of signal-to-noise ratio: Image J 1.53a (64-bit), was used for adjusting the brightness and contrast of .tif images. Pseudo-color was imparted to images collected from different channels and merged using Image J tool. Pseudo-line was drawn on the image and analyzed using "plot profile" feature to obtain intensity vs. distance (pixels) graph. The raw data of the graph was exported, and signal-to-noise ratio (SNR) was calculated using the following equation:

$$SNR = (Average\ signal)/(Standard\ deviation\ of\ noise)$$

Average of 5 pixels with highest intensity was recorded as average signal. Standard deviation of first and last 50 pixels was recorded as standard deviation of noise. In case of ELISpot because the images had white background, "invert image" feature was used to create a dark background before the intensity vs. distance graph was obtained.

ELISpot/FluoroSPOT and FluoroDOT assay on PBMCs: Capture antibody pre-coated polyvinylidene difluoride–backed strip plates were used for ELISpot and FluoroSPOT assays as per the manufacturer's instructions for detection of human IFNγ (ImmunoSPOT, Cellular Technology (CTL), Cleavland, OH). Samples were run in duplicate for each assay type. For ELISpot and FluoroSpot assays, 25,000 PBMCs/ well in 100 µl of media were seeded on the plate. Human IFNγ ELISpot development module (R&D systems, catalog number SEL285) was used to perform the FluoroDOT assays. Glass-bottom 96-well black plate (P96-1.5H-N, Cellvis, Mountain View, USA) was first coated with capture antibodies (1:60 dilution in PBS), 100 µl/well and incubated overnight at 4^{o}C. The plate was washed three times with 1x PBS and then blocked with 200 µl of reagent diluent (1x PBS in 1% BSA, 0.2µm filtered). After blocking, the plates were washed three times with PBS. For FluoroDOT assay 12,500 PBMCs/well in 100 µl

of medium followed by incubation at 37ºC in 5% CO_2 for 30 minutes. All the non-adherent cells were removed by taking out the medium and replacing it with 100 µl of fresh medium containing PMA (1 ng/ml) and ionmycin (400 ng/ml). The cells were incubated at 37ºC in 5% CO_2 for 18 hours. After completion of the incubation duration, the medium was decanted, and the plates were then washed three times with PBS and incubated with biotinylated detection antibodies, 1:60 dilution in reagent diluent for 2 hours at room temperature. The plates were washed three times using PBS and then were incubated with 100 µl/well of streptavidin Cy5-plasmonic-fluors (extinction 0.5) for 30 minutes at room temperature in dark. Finally, the plates were washed three times in PBS and imaged using Nikon TsR2 epifluorescence microscope. For ELISpot assay, streptavidin-bound alkaline phosphatase and developer solution and for FluoroSPOT assay streptavidin-bound FITC were applied to samples as per manufacturer instructions before imaging and analysis using Cellular Technology series 6 ImmunoSpot Universal Analyzer with ImmunoSpot 7.0 professional software (Cellular Technology Analyzers, Shaker Heights, OH). Analysis parameters were optimized to obtain appropriate spot numbers (cytokine-secreting cells) and were maintained constant throughout each sample.

FluoroDOT assay using alveolar macrophages: Mouse TNFα DuoSet ELISA kits (R&D systems, catalog number DY410, lot number P189768) and mouse IL-1β (Invitrogen, catalog number 88-7013-88 and lot number 183204000) were used to perform the assays. Glass-bottom 96-well black plate (P96-1.5H-N, Cellvis, Mountain View, USA) was first coated with TNFα capture antibody (0.8 µg/ml in PBS) or 1L-1β capture antibody (1:250 dilution in PBS), 100 µl/well, and incubated overnight at 4ºC. The plate was washed three times with 1x PBS and then blocked with 200 µl of reagent diluent (1x PBS in 1% BSA, 0.2µm filtered). After blocking the plates were washed three times with PBS. Mouse alveolar macrophages were seeded on the

capture antibody-coated plates, at the seeding density of 5,000 cells/well in 100 µl of medium followed by incubation at 37^{o}C in 5% CO_2 for 30 minutes. All the non-adherent cells were removed by taking out the medium and replacing it with 100 µl of fresh medium containing 500 ng/ml of LPS. The cells were incubated at 37^{o}C in 5% CO_2. After 4 hours, for some wells, 20 µM nigericin was added and the plate was incubated for another 30 minutes. Subsequently, the medium was decanted, and the cells were fixed using 100 µl/well of 4% neutral buffered formalin (NBF) for 20 minutes at room temperature. The plates were then washed three times with PBS and incubated with biotinylated detection antibodies (TNFα 75 ng/ml and IL-1β 1:250 dilution) in reagent diluent for 2 hours at room temperature. The plates were washed three times using PBS and then were incubated with 100 µl/well of streptavidin Cy5-plasmonic-fluors (extinction 0.5) for 30 minutes at room temperature in dark. The plates were washed with PBS three times and the nuclei of the cells were stained with 300 nM DAPI solution (Millipore Sigma, St. Louis, MO, USA) for 5 minutes at room temperature in dark. Finally, the plates were washed three times in PBS and imaged using Nikon TsR2 epifluorescence microscope.

TNFα and IL-1β ELISA of AM culture supernatant: AMs were seeded in 96-well plate (Corning® Costar®, Millipore Sigma, St. Louis, MO, USA) at a seeding density of 150,000 cell in 150 µl of media. Adherent AMs were selected by incubating for 1 hour in media and further, culture medium was replaced with DMEM containing 500 ng/ml LPS for priming. After 4 hours of LPS treatment, 20 µM nigericin was added to activate NLRP3 inflammasome for 30 minutes. Cell culture supernatant was collected and cytokine concentration was measured using mouse TNFα DuoSet ELISA kits (R&D systems, catalog number DY410, lot number P189768) and mouse IL-1β (Invitrogen, catalog number 88-7013-88 and lot number 183204000) as per manufacturer's instructions.

Antibody conjugation on plasmonic-fluor for multiplexing and validation: Streptavidin-conjugated Cy3-plasmonic-fluor (40 µl, extinction 32) and streptavidin-conjugated Cy5-plasmonic-fluor (40 µl, extinction 30) was added to 50 µl of 4.5 µg/ml biotinylated IL-6 detection antibody and biotinylated TNF-α detection antibody, respectively. The mixture was incubated for 30 minutes at room temperature and then washed twice with pH 10 water. For washing, Cy3-plasmonic-fluor was centrifuged at 4,000 revolutions per minute (rpm) for 10 minutes, and Cy5-plasmonic-fluor was centrifuged at 6,000 rpm for 10 minutes. Finally, the pellet was resuspended in 1% BSA in 1x PBS and stored in 4^{o}C until further use. In order to validate the successful conjugation of the antibody, 0.5 µl of TNFα capture antibody (0.8 µg/ml in 10% glycerol in 1x PBS) was deposited on top-left area of a 96-well glass-bottom plate. Similarly, 0.5 µl of IL-6 capture antibody (2 µg/ml in 10% glycerol in 1x PBS) was deposited on top-right area of the same 96-well glass-bottom plate. 0.5 µl of a mixture of TNFα capture antibody (0.8 µg/ml in 10% glycerol in 1x PBS) and IL-6 capture antibody (2 µg/ml in 10% glycerol in 1x PBS) was deposited on bottom-middle area of the same 96-well glass-bottom plate. The plate was sealed with plate sealant and incubated for 2 hours at room temperature. The plate was washed three times with 1x PBST and then blocked with 200 µl of reagent diluent (1x PBS in 1% BSA, 0.2µm filtered). After blocking, the plates were washed three times with PBST and 5,000 pg/ml of both of standard proteins (TNFα and IL-6) in 100 µl of 1% BSA in 1x PBS was added to the well and incubated for 2 hours at room temperature. The plates were washed three times with PBST and then incubated for 2 hours with a suspension comprised of 50 µl of IL-6 detection antibody-conjugated Cy3-plasmonic-fluor and 50 µl of TNFα detection antibody-conjugated Cy5-plasmonic-fluor (extinction 1 each) in dark. Finally, the plates were washed

three times in PBST and imaged using Nikon TsR2 epifluorescence microscope using a 4x objective.

Multiplexed FluoroDOT assay: Mouse TNFα DuoSet ELISA kits (R&D systems, catalog number DY410, lot number P189768) and mouse IL-6 DuoSet ELISA kit (R&D systems, catalog number DY406, lot number P234212) were used to perform the assays. Glass-bottom 96-well black plate (P96-1.5H-N, Cellvis, Mountain View, USA) was first coated with both TNFα capture antibody (0.8 µg/ml in PBS) and IL-6 capture antibody (2 µg/ml in PBS), 100 µl/well, and incubated overnight at 4^{o}C. The plate was washed three times with 1x PBS and then blocked with 200 µl of reagent diluent (1x PBS in 1% BSA, 0.2µm filtered). After blocking the plates were washed three times with PBS. JAWS II dendritic cells (ATCC® CRL-11904™) were cultured in alpha minimum essential medium with ribonucleosides, deoxyribonucleosides, 4 mM L-glutamine, 1 mM sodium pyruvate and 5 ng/ml murine GM-CSF, 10% heat-inactivated fetal bovine serum, 50 IU/ml of penicillin, 50 µg/ml of streptomycin. JAWS II DCs were seeded on the capture coated plates, at the seeding density of 5,000 cells/well in 100 µl of medium followed by incubation at 37^{o}C in 5% CO_2 for 30 minutes. All the non-adherent cells were removed by taking out the medium and replacing it with 100 µl of fresh medium containing 200 ng/ml of LPS. The cells were incubated at 37^{o}C in 5% CO_2 for 30 minutes, 1 hour, 2 hours, and 3 hours. The wells with medium and without LPS were incubated for 3 hours. Subsequently, the medium was decanted, and cells were fixed using 100 µl/well of 4% neutral buffered formalin (NBF) for 20 minutes at room temperature. The plates were then washed three times with PBS and incubated with biotinylated detection antibody conjugated plasmonic-fluors (TNFα-detection antibody conjugated Cy5-plasmonic-fluor and IL-6 detection antibody conjugated Cy3-plasmonic-fluor: extinction 0.5) in reagent diluent for 2 hours at room temperature. The plates

were washed three times using PBS and the nuclei of the cells were stained with 300 nM DAPI solution (Millipore Sigma, St. Louis, MO, USA) for 5 minutes at room temperature in dark. Finally, the plates were washed three times in PBS and imaged using Nikon TsR2 epifluorescence microscope.

FluoroDOT assay using Mtb-infected BMDMs: Mouse TNFα DuoSet ELISA kit (R&D systems, catalog number DY410, lot number P189768) was used for this assay. Glass-bottom 96-well black plate (P96-1.5H-N, Cellvis, Mountain View, USA) was first coated with capture antibodies (0.8 µg/ml in PBS), 100 µl/well and incubated overnight at 4^{o}C. The plate was washed 3 times with 1x PBS and then blocked with 200 µl of reagent diluent (1x PBS in 1% BSA, 0.2 µm filtered). After blocking the plates were washed three times with PBS. BMDMs were seeded on the capture coated plates, at the seeding density of 5,000 cells/well in 100 µl of medium followed by incubation at 37^{o}C in 5% CO_2 for 30 minutes. All the non-adherent cells were removed by taking out the medium and replacing it with 100 µl of fresh medium containing DsRed-expressing *Mtb* strains at MOI of ~5. The cells were incubated at 37^{o}C in 5% CO_2 for 3 hours, then the supernatant was replaced and incubated for another 3 hours. Subsequently, the medium is decanted, and the cells were fixed using 100 µl/well of 1% paraformaldehyde (PFA) in PBS, overnight at 4^{o}C. The plates were then washed three times with PBS and incubated with biotinylated detection antibodies (75 ng/ml in reagent diluent for 2 hours at room temperature. The plates were washed three times using PBS and were incubated with 100 µl/well of streptavidin Cy5-plasmonic-fluors (extinction 0.5) for 30 minutes at room temperature in dark. The plates were washed with PBS 3 times and the nuclei of the cells were stained with 300 nM DAPI solution (Millipore Sigma, St. Louis, USA) for 5 minutes at room temperature in dark.

Finally, the plates were washed three times in PBS and imaged using Nikon TsR2 epifluorescence microscope.

FluoroDOT assay using BMDC and T cell co-cultures: Mouse IFNγ DuoSet ELISA kit (R&D systems, catalog number DY485-05, lot number P234214) was used for this assay. Glass-bottom 96-well black plate (P96-1.5H-N, Cellvis, Mountain View, USA) was first coated with capture antibodies (4 µg/ml in PBS), 100 µl/well and incubated overnight at 4^{o}C. The plate was washed three times with 1x PBS and then blocked with 200 µl of reagent diluent (1x PBS in 1% BSA, 0.2µm filtered). After blocking, the plates were washed three times with PBS. Wild-type and mismatch BMDCs were seeded on the capture coated plates, at the seeding density of 5,000 cells/well in 100 µl of medium followed by incubation at 37^{o}C in 5% CO_2 for 30 minutes. All the non-adherent cells were removed by taking out the medium and replacing it with 100 µl of fresh medium containing either DsRed-expressing *Mtb* strains at MOI of ~5 or LPS (1,000 ng/ml). Incubate the cells at 37^{o}C in 5% CO_2 for 24 hours. Mycobacterium tuberculosis (*Mtb*) MHCII-peptide (P25)-specific GFP-expressing $CD4^+$ T cells were prepared as reported previously.[111] LPS treated BMDCs were treated with 791 ng/ml of P25 peptide. GFP expressing $CD4^+$ T cells (50,000 cells per well in 100 µl) were added to infected BMDCs, for 3 hours. For time-dependent study, the plates were incubated for 1 hour, 2 hours and 3 hours. Since T cells are non-adherent, after completion of the incubation duration, the plate was spun at 1100 rpm for 5 minutes. The medium was decanted, and the cells were fixed using 100 µl/well of 1% paraformaldehyde (PFA) in PBS, overnight at 4^{o}C. The plates were then gently washed two times with PBS and incubated with biotinylated detection antibodies (200 ng/ml in reagent diluent for 2 hours at room temperature. The plates were gently washed two times using PBS and then were incubated with 100 µl/well of streptavidin Cy5-plasmonic-fluors (extinction 0.5) for

30 minutes at room temperature in dark. The plates were gently washed with PBS 2 times, and the nuclei of the cells were stained with 300 nM DAPI solution (Millipore Sigma, St. Louis, USA) for 5 minutes at room temperature in dark. Finally, the plates were gently washed two times in PBS and imaged using Nikon TsR2 epifluorescence microscope.

Quantification and statistical analysis: For analyzing the statistical difference between more than two groups, one-way analysis of variance (ANOVA) with a post-hoc Tukey's honest significance test was used. Statistical significance of the data was calculated at 95% ($p<0.05$) confidence intervals. All values are expressed as mean ± standard deviation. GraphPad Prism 6 was used for all statistical analysis. Linear regression was used to calculate the equation and to derive the slope of fluorescence intensity vs. molar concentration graph. 4-parameter logistic (4-PL) was used to calculate the R^2 values and LOD in the standard curves of immuno-assays. The LOD is defined as the analyte concentration corresponding to the mean fluorescence intensity of blank plus three times of its standard deviation (mean+3σ). For FluoroDOT assay, all measurements were taken from distinct samples as well as different regions of the same sample.

3.5 Figures

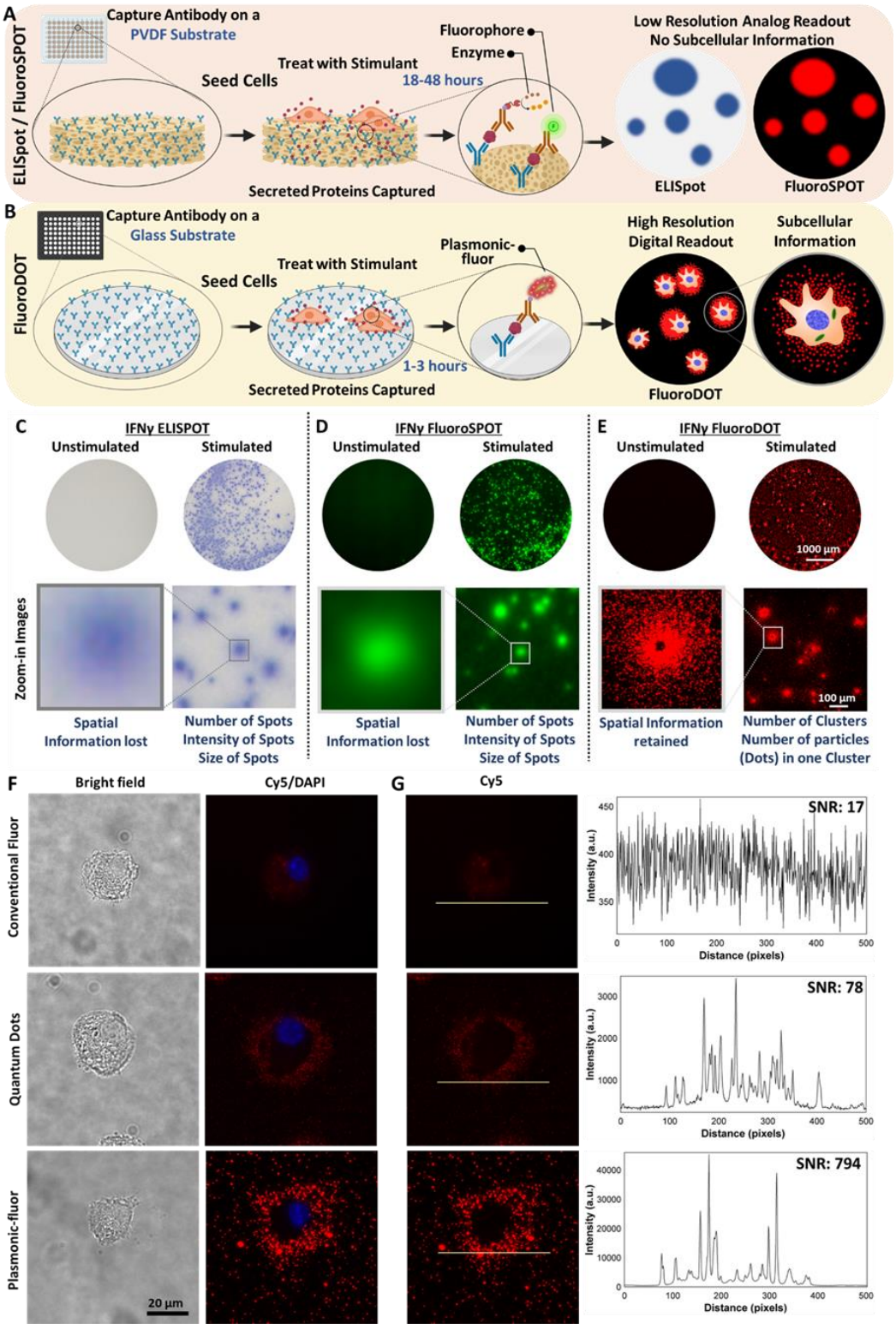

Figure 3.1 Comparison of conventional ELISpot/FluoroSpot assays with plasmon-enhanced FluoroDOT assay relying on plasmonic-fluors as ultrabright biolabels. Schematic

illustration depicting step-by-step method for **A**) conventional ELISpot and FluoroSpot assays, and **B**) plasmon-enhanced FluoroDOT assay. Representative whole well and zoomed-in images of PBMCs IFNγ assay **C**) ELISpot, **D**) FluoroSPOT and **E**) FluoroDOT. The cells were incubated for 18 hours for comparison of all three assays. **F**) JAWS II DCs were treated with 200 and 2000 ng/ml lipopolysachharide (LPS) and bright field images (left panel), Cy5/DAPI merged images (middle panel) of a single cell secreting TNFα, visualized using conventional fluor (Cy5), quantum dot 655 and Cy5-plasmonic-fluor and **G**) Representative line-scans and signal-to-noise ratio (SNR) corresponding to conventional fluor (Cy5), quantum dot 655 and Cy5-plasmonic-fluor. To assess the signal of the secreted cytokine, the line scans for all the fluors are placed just outside the boundary of the cell (using the corresponding brightfield image). High power laser (Lumencor Aura III Light Engine) was used as light source. Standard Cy5 filter was used to image all three labels. See also Figure S1 and S2.

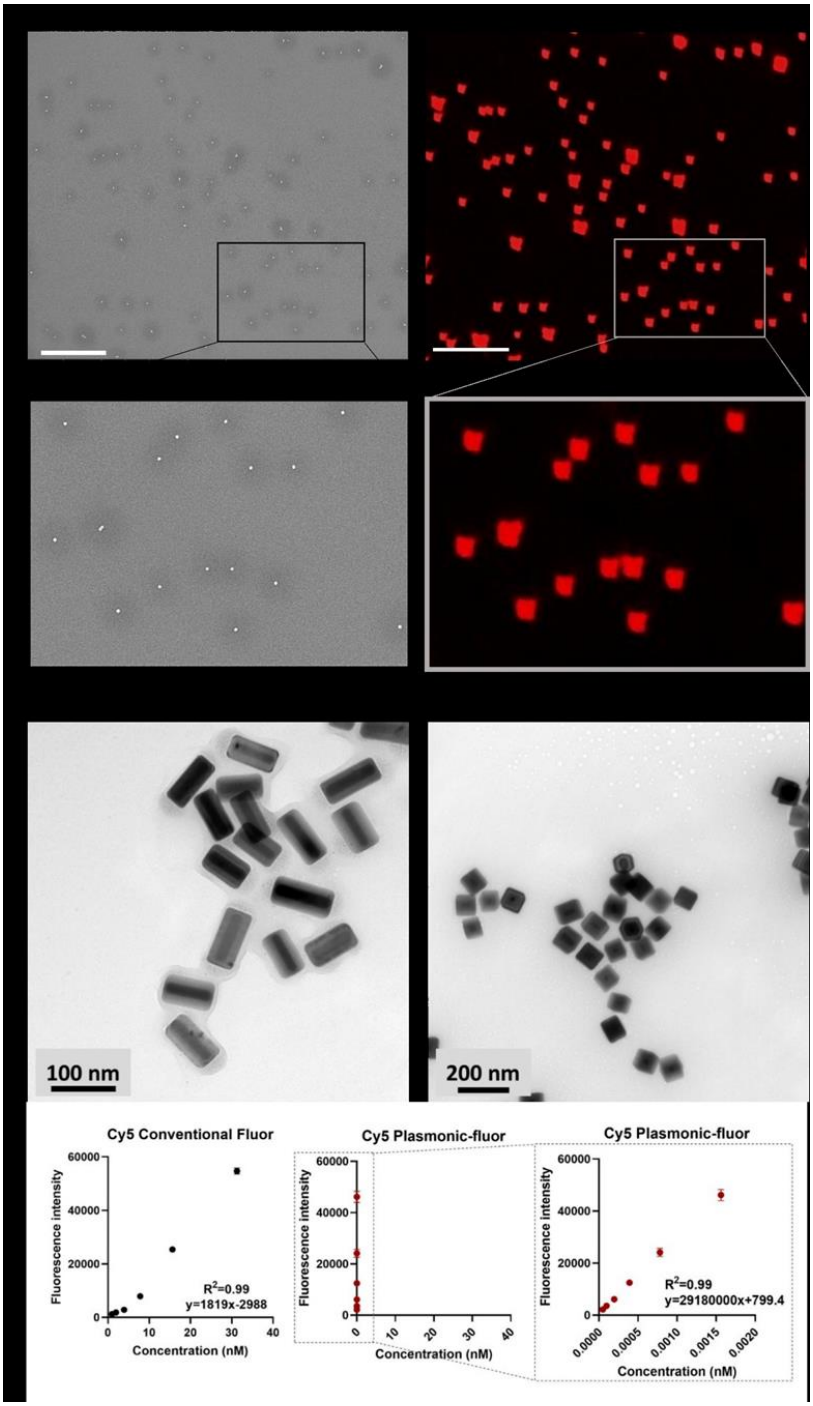

Figure 3.2 A) Scanning electron microscopic images (left) and epifluorescence microscopy images (right) from the same regions of substrate drop-casted with plasmonic-fluors showing one-to-one correlation of individual plasmonic-fluors between the two images. Scale bar: 5 µm.

B) Transmission electron microscopy images of streptavidin Cy5-plasmonic-fluor and streptavidin Cy3-plasmonic-fluor. **C**) Fluorescence intensity of Cy5 conventional fluor and Cy5-plasmonic-fluor at their different molar concentrations. Data represented as mean ± s.d ($n = 2$ repeated tests). The data was fitted and graphically presented on a linear scale.

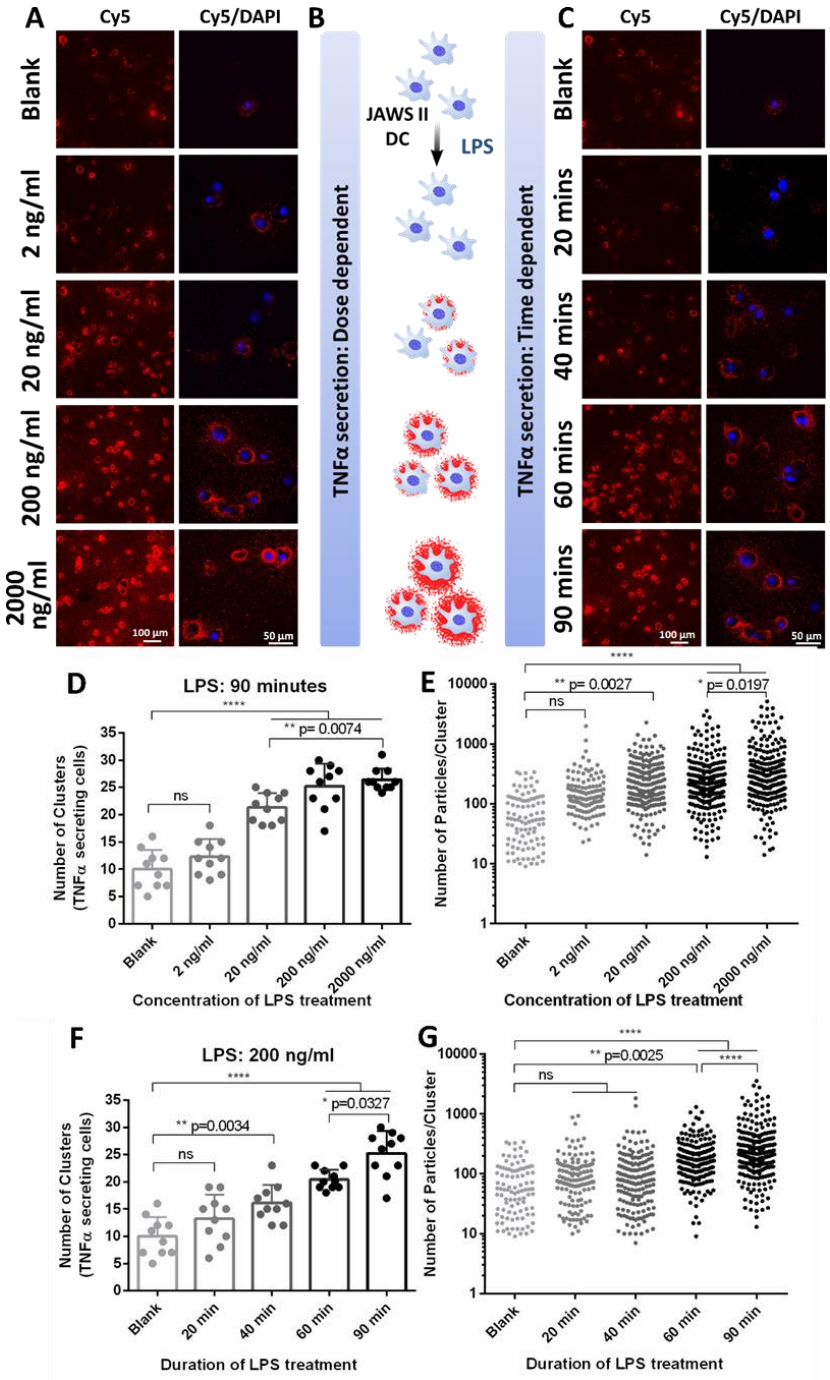

Figure 3.3 Studying the effect of stimulant dose and stimulation duration on single-cell protein secretions. FluoroDOT assay performed on JAWS II dendritic cells treated with a) 0, 2, 20, 200 and 2000 ng/ml lipopolysachharide (LPS) for 90 minutes and c) 200 ng/ml of LPS

treated for 20 minutes, 40 minutes, 60 minutes and 90 minutes. **A**) and **C**) Left panel: Cy5 epifluorescence microscopy images of the assay using Cy5-plasmonic-fluor. Scale bar: 100 µm. a) and c) Right panel: Cy5/DAPI merged image of TNFα secreting cell visualized using Cy5-plasmonic-fluor at 60x. Scale bar: 50 µm. **B)** Illustration depicting the LPS treatment of JAWS II dendritic cells for studying the secretion levels of TNFα in a dose and time-dependent manner. Quantification of the number of TNFα secreting cells and the amount of TNFα secreted by individual cells with (**D, E**) increasing dose of LPS and (**F, G**) increasing duration of LPS treatment. Ten, 20x images for each treatment condition were collected. 700-750 cells were analyzed. Each data point is the number of clusters in the field of a 20X image. The fields were randomly chosen. There were at least 10 cells in each field of view.ns: not significant, **$p<0.01$, ***$p<0.001$, ****$p<0.0001$ by one-way ANOVA and Tukey's post test.

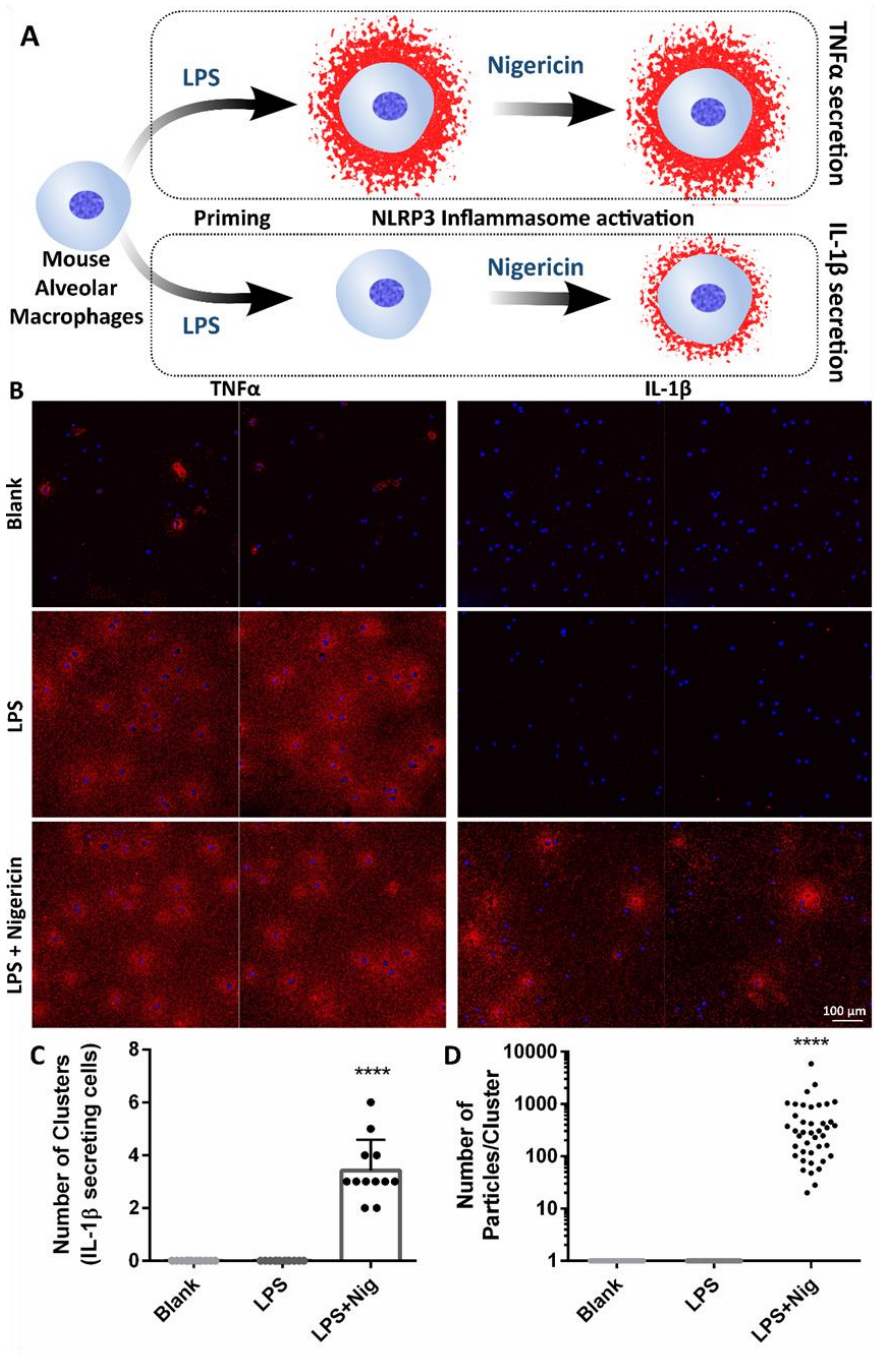

Figure 3.4 Detection of two secreted proteins in primary cells after multiple stimulants. A) Illustration depicting the experiment performed using alveolar macrophages to study the effect of two stimulants (LPS and nigericin) on the secretion of TNFα and IL-1β. Plasmon-enhanced FluoroDOT assay performed on mouse-derived alveolar macrophages treated with 500 ng/ml LPS with and without nigericin for inflammasome activation. **B**) TNFα secretion and IL-1β

secretion observed after 4 hours of LPS treatment and 30 minutes of 20 μM nigericin treatment. Cy5 epifluorescence microscopy images of the assay using Cy5-plasmonic-fluor (red) overlaid with DAPI nuclei stain (blue). Each panel contains two representative 20x images stitched together. Scale bar: 100 μm. Quantification data showing **C**) the number of cells secreting IL-1β and **D**) the amount of IL-1β secreted by individual cells after inflammasome activation. Number of clusters and number of particles/cluster were calculated using twelve, 20x images for each treatment condition. ****$p<0.0001$ by one-way ANOVA and Tukey's post test.

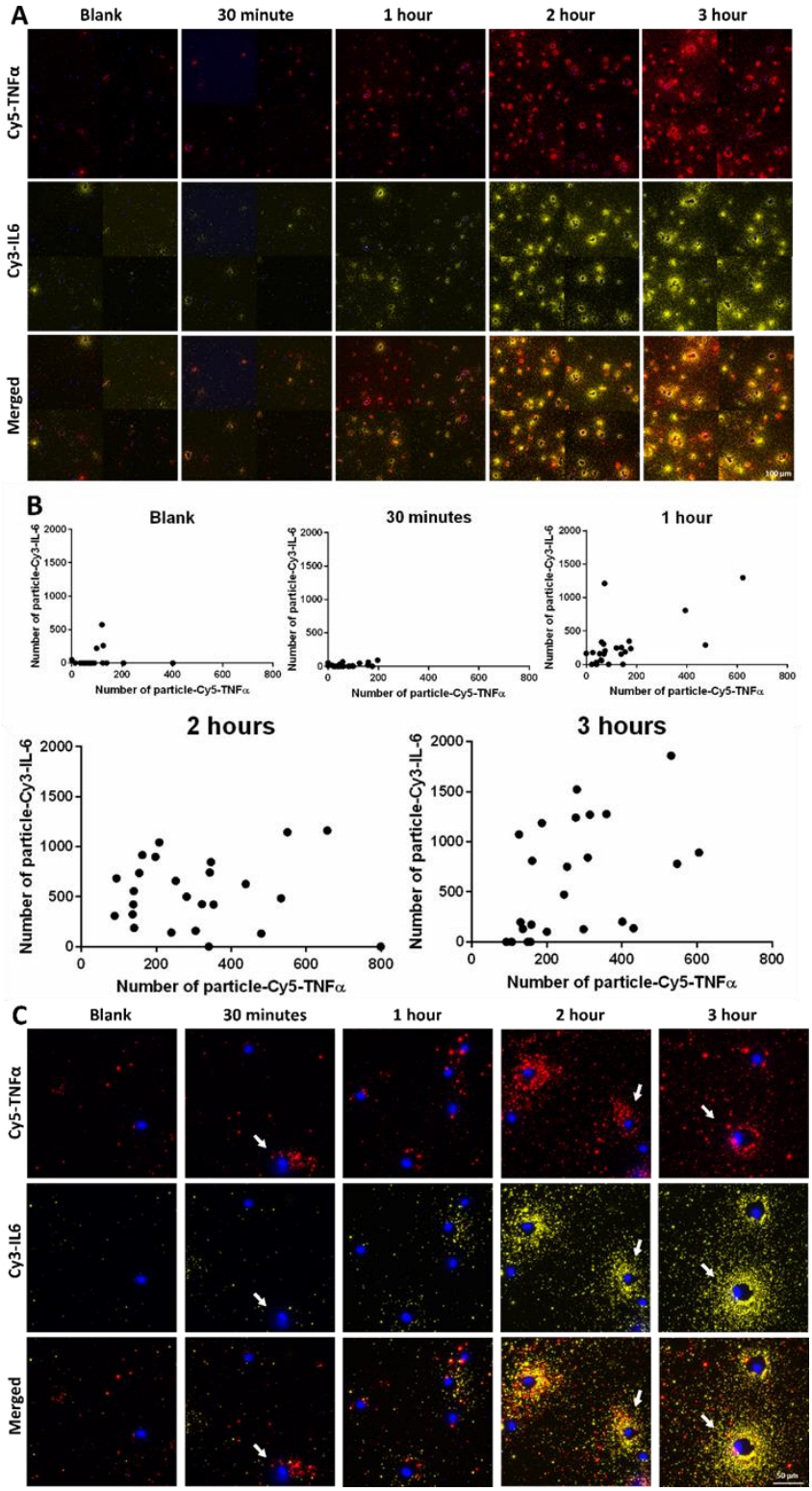

Figure 3.5 Multiplexed analysis of secretion of two proteins in the same cell using antibody conjugated plasmonic-fluors. A) Multiplexed analysis of secretion of TNFα and IL-6 from single JAWS II DC when subjected to 200 ng/ml LPS after 30 min, 1 hour, 2 hours, and 3 hours

of incubation. Epifluorescence microscopy images of the cells using TNFα detection antibody conjugated cy5-plasmonic-fluor (red) and IL-6 detection antibody conjugated cy3-plasmonic-fluor (yellow) overlaid with DAPI nuclei stain (blue). Each panel contains four representative 20x images stitched together. Scale bar: 100 μm **B**) Quantification of both TNFα and IL-6 from individual JAWS II DC after LPS treatment for 30 minutes, 1 hour, 2 hours, and 3 hours. Number of clusters and number of particles/cluster were calculated using seven, 20x images for each treatment condition. **C**) Representative higher magnification images (60x) of JAWS II DCs showing the multiplexed detection of the TNFα and IL-6 secretion and the associated cell-to-cell heterogeneity indicated by white arrows. Scale bar: 50 μm.

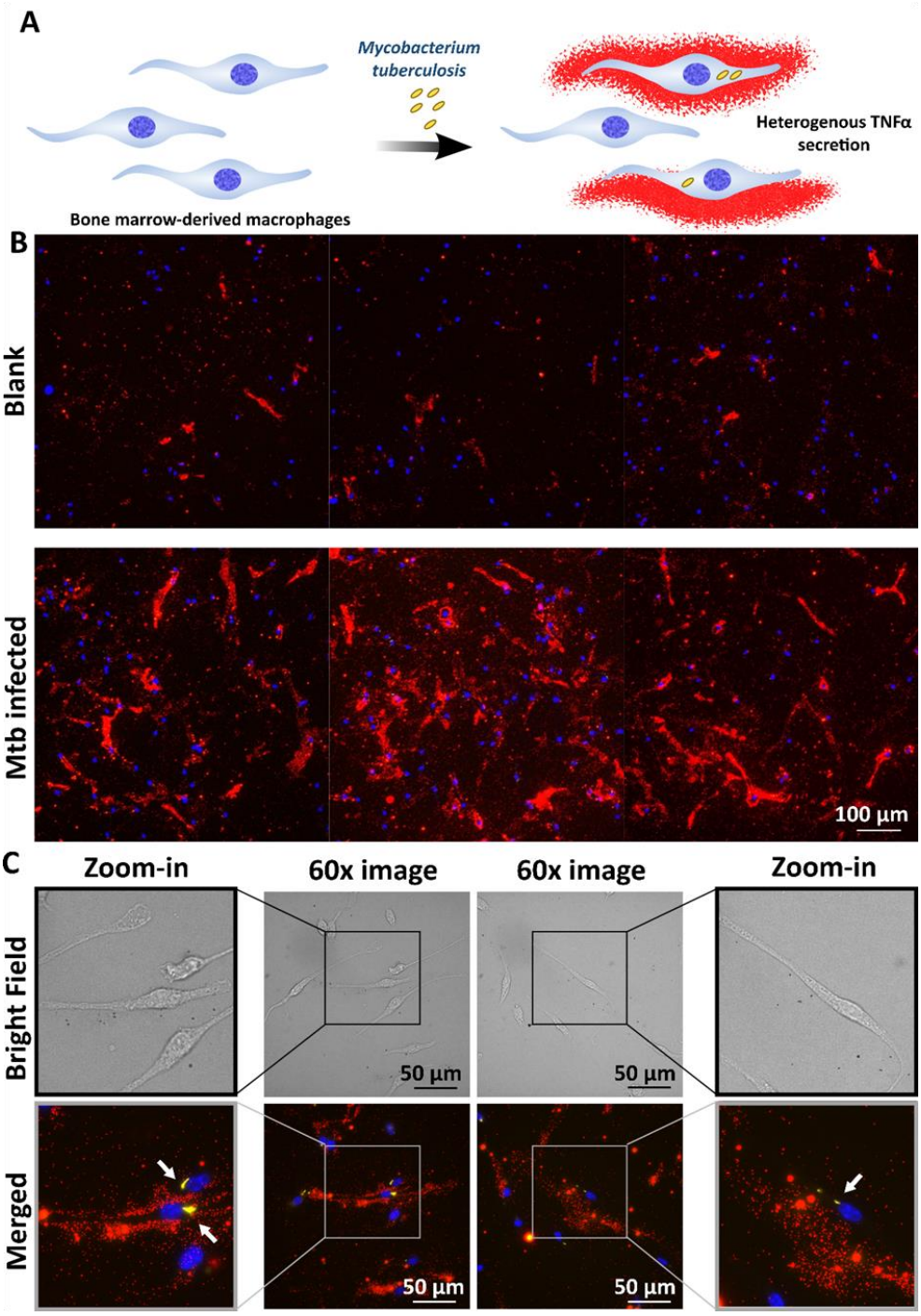

Figure 3.6 Cell-to-cell heterogeneity in cytokine secretion after *Mtb* infection. A) Illustration depicting the heterogeneity in TNFα secretion in terms of infection amount and direction of secretion by bone marrow-derived macrophages (BMDMs) infected with *M. tuberculosis* (*Mtb*). **B**) Plasmon-enhanced FluoroDOT assay for TNFα secretion from BMDMs in the absence and presence of DsRed-expressing *Mtb*. Epifluorescence microscopy images of the assay using Cy5-

plasmonic-fluor (red) overlaid with *Mtb* (yellow) and DAPI nuclei stain (blue). Each panel contains three representative 20x images stitched together. Scale bar: 100 µm. **C**) Bright field and Cy5/TRITC/DAPI merged images at 60x with a zoom-in image on either side. Presence of *Mtb* is highlighted by white arrows. Scale bar: 50 µm.

Chapter 4: Plasmon-enhanced flow cytometry

4.1 Introduction

Flow cytometry is a powerful cell analysis tool employed to identify and characterize single cells. This technique is extensively employed in immunophenotyping biological specimens with applications in various fields ranging from immunology, molecular biology, and infectious diseases to cancer biology[27,112-114]. A critical tool for decrypting cell systems for diagnostics and sorting are the cell surface antigens characterized to perform specific cellular functions[27]. An important discovery highlighted the correlation between surface protein cellular function and their abundance, indicating that ~65% of target antigens represent <5,000 copies per cell[24,27]. Briefly, surface proteins involved in functions such as cell communication, regulation of cellular processes, protein sorting in post-transcriptional processing, and metabolic processing were identified to lie in a low abundance regime (<5,000 copies)[24]. While high-abundant surface proteins (high copy numbers) can feasibly be investigated via standard flow cytometry protocols that rely on antibody-conjugated fluorescent labeling, low-abundant proteins are disregarded owing to the poor sensitivity and precision of the techniques. For example, one study estimated the need for >5,000 fluorescein molecules for specifically detecting the "positive signal" from target cell surface antigens having accounted for the auto-fluorescence and background fluorescence from "negative" cell populations[16,27]. Clearly, there is an imminent need to overcome the limitation associated with dim fluorescence signals, poor sensitivity, and non-specific binding.

Considering the growing list of fluorophores, it is critical to select the most suitable fluorophore for probing cell surface target antigens via flow cytometry. While categorizing and selecting cell surface antigens to be probed based on their expression level (copy number) is necessary for optimal results, it is equally important to designate an appropriate fluorophore to label target antigen[112]. Furthermore, building an appropriate fluorophore panel is imperative for performing multiparameter flow cytometry to probe multiple markers on single cells. Though complexity rises in multiparameter flow cytometry experiments, using fluorophores for detecting multiple markers proves advantageous in accurately determining cell population distributions[113]. A comprehensive guide for selecting fluorophores considers the following parameters: (a) relative brightness profile of fluorophore, (b) excitation and emission profile matching the optical configuration of flow cytometer instrument, (c) fluorescence emission overlaps to avoid spillover in adjacent channels, (d) stability of fluorophore-antibody conjugates, (e) reproducibility and reliability of antibody-conjugation to fluorophore[113,115,116]. The need to consider these factors in choosing the appropriate fluorophore for flow cytometry is further necessitated by the lack of ultrabright and ultrasensitive nanolabels that can effectively detect low-abundant receptors on the cell surface[27,115]. For example, several important interleukin (IL) receptors such as IL-2, IL-4, IL-6, and IL-12 are found to be expressed at as low as 100-1,000 copies/cell (very low-abundant), highlighting the need for ultrabright fluorescent nanolabels capable of detecting "positive" cell surface target antigens[27,117-119]. Therefore, it is important to consider the type and the number of surface antigens to be probed via flow cytometry for effective cell analysis

While flow cytometry is one of the most widely employed technique for investigating and analyzing cellular systems, a persisting challenge revolves around the poor sensitivity of the technique. A sensitive flow cytometry technique will demonstrate the capability of accurately

detecting “positive” cell population expressing target antigens, beyond the background and autofluorescence signals, therefore quantitatively and qualitatively distinguishing differences between cell populations[16,112,114]. Conventionally, flow cytometry experiments have been designed with molecular fluorochromes (eg. FITC, Alexa Fluor 488, Texas Red, PerCP, PE) exhibiting consistent emission spectra, high stability, and reproducible conjugation to antibodies[3,115].

The introduction of quantum dots (QDs) in conjunction with flow cytometry has supported new findings in the field of cell analysis, owing to numerous advantages. Briefly, QDs demonstrate excellent emission wavelength tunability (size), therefore supporting efficient multiparameter flow cytometry experiments[120]. In addition, QDs exhibit significantly brighter fluorescence readout (quantum yield ~90%) relative to common organic fluorochromes (quantum yield <30%)[120-125]. Furthermore, multicolor flow cytometry is expected to benefit from the use of QDs owing to a symmetrical emission spectra and minimal spillover, in contrast to molecular fluorophores[120,122]. Despite the above-listed advantages, there are a few limitations associated with QDs related to failure in achieving successful antibody conjugation to QDs, higher overhead cost of QDs, and poor stability, impacting the adoption rate of this staining technology by the flow cytometry community[120].

Here we demonstrate ultrasensitive and quantitative detection of target antigens on cell surface through plasmon-enhanced flow cytometry and analysis. We demonstrate the excellent compatibility and utility of an ultrabright fluorescence nanolabel, termed plasmonic-fluor, with conventional flow cytometer. Using a model system based on dendritic cells, we demonstrate that plasmonic-fluors can be used for quantitative and qualitative characterization of various cell surface antigens via flow cytometry. First, we establish the sensitivity of plasmon-enhanced flow

cytometry in achieving 20-fold higher fluorescence signal compared with conventional flow cytometry relying on molecular fluorophores and quantum dots. Second, we determined the optimal condition of antibody-conjugated plasmonic-fluors by designing an innovative conjugation approach. Last, we validated the application of antibody-conjugated plasmonic-fluors in multiparameter flow cytometry by probing a pair of cell surface expressed antigens on our model system. This ultrabright, ultrasensitive and quantifiable approach may enable investigation of novel cellular systems including low-abundant cell surface antigens.

4.2 Results and discussion

Addressing the limitations of conventional flow cytometry, we propose an innovative approach termed plasmon-enhanced flow cytometry. The bio-detection technology described here is based on detecting, quantifying, and characterizing cell surface antigens by employing an ultrabright nanostructure termed plasmonic-fluor. We have recently developed an ultrabright fluorescent nanoconstruct termed plasmonic-fluor that exhibits ~7,000-fold enhancement in fluorescence compared to its conventional counterpart[47]. Plasmonic-fluor (PF) comprises a plasmonic nanostructure that acts as fluorescence enhancer coated with a siloxane copolymer spacer layer to prevent metal-induced fluorescence quenching and a scaffold composed of bovine serum albumin (BSA), universal bio-linker (e.g., biotin, streptavidin) and fluorophores (e.g., AF647, FITC, 800CW, IR650)[47,126]. BSA serves as a key design element by imparting high stability to the nanoparticles, minimizing non-specific binding of PFs, and assembling the functional elements to coat the PFs. By tuning the longitudinal localized surface plasmon resonance (LSPR) of the plasmonic nanostructure, PFs can be designed with any molecular fluorophore to emit over a broad range of electromagnetic wavelength (e.g., PF-800CW, PF-Cy5, PF-LT680, PF-IR650)[25,26,47,48].

We hypothesized that the introduction of highly stable and bright PF will provide an unprecedented advantage to flow cytometry in investigating novel cellular systems, including low-abundant cell surface antigens and establishing multiparameter flow cytometry. To investigate and compare the performance of PFs with conventional molecular fluorophores and QDs, we conducted flow cytometry experiments to probe dendritic cells (bone marrow derived dendritic cells, BMDCs). Dendritic cells (DCs) are potent antigen presenting cells (APC) that process and present antigens to T-cells to initiate immune response against pathogens[127]. Exposing immature DCs to an exogenous (lipopolysaccharide, LPS) or endogenous (oxidative stress) stimulus induces maturation in DCs resulting in amplified potency to activate T-cells[128,129]. DCs receiving the appropriate maturation stimuli upregulate the surface expressed molecules including CD80, CD40, CD86, and CD83, and chemokines that support DCs functions as APCs[127]. Therefore, investigating DCs surface for target antigen distribution, one can gain insight into the molecular profiles of immature and mature DCs, and their effectiveness in functioning as APCs[127].

In this study, we have employed plasmonic-fluor comprised of AF647 and plasmonic-fluor comprised of FITC (called PF-AF647 and PF-FITC respectively, henceforth) for exploring their compatibility and utility with flow cytometry. PF-AF647 is realized using Au@Ag nanocuboids with LSPR wavelength at ~650 nm as plasmonic nanoantenna (**Fig. 2A**). Transmission electron microscopy (TEM) image shows PF-AF647 with a length of 77 ± 6 nm and a width of 34 ± 2 nm (**Fig. 2B**).

To establish the compatibility of PFs with conventional flow cytometry protocol, we first assigned CD80 as the target antigen on BMDCs to be detected via 3 fluorescent probes, namely: Quantum dots 655 (QD655), Alexa Fluor 647 (AF647) and plasmonic-fluor-AF647 (PF-AF647).

As described above, CD80 is one of the maturation markers that is known to be expressed at differing levels on the surfaces of immature and mature BMDCs[127]. We chose AF647 owing to its high brightness ranking[130]; designed PF-AF647 with AF647 as dye fluorophore, and chose QD655 owing to its high fluorescence from the list of CdSe QDs[131]. We relied on the biotin-streptavidin interaction to label immature and mature BMDCs with biotin-conjugated anti-CD80 antibody followed by streptavidin-conjugated fluorophores. In addition, each experiment included an 'unstained' control to account for the autofluorescence, a 'no antibody' control to account for the non-specific binding of the employed fluorophore (**Fig. 2D-F**). While we observed a comparable performance of AF647 and QD655 in staining immature and mature BMDCs populations, 1.8-fold higher non-specific binding of AF647 was recorded over QD655 (**Fig. 2G**). In contrast, staining with PF-AF647 resulted in ~20-fold and ~15-fold larger cell population for immature and mature BMDCs, respectively (**Fig. 2G**). Furthermore, fluorescence readout from non-specific binding of PF-AF647 was minimized owing to the protective coating of BSA on PFs[47]. To assess the relative brightness of the 3 fluorophores, we relied on the comparison of a standard parameter named staining index[113]. Staining index (SI) is given by,

$$SI = \frac{MFI\ of\ positive\ cells - MFI\ of\ negative\ cells}{2 * standard\ deviation\ of\ negative\ cells}$$

where MFI is the mean fluorescence intensity.

Therefore, SI values of PF-AF647 were 15-fold and 35-fold higher than AF647 and QD655, respectively. The ultrabright fluorescence readout, reduced non-specific binding, and high relative SI are indicative of the compatibility of PFs with flow cytometry and their effective in delineating small differences in cell surface antigen expression levels.

To incorporate PFs into multiparameter flow cytometry, we propose an antibody conjugation approach to achieve different surface coverage of antibody on PFs by relying on biotin-streptavidin interaction. To determine the optimal amount of antibody on PFs, we varied the amounts of biotin-functionalized anti-CD80 antibody to be conjugated to streptavidin-functionalized PF-AF647 and achieved five different surface coverage densities (5%, 2.5%, 1.25%, 0.625%, and 0%) (**Fig. 3A**). As expected, we observed highest mean fluorescence intensity (MFI) in immature and mature BMDCs populations when probed with 5% anti-CD80 antibody-conjugated PF-AF647 (**Fig. 3B**). We observed a declining trend in MFI of immature and mature BMDCs when probed with decreasing surface coverage densities of anti-CD80 antibody on PF-AF647 (**Fig. 3C-E**). In addition, we observed minimal non-specific binding of pristine PF-AF647 (conjugated to 0% anti-CD80 antibody) to immature and mature BMDCs, further validating the high specificity and excellent labeling efficiency of our proposed methodology (**Fig. 3F**). We further evaluated the performance of different surface coverage antibody-conjugated PFs by using a tool named resolution metric[114,132]. Resolution metric provides a normalized difference between two populations, and is given by,

$$Resolution\ Metric = \frac{MFI\ of\ positive\ cells - MFI\ of\ negative\ cells}{Standard\ deviation\ of\ positive\ cells + Standard\ deviation\ of\ negative\ cells}$$

Resolution metric revealed 2.5% surface coverage of anti-CD80 antibody-conjugated PF-AF647 is the most optimal condition for differentiating and resolving between immature and mature BMDCs.

To determine the feasibility of using antibody-conjugated plasmonic-fluors in multiparameter flow cytometry, we synthesized two different plasmonic-fluors: PF-FITC conjugated to anti-CD40 antibody and PF-AF647 conjugated to anti-CD80 antibody, after fixation, immature and

stimulated mature BMDCs were simultaneously stained for CD40 and CD80 surface antigens using two versions of plasmonic-fluors. As expected, we observed excellent compatibility of antibody-conjugated PFs with multiparameter flow cytometry, demonstrating their ability in differentiating between immature and mature BMDCs expressing differing levels of target antigens (**Fig. 4A,B**). Moreover, we observed minimal contribution of fluorescence from non-specific binding of antibody-conjugated PFs (**Fig. SI**), highlighting the remarkable specificity and sensitivity of the employed antibody conjugation protocol. In addition, it is important to note unstained BMDCs exhibited high autofluorescence in the FITC channel compared to AF647 channel (**Fig. 4C**). Overall, we observed high MFI in immature and mature BMDCs when probed with antibody-conjugated PFs for CD40 and CD80 target antigens (**Fig. 4C**). Further analysis revealed 17-fold higher staining index of anti-CD80 antibody-conjugated PF-AF647 relative to anti-CD40 antibody-conjugated PF-FITC. On the other hand, the resolution metric of the employed antibody-conjugated PFs ranged between 0.47 - 0.62 indicative of their comparable yet remarkable performance in delineating the differences between target antigen expression levels on immature and mature BMDCs via multiparameter flow cytometry (**Fig. SI**). Additionally, by employing a gating strategy we investigated the BMDCs single cells to reveal ~99% BMDCs cells representing the autofluorescence of unstained control subset (**Fig. 4D,E**). Immature and mature BMDCs subset defined as CD40+ CD80+ were evaluated to represent ~50% and ~72% frequencies respectively (**Fig. 4F,G**).

4.3 Conclusion

In summary, we have demonstrated an ultrasensitive, ultrabright, and quantitative approach for analyzing target antigens on cell surfaces via plasmon-enhanced flow cytometry. Using a model system based on dendritic cells, we established a novel technology for efficiently probing cell

surface antigens with remarkable selectivity, surpassing the conventionally employed molecular fluorophores and quantum dots. While retaining the workflow of standard flow cytometry, plasmon-enhanced flow cytometry overcomes the limitations associated with poor brightness, high non-specific binding, and large spillover across channels with the use of fluorophores and quantum dots. Moreover, this technology demonstrated the potential to be employed in multiparameter flow cytometry, enabling the simultaneous detection of various cell surface antigens. Plasmon-enhanced flow cytometry may be broadly applicable to a wide range of biomarkers and receptors expressed on cell surfaces including low-abundant proteins. In addition, this technology may enable quantitative analysis and characterization of the sparsely distributed low-abundant proteins owing to its ultrabright fluorescent readout and minimized non-specific binding. The surface proteome offers a plethora of information that can provide a deeper insight for structure-function correlation in the cellular systems. Therefore, the demonstrated technology serves as an efficient tool for probing cell surface proteome and advancing our understanding of the cell systems.

4.4 Experimental section

Materials

$NaBH_4$ (71321), $HAuCl_4$ (520918), CTAB (H5882), $AgNO_3$ (204390), ascorbic acid (A92902), HCl (H9892), RBC lysis buffer, BSA (A7030), MPTMS (175617), APTMS (281778), TMPS (662275) were acquired from Sigma-Aldrich. NHS-PEG4-biotin (21329), 5 ml, 7000 MWCO desalting column (21329), Streptavidin-AF647 (S21374), Streptavidin-FIT (434311), Streptavidin-QD655 (Q101023MP) were acquired from Thermo Scientific. Seroblock FcR was acquired from Bio Rad (Cat. #-BUF041A). Anti-Mouse CD80 - biotin (reference number 13–

0801, Clone 16-10A1) and anti-mouse CD40-biotin (reference number 13-0401-82, clone number 1C10) were acquired from Invitrogen.

Synthesis of plasmonic-fluor

To synthesize plasmonic-fluor with high brightness, it is important to choose an "on-resonant" plasmonic nanostructure for a given fluorophore. Therefore, we employed Ag@AuNR with LSPR ~640 nm for synthesizing PF-AF647 and Ag@AuNS with LSPR ~510 nm for synthesizing PF-FITC.

Briefly, AuNRs were synthesized by seed-mediated method[133]. First, Au seed was prepared by adding 0.6 ml (10mM) ice-cold NaBH4 solution to a solution containing 0.25 ml of HAuCl4 (10 mM) and 9.75 ml of CTAB (0.1 M) under vigorous stirring at room temperature. The color of the solution changed from yellow to brown indicating the formation of Au seed. For the synthesis of AuNR, the growth solution was prepared by the sequential addition of aqueous HAuCl4 (0.01 M, 2 ml), CTAB (0.1 M, 38 ml), AgNO3 (0.01 M, 0.5 ml), HCl (1 M, 0.8 ml) and ascorbic acid (0.1 M, 0.22 ml) followed by gentle inversion to homogenize the solution. Subsequently, 5 μl of the seed solution was added into the growth solution and left undisturbed in the dark for 24 h. The AuNR solution was centrifuged at 7,000 r.p.m. for 40 min to remove the supernatant and the AuNR was re-dispersed into nanopure water to achieve a final peak extinction of ~2.0.

The AuNR with an LSPR wavelength around 711 nm was employed as the core for the synthesis of AuNR@Ag nanostructures. Specifically, 3 ml of AuNR (peak extinction ~4) was incubated with 8 ml of CTAC (20 mM) at 60 °C for 20 min under stirring. Then, 8 ml of AgNO3 (4 mM), 4 ml of CTAC (20 mM) and 0.8 ml of ascorbic acid (0.1 M) were added sequentially and the mixture was incubated at 60 °C for 4 h under magnetic stirring to form AuNR@ Ag

nanocuboids. Finally, AuNR@Ag nanocuboids solution was centrifuged at 6,000 r.p.m. and the nanocuboids were re-dispersed in nanopure water.

BMDCs isolation and cell culture

Five-six-week-old female C57BL/6 (H-2b) mice were purchased from Jackson Labs and maintained under pathogen-free conditions. All experiments employing mice were performed in accordance with laboratory animal protocol approved by the School of Medicine Animal Studies Committee of Washington University in St. Louis. Mice were euthanized using CO_2 asphyxiation and cervical dislocation. The euthanized mice were wiped clean with 70% (v/v) ethanol. Both the femurs and tibiae were isolated, and the muscle attachments were carefully removed using tweezers and gauze pads. Both ends of the bones were carefully cut with scissors and the marrow was centrifuged in an adapted centrifuge tube (0.6 ml tube with a hole inserted in 1.5 ml tube) at 1,000 r.p.m. for 10 s. The cell pellet was immediately resuspended in RPMI 1640 media. A single-cell suspension was prepared by passing the cells were passed through a 70 μm cell strainer. After one wash (1,200 r.p.m., 5 min), red blood cells were depleted with RBC lysis buffer. The bone marrow cells were collected and cultured in 100 mm Petri dishes for 7 days, containing 10 ml of RPMI medium supplemented with 10% heat-inactivated fetal bovine serum, 50 IU ml^{-1} of penicillin, 50 μg ml^{-1} of streptomycin and 20 ng ml^{-1} of mouse recombinant granulocyte-macrophage colony-stimulating factor (R&D Systems). BMDCs (1×10^6) were cultured in six-well plates. Mature BMDCs were achieved by stimulating with 1 ml of 1 μg ml^{-1} of LPS for 24 h. Cells were collected using a cell scraper for further staining and flow cytometry analysis.

Immunohistochemistry and flow cytometry analysis

CD80 overexpressed on the cell surface was probed using conventional molecular fluorophore, quantum dots and plasmonic-fluor. Specifically, immature and mature BMDCs were washed once with 1X PBS to remove the culture medium (centrifugation at 2,000 r.p.m. for 5 min) and fixed using 4% neutral buffered formalin for 20 min. The cells were then washed (2,000 r.p.m. for 5 min) and blocked with Seroblock FcR for 10 minutes. Next, biotinylated CD80 primary antibody was added into the BMDC suspension to achieve a final antibody concentration of 100 ng ml^{-1} and the mixture was incubated for 1 h. The BMDCs were washed twice (2,000 r.p.m. for 5 min) with 1% BSA and subsequently incubated with fluorophore for 1 hour. Briefly, we used molecular fluorophores (AF647, FITC) at a concentration of 1 μg ml^{-1}, QD655 at 10 nM, PF-AF647 at 400 pM, and PF-FITC at 150 pM. Finally, the cells were washed to remove unbound fluorophores. Ten thousand cells were analyzed by ACEA NovoCyte Flow Cytometer to acquire the fluorescence signal (APC channel (excitation laser 633 nm; filter 660/20 nm) and FITC channel (excitation laser 488 nm; filter 525/50 nm)) in combination with forward scatter and side scatter.

4.5 Figures

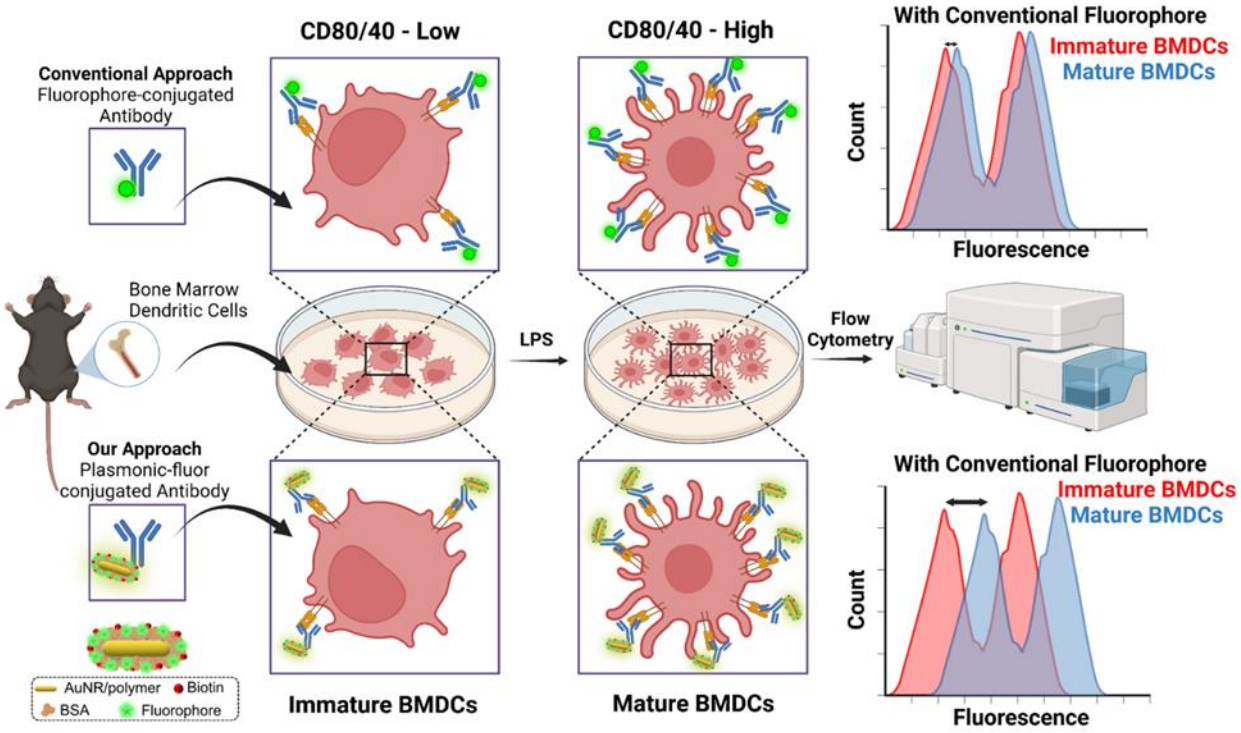

Figure 4.1 Schematic illustration depicting step-by-step protocol for differentiating between cell populations expressing surface antigens (immature BMDCs) at low levels and high levels (mature BMDCs, post-stimulation via LPS), using **A**) conventional flow cytometry approach employing a fluorophore-conjugated antibody and **B**) our proposed flow cytometry approach employing plasmonic-fluor-conjugated antibody.

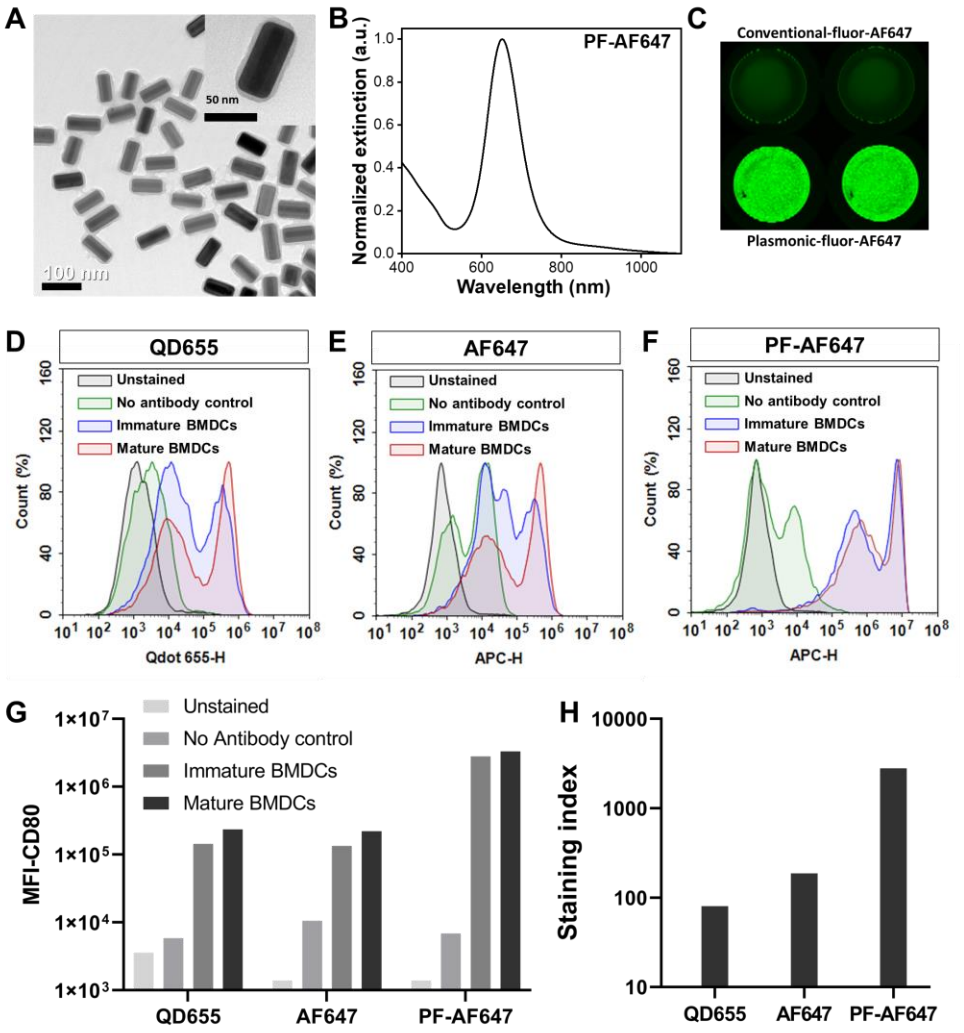

Figure 4.2 A) TEM image of PF-AF647 with inset showing the core plasmonic nanostructure and the outer shell composed of the spacer layer and BSA-biotin-dye conjugate. **B**) Vis-NIR spectrum of PF-AF647. **C**) Fluorescence intensity of AF647-streptavidin and PF-AF647-streptavidin showing an average of 700-fold enhancement in fluorescence intensity. **G**) Plot showing CD80 mean fluorescence intensity for the employed fluorophores. **H**) Plot showing the staining index values for the employed fluorophores, highlighting the brightness ranking of PF-AF647 is 15-fold higher than AF647 and 35-fold higher than QD655.

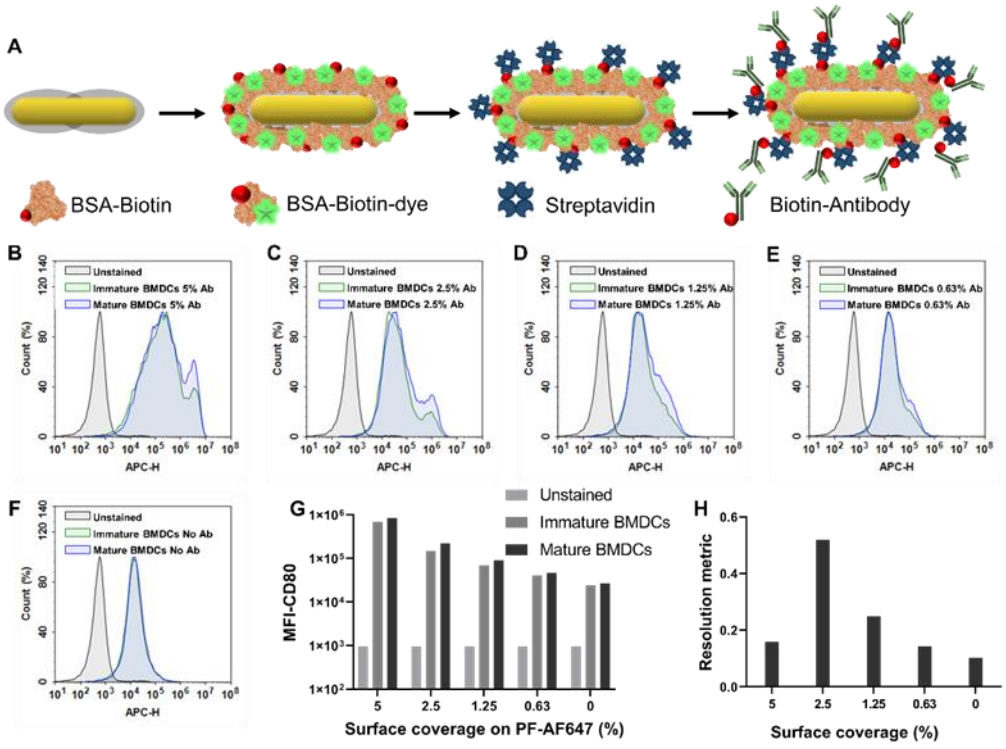

Figure 4.3 Optimizing antibody conjugation on plasmonic-fluor. A) Schematic illustrating the design workflow of modifying the spacer layer modified plasmonic nanostructure to achieve biotin-PF, streptavidin-PF, and subsequently antibody-conjugated PF. Histogram fluorescence profiles of BMDCs (immature and mature) probed using anti-CD80 antibody-conjugated PF-AF647 with **B**) 5%, **C**) 2.5%, **D**) 1.25%, **E**) 0.625% surface coverage, and **F**) pristine PF-AF647 (no antibody). **G**) MFI of anti-CD80 antibody-conjugated PF-AF647. **H**) Resolution metric of anti-CD80 antibody-conjugated PF-AF647 with different surface coverage.

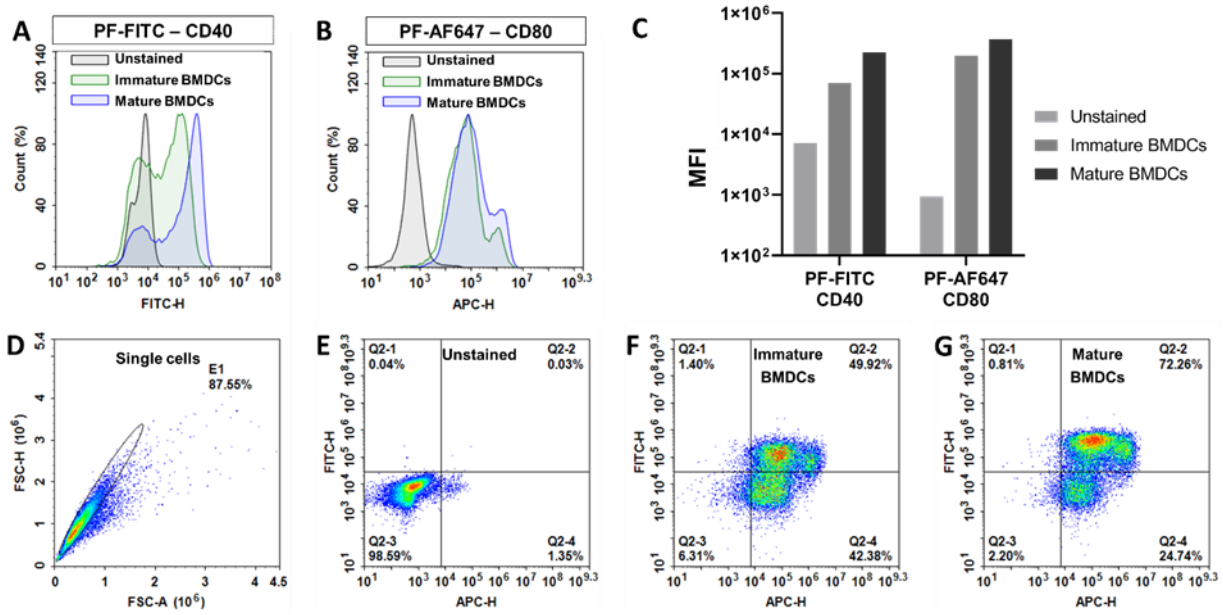

Figure 4.4 Multiparameter plasmon-enhanced flow cytometry. Histogram fluorescence profiles of BMDCs (immature and mature) probed using **A**) anti-CD40 antibody-conjugated PF-FITC, and **B**) anti-CD80 antibody-conjugated PF-AF647. **C**) MFI of anti-CD40 antibody-conjugated PF-FITC and anti-CD80 antibody-conjugated PF-AF647. **D**) Dot plot from flow cytometry analysis representing BMDCs. BMDCs E1 gated cells were analyzed for **E**) unstained control, and **F,G**) CD40-PF-FITC and CD80-PF-AF647 labeling in immature and mature BMDCs.

Chapter 5: Conclusion

In summary, we have designed and established plasmon-enhanced imaging and analytical methodologies for ultrasensitive probing of single cells. Specifically, this work was aimed at improving the sensitivity and resolution capabilities of conventionally employed bioanalytical techniques by employing ultrabright plasmonically-active nanostructures designed to take advantage of plasmon-enhanced fluorescence.

We have demonstrated a high-resolution bioimaging approach for investigating hippocampal neuron cells via plasmon-enhanced expansion microscopy. We demonstrated the excellent compatibility of plasmonic-fluor in standard expansion microscopy protocols exhibiting high fluorescence retention (nearly 85%) in post-ExM surpassing conventional molecular fluorophores (<50%). We noted excellent fidelity of p-ExM over large sample regions, indicating a uniform and isotropic expansion (expansion factor nearly 4-fold) of the neuronal network labelled with plasmonic-fluors. FImage registration analysis highlighted the minimal distortions occurring in p-ExM establishing the feasibility and reliability of the proposed methodology. More importantly, p-ExM enabled improved delineation and subsequent analysis of fine features in neural networks owing to in the improved spatial resolution. Probing neural networks in post-ExM via filament tracking analysis software (Imaris) revealed a significant increase in morphological maturation markers highlighting the superior performance of p-ExM. This high-resolution, convenient and ultrabright plasmon-enhanced expansion microscopy protocol can be broadly employed to investigate rare cell systems and identify low-abundant surface antigens.

We employed plasmonic-fluor to demonstrate a simple, ultrasensitive, and quantifiable method to probe and characterize cell populations expressing different levels of surface antigens via plasmon-enhanced flow cytometry. Using bone-marrow-derived dendritic cells in naïve (immature) state and activated (mature) state, we validated ultrabright plasmonic nanolabels in standard flow cytometry protocols. Furthermore, in contrast to molecular fluorophores and quantum dots, plasmonic-fluors exhibited a significantly improved ability to differentiate small differences in the surface-expressed CD80 levels as evidenced by brighter fluorescence readouts, low background signals, and high staining indices and resolution metrics. By determining the optimal antibody conjugation conditions on plasmonic-fluor, we further employed plasmon-enhanced flow cytometry to simultaneously probe two BMDC cell surface antigens, establishing compatibility for multiparametric analysis.

To address challenges associated with single-cell secretome analysis, we introduced an ultrasensitive digitized plasmon-enhanced FluoroDOT assay for investigating the different cytokines secreted by single cells and studying cell-to-cell heterogeneity. This versatile, low-cost, and adaptable FluoroDOT assay offers the potential to be employed for multiplexed detection and spatial mapping of proteins secreted from cells. Employing plasmonic-fluor in standard ELISspot assay resulted in a 30-fold higher signal-to-noise ratio and reduction in the LOD by two orders of magnitude when compared to conventional fluorophore biolabels. More importantly, FluoroDOT assay enables visualization of cell-to-cell heterogeneity, directionality, and protein secretion at single-cell resolution and therefore can be implemented for improved understanding of cellular interactions including immune-tumor cells and neural networks.

References

1 Combs, C. A. Fluorescence microscopy: a concise guide to current imaging methods. *Curr Protoc Neurosci* **Chapter 2**, Unit2 1, doi:10.1002/0471142301.ns0201s50 (2010).

2 Frank An, W. *Cell-Based Assays for*

High-Throughput Screening. (2009).

3 McKinnon, K. M. Flow Cytometry: An Overview. *Curr Protoc Immunol* **120**, 5 1 1-5 1 11, doi:10.1002/cpim.40 (2018).

4 Chen, F., Tillberg, P. W. & Boyden, E. S. Expansion Microscopy. *Science* **347**, 543 (2015).

5 Aslan, K. *et al.* Metal-enhanced fluorescence: an emerging tool in biotechnology. *Curr Opin Biotechnol* **16**, 55-62, doi:10.1016/j.copbio.2005.01.001 (2005).

6 Jeong, Y., Kook, Y. M., Lee, K. & Koh, W. G. Metal enhanced fluorescence (MEF) for biosensors: General approaches and a review of recent developments. *Biosens Bioelectron* **111**, 102-116, doi:10.1016/j.bios.2018.04.007 (2018).

7 Deng, W., Xie, F., Baltar, H. T. & Goldys, E. M. Metal-enhanced fluorescence in the life sciences: here, now and beyond. *Phys Chem Chem Phys* **15**, 15695-15708, doi:10.1039/c3cp50206f (2013).

8 Anker, J. N. *et al.* Biosensing with plasmonic nanosensors. *Nature Materials* **7**, 442-453, doi:10.1038/nmat2162 (2008).

9 Stranik, O., McEvoy, H. M., McDonagh, C. & MacCraith, B. D. Plasmonic enhancement of fluorescence for sensor applications. *Sensors and Actuators B: Chemical* **107**, 148-153, doi:10.1016/j.snb.2004.08.032 (2005).

10 Tam, F., Goodrich, G. P., Johnson, B. R. & Halas, N. J. Plasmonic Enhancement of Molecular Fluorescence. *Nano Letters* **7**, 496-501, doi:10.1021/nl062901x (2007).

11 Stranik, O., Nooney, R., McDonagh, C. & MacCraith, B. D. Optimization of Nanoparticle Size for Plasmonic Enhancement of Fluorescence. *Plasmonics* **2**, 15-22, doi:10.1007/s11468-006-9020-9 (2007).

12 Stranik, O., McDonagh, C. & MacCraith, B. *Plasmonic enhancement of fluorescence for sensor applications*. Vol. 5450 EPE (SPIE, 2004).

13 Schultz, S., Smith, D. R., Mock, J. J. & Schultz, D. A. Single-target molecule detection with nonbleaching multicolor optical immunolabels. *Proceedings of the National Academy of Sciences* **97**, 996-1001, doi:doi:10.1073/pnas.97.3.996 (2000).

14 Nam, J.-M., Thaxton, C. S. & Mirkin, C. A. Nanoparticle-Based Bio-Bar Codes for the Ultrasensitive Detection of Proteins. *Science* **301**, 1884-1886, doi:doi:10.1126/science.1088755 (2003).

15 Haes, A. J., Chang, L., Klein, W. L. & Van Duyne, R. P. Detection of a Biomarker for Alzheimer's Disease from Synthetic and Clinical Samples Using a Nanoscale Optical Biosensor. *Journal of the American Chemical Society* **127**, 2264-2271, doi:10.1021/ja044087q (2005).

16 Schwartz, A. & Fernandez-Repollet, E. Development of clinical standards for flow cytometry. *Ann N Y Acad Sci* **677**, 28-39, doi:10.1111/j.1749-6632.1993.tb38760.x (1993).

17 Uhlén, M. *et al.* The human secretome. *Science Signaling* **12**, eaaz0274, doi:10.1126/scisignal.aaz0274 (2019).

18 Smith, D. S., Al-Hakiem, M. H. H. & Landon, J. A review of fluoroimmunoassays and immunofluorometric assay. *Annals of Clinical Biochemistry* **18**, 253 (1981).
19 Uhlen, M., Karlson, M. J. & al., e. The human secretome. *Science* **12**, 274 (2019).
20 Yuan, G.-C. *et al.* Challenges and emerging directions in single-cell analysis. *Genome Biology* **18**, 84, doi:10.1186/s13059-017-1218-y (2017).
21 Eberwine, J., Sul, J.-Y., Bartfai, T. & Kim, J. The promise of single-cell sequencing. *Nature Methods* **11**, 25-27, doi:10.1038/nmeth.2769 (2014).
22 Spitzer, Matthew H. & Nolan, Garry P. Mass Cytometry: Single Cells, Many Features. *Cell* **165**, 780-791, doi:https://doi.org/10.1016/j.cell.2016.04.019 (2016).
23 Zenobi, R. Single-Cell Metabolomics: Analytical and Biological Perspectives. *Science* **342**, 1243259, doi:doi:10.1126/science.1243259 (2013).
24 Beck, M. *et al.* The quantitative proteome of a human cell line. *Mol Syst Biol* **7**, 549, doi:10.1038/msb.2011.82 (2011).
25 Wang, Z. *et al.* Microneedle patch for the ultrasensitive quantification of protein biomarkers in interstitial fluid. *Nat Biomed Eng* **5**, 64-76, doi:10.1038/s41551-020-00672-y (2021).
26 Seth, A. *et al.* High-resolution imaging of protein secretion at the single-cell level using plasmon-enhanced FluoroDOT assay. *Cell Rep Methods* **2**, 100267, doi:10.1016/j.crmeth.2022.100267 (2022).
27 Mori, T. & Katayama, Y. Signal amplification in flow cytometry for cell surface antigen analysis. *J Biochem* **166**, 205-212, doi:10.1093/jb/mvz052 (2019).
28 Bandura, D. R. *et al.* Mass Cytometry: Technique for Real Time Single Cell Multitarget Immunoassay Based on Inductively Coupled Plasma Time-of-Flight Mass Spectrometry. *Analytical Chemistry* **81**, 6813-6822, doi:10.1021/ac901049w (2009).
29 Hell, S. W. & Wichman, J. Breaking the diffraction resolution limit by stimulated emission:stimulated-emission-depletion fluorescence microscopy. *Optics Letter* **19**, 780 (1994).
30 Rust, M. J., Bates, M. & Zhuang, X. Sub-diffraction-limit imaging by stochastic optical reconstruction microscopy (STORM). *Nat Methods* **3**, 793-795, doi:10.1038/nmeth929 (2006).
31 Balzarotti, F. *et al.* Nanometer resolution imaging and tracking of fluorescent molecules with minimal photon fluxes. *Science* **355**, 606 (2017).
32 Hell, S. W. Far-Field Optical Nanoscopy. *Science* **316**, 1153 (2007).
33 Westphal, V. & Hell, S. W. Nanoscale resolution in the focal plane of an optical microscope. *Phys Rev Lett* **94**, 143903, doi:10.1103/PhysRevLett.94.143903 (2005).
34 Alberts B, J. A., Lewis J, et al. *Molecular Biology of the Cell*. (New York: Garland Science, 2002).
35 Neil, M. A. A., Juskaitis, R. & Wilson, T. Method of obtaining optical sectioning by using structured light in a conventional microscope. *Optics Letter* **22**, 1905 (1997).
36 Sigal, Y. M., Zhou, R. & Zhuang, X. Visualizing and discovering cellular structures with super-resolution microscopy. *Science* **361**, 880-887, doi:10.1126/science.aau1044 (2018).
37 Blom, H. & Widengren, J. Stimulated Emission Depletion Microscopy. *Chem Rev* **117**, 7377-7427, doi:10.1021/acs.chemrev.6b00653 (2017).
38 Huang, B., Wang, W., Bates, M. & Zhuang, X. Three-Dimensional Super-Resolution Imaging by Stochastic Optical Reconstruction Microscopy. *Science* **319**, 810 (2008).

39 Schmidt, R. *et al.* MINFLUX nanometer-scale 3D imaging and microsecond-range tracking on a common fluorescence microscope. *Nat Commun* **12**, 1478, doi:10.1038/s41467-021-21652-z (2021).
40 Mockl, L. & Moerner, W. E. Super-resolution Microscopy with Single Molecules in Biology and Beyond-Essentials, Current Trends, and Future Challenges. *J Am Chem Soc* **142**, 17828-17844, doi:10.1021/jacs.0c08178 (2020).
41 Tillberg, P. W. *et al.* Protein-retention expansion microscopy of cells and tissues labeled using standard fluorescent proteins and antibodies. *Nat Biotechnol* **34**, 987-992, doi:10.1038/nbt.3625 (2016).
42 Chozinski, T. J. *et al.* Expansion microscopy with conventional antibodies and fluorescent proteins. *Nat Methods* **13**, 485-488, doi:10.1038/nmeth.3833 (2016).
43 Trinks, N. *et al.* Subdiffraction-resolution fluorescence imaging of immunological synapse formation between NK cells and A. fumigatus by expansion microscopy. *Commun Biol* **4**, 1151, doi:10.1038/s42003-021-02669-y (2021).
44 Liu, J. *et al.* Expansion Microscopy with Multifunctional Polymer Dots. *Adv Mater* **33**, e2007854, doi:10.1002/adma.202007854 (2021).
45 Min, K., Cho, I., Choi, M. & Chang, J. B. Multiplexed expansion microscopy of the brain through fluorophore screening. *Methods* **174**, 3-10, doi:10.1016/j.ymeth.2019.07.017 (2020).
46 Cho, I., Sim, J. & Chang, J. B. Expansion microscopy imaging of various neuronal structures. *Methods Cell Biol* **161**, 83-103, doi:10.1016/bs.mcb.2020.06.003 (2021).
47 Luan, J. *et al.* Ultrabright fluorescent nanoscale labels for the femtomolar detection of analytes with standard bioassays. *Nat Biomed Eng* **4**, 518-530, doi:10.1038/s41551-020-0547-4 (2020).
48 Wang, Z. *et al.* Plasmonically-enhanced competitive assay for ultrasensitive and multiplexed detection of small molecules. *Biosens Bioelectron* **200**, 113918, doi:10.1016/j.bios.2021.113918 (2022).
49 Gupta, P. *et al.* Neuronal Maturation-dependent Nano-Neuro Interaction and Modulation. doi:10.1101/2022.08.03.502650 (2022).
50 Dante, S. *et al.* Selective Targeting of Neurons with Inorganic Nanoparticles: Revealing the Crucial Role of Nanoparticle Surface Charge. *ACS Nano* **11**, 6630-6640, doi:10.1021/acsnano.7b00397 (2017).
51 Pereiro, I., Fomitcheva-Khartchenko, A. & Kaigala, G. V. Shake It or Shrink It: Mass Transport and Kinetics in Surface Bioassays Using Agitation and Microfluidics. *Anal Chem* **92**, 10187-10195, doi:10.1021/acs.analchem.0c01625 (2020).
52 Sotnikov, D. V., Zherdev, A. V. & Dzantiev, B. B. Mathematical Modeling of Bioassays. *Biochemistry (Mosc)* **82**, 1744-1766, doi:10.1134/S0006297917130119 (2017).
53 Stenberg, M. & Nygren, H. Kinetics of antigen-antibody reactions at solid-liquid interfaces. *Journal of Immunological Methods*, 3 (1988).
54 Wang, G., Driskell, J. D., Porter, M. D. & Lipert, R. J. Control of Antigen Mass Transport via Capture Substrate Rotation: Binding Kinetics and Implications on Immunoassay Speed and Detection Limits. *Analytical Chemistry* **81**, 6175 (2009).
55 Li, J., Zrazhevskiy, P. & Gao, X. Eliminating Size-Associated Diffusion Constraints for Rapid On-Surface Bioassays with Nanoparticle Probes. *Small* **12**, 1035-1043, doi:10.1002/smll.201503101 (2016).

56 Uhlén, M. *et al.* Tissue-based map of the human proteome. *Science* **347**, 1260419, doi:10.1126/science.1260419 (2015).
57 Marx, V. A dream of single-cell proteomics. *Nature Methods* **16**, 809-812, doi:10.1038/s41592-019-0540-6 (2019).
58 Vogel, C. & Marcotte, E. M. Insights into the regulation of protein abundance from proteomic and transcriptomic analyses. *Nat Rev Genet* **13**, 227-232, doi:10.1038/nrg3185 (2012).
59 Maier, T., Güell, M. & Serrano, L. Correlation of mRNA and protein in complex biological samples. *FEBS Letters* **583**, 3966-3973, doi:10.1016/j.febslet.2009.10.036 (2009).
60 Couvillion, S. P. *et al.* New mass spectrometry technologies contributing towards comprehensive and high throughput omics analyses of single cells. *Analyst* **144**, 794-807, doi:10.1039/C8AN01574K (2019).
61 Janetzki, S. *et al.* Guidelines for the automated evaluation of Elispot assays. *Nature Protocols* **10**, 1098-1115, doi:10.1038/nprot.2015.068 (2015).
62 Luan, J. *et al.* Ultrabright fluorescent nanoscale labels for the femtomolar detection of analytes with standard bioassays. *Nature Biomedical Engineering*, doi:10.1038/s41551-020-0547-4 (2020).
63 Kim, Y. *et al.* Ultrabright plasmonic fluor nanolabel-enabled detection of a urinary ER stress biomarker in autosomal dominant tubulointerstitial kidney disease. *American Journal of Physiology-Renal Physiology* **321**, F236-F244, doi:10.1152/ajprenal.00231.2021 (2021).
64 Liu, L. *et al.* Plasmonically Enhanced CRISPR/Cas13a-Based Bioassay for Amplification-Free Detection of Cancer-Associated RNA. *Advanced Healthcare Materials* **n/a**, 2100956, doi:https://doi.org/10.1002/adhm.202100956 (2021).
65 Wang, Z. *et al.* Microneedle patch for the ultrasensitive quantification of protein biomarkers in interstitial fluid. *Nature Biomedical Engineering* **5**, 64-76, doi:10.1038/s41551-020-00672-y (2021).
66 Bardhan, R., Grady, N. K., Cole, J. R., Joshi, A. & Halas, N. J. Fluorescence Enhancement by Au Nanostructures: Nanoshells and Nanorods. *ACS Nano* **3**, 744-752, doi:10.1021/nn900001q (2009).
67 Luan, J. *et al.* Add-on plasmonic patch as a universal fluorescence enhancer. *Light: Science & Applications* **7**, 29, doi:10.1038/s41377-018-0027-8 (2018).
68 Abadeer, N. S., Brennan, M. R., Wilson, W. L. & Murphy, C. J. Distance and Plasmon Wavelength Dependent Fluorescence of Molecules Bound to Silica-Coated Gold Nanorods. *ACS Nano* **8**, 8392-8406, doi:10.1021/nn502887j (2014).
69 Khatua, S. & Orrit, M. Probing, Sensing, and Fluorescence Enhancement with Single Gold Nanorods. *The Journal of Physical Chemistry Letters* **5**, 3000-3006, doi:10.1021/jz501253j (2014).
70 Gandra, N. *et al.* Probing Distance-Dependent Plasmon-Enhanced Near-Infrared Fluorescence Using Polyelectrolyte Multilayers as Dielectric Spacers. *Angewandte Chemie International Edition* **53**, 866-870, doi:10.1002/anie.201308516 (2014).
71 Lu, X., Ye, G., Punj, D., Chiechi, R. C. & Orrit, M. Quantum Yield Limits for the Detection of Single-Molecule Fluorescence Enhancement by a Gold Nanorod. *ACS Photonics* **7**, 2498-2505, doi:10.1021/acsphotonics.0c00803 (2020).

72 Murphy, T. W., Zhang, Q., Naler, L. B., Ma, S. & Lu, C. Recent advances in the use of microfluidic technologies for single cell analysis. *Analyst* **143**, 60-80, doi:10.1039/C7AN01346A (2018).
73 Chiu, D. T. *et al.* Small but Perfectly Formed? Successes, Challenges, and Opportunities for Microfluidics in the Chemical and Biological Sciences. *Chem* **2**, 201-223, doi:https://doi.org/10.1016/j.chempr.2017.01.009 (2017).
74 Juan-Colás, J., Hitchcock, I. S., Coles, M., Johnson, S. & Krauss, T. F. Quantifying single-cell secretion in real time using resonant hyperspectral imaging. *Proceedings of the National Academy of Sciences* **115**, 13204, doi:10.1073/pnas.1814977115 (2018).
75 Zhou, Y. *et al.* Evaluation of Single-Cell Cytokine Secretion and Cell-Cell Interactions with a Hierarchical Loading Microwell Chip. *Cell Reports* **31**, 107574, doi:https://doi.org/10.1016/j.celrep.2020.107574 (2020).
76 Armbrecht, L. *et al.* Quantification of Protein Secretion from Circulating Tumor Cells in Microfluidic Chambers. *Advanced Science* **7**, 1903237, doi:10.1002/advs.201903237 (2020).
77 Chen, Z. *et al.* Multiplexed, Sequential Secretion Analysis of the Same Single Cells Reveals Distinct Effector Response Dynamics Dependent on the Initial Basal State. *Advanced Science* **6**, 1801361, doi:10.1002/advs.201801361 (2019).
78 Li, X. *et al.* Label-Free Optofluidic Nanobiosensor Enables Real-Time Analysis of Single-Cell Cytokine Secretion. *Small* **14**, 1800698, doi:https://doi.org/10.1002/smll.201800698 (2018).
79 Bounab, Y. *et al.* Dynamic single-cell phenotyping of immune cells using the microfluidic platform DropMap. *Nature Protocols* **15**, 2920-2955, doi:10.1038/s41596-020-0354-0 (2020).
80 Jammes, F. C. & Maerkl, S. J. How single-cell immunology is benefiting from microfluidic technologies. *Microsystems & Nanoengineering* **6**, 45, doi:10.1038/s41378-020-0140-8 (2020).
81 Hassanzadeh-Barforoushi, A., Warkiani, M. E., Gallego-Ortega, D., Liu, G. & Barber, T. Capillary-assisted microfluidic biosensing platform captures single cell secretion dynamics in nanoliter compartments. *Biosensors and Bioelectronics* **155**, 112113, doi:https://doi.org/10.1016/j.bios.2020.112113 (2020).
82 Choi, J. R. Advances in single cell technologies in immunology. *BioTechniques* **69**, 226-236, doi:10.2144/btn-2020-0047 (2020).
83 Albrecht, V., Hofer, T. P. J., Foxwell, B., Frankenberger, M. & Ziegler-Heitbrock, L. Tolerance induced via TLR2 and TLR4 in human dendritic cells: role of IRAK-1. *BMC Immunology* **9**, 69, doi:10.1186/1471-2172-9-69 (2008).
84 Efros, A. L. & Nesbitt, D. J. Origin and control of blinking in quantum dots. *Nature Nanotechnology* **11**, 661-671, doi:10.1038/nnano.2016.140 (2016).
85 Yuan, G., Gómez, D. E., Kirkwood, N., Boldt, K. & Mulvaney, P. Two Mechanisms Determine Quantum Dot Blinking. *ACS Nano* **12**, 3397-3405, doi:10.1021/acsnano.7b09052 (2018).
86 Nickel, W. & Rabouille, C. Mechanisms of regulated unconventional protein secretion. *Nature Reviews Molecular Cell Biology* **10**, 148-155, doi:10.1038/nrm2617 (2009).
87 Evavold, C. L. *et al.* The Pore-Forming Protein Gasdermin D Regulates Interleukin-1 Secretion from Living Macrophages. *Immunity* **48**, 35-44.e36, doi:10.1016/j.immuni.2017.11.013 (2018).

88 Gritsenko, A. *et al.* Priming Is Dispensable for NLRP3 Inflammasome Activation in Human Monocytes In Vitro. *Frontiers in Immunology* **11**, doi:10.3389/fimmu.2020.565924 (2020).
89 Joshi, H. *et al.* L-plastin enhances NLRP3 inflammasome assembly and bleomycin-induced lung fibrosis. *Cell Reports* **38**, doi:10.1016/j.celrep.2022.110507 (2022).
90 Langenkamp, A., Messi, M., Lanzavecchia, A. & Sallusto, F. Kinetics of dendritic cell activation: impact on priming of TH1, TH2 and nonpolarized T cells. *Nature Immunology* **1**, 311-316, doi:10.1038/79758 (2000).
91 Chang, H.-H. & Murphy, C. J. Mini Gold Nanorods with Tunable Plasmonic Peaks beyond 1000 nm. *Chemistry of Materials* **30**, 1427-1435, doi:10.1021/acs.chemmater.7b05310 (2018).
92 Toniolo, C., Rutschmann, O. & McKinney, J. D. Do chance encounters between heterogeneous cells shape the outcome of tuberculosis infections? *Curr Opin Microbiol* **59**, 72-78, doi:10.1016/j.mib.2020.08.008 (2020).
93 Chattopadhyay, P. K., Gierahn, T. M., Roederer, M. & Love, J. C. Single-cell technologies for monitoring immune systems. *Nature immunology* **15**, 128-135, doi:10.1038/ni.2796 (2014).
94 Ashouri, J. F. & Weiss, A. Endogenous Nur77 Is a Specific Indicator of Antigen Receptor Signaling in Human T and B Cells. *J Immunol* **198**, 657-668, doi:10.4049/jimmunol.1601301 (2017).
95 Tamura, T. *et al.* The role of antigenic peptide in CD4+ T helper phenotype development in a T cell receptor transgenic model. *International immunology* **16**, 1691-1699, doi:10.1093/intimm/dxh170 (2004).
96 Streeck, H., Frahm, N. & Walker, B. D. The role of IFN-γ Elispot assay in HIV vaccine research. *Nature Protocols* **4**, 461-469, doi:10.1038/nprot.2009.7 (2009).
97 Malyguine, A. M., Strobl, S., Dunham, K., Shurin, M. R. & Sayers, T. J. ELISPOT Assay for Monitoring Cytotoxic T Lymphocytes (CTL) Activity in Cancer Vaccine Clinical Trials. *Cells* **1**, 111-126, doi:10.3390/cells1020111 (2012).
98 Saletti, G., Çuburu, N., Yang, J. S., Dey, A. & Czerkinsky, C. Enzyme-linked immunospot assays for direct ex vivo measurement of vaccine-induced human humoral immune responses in blood. *Nature Protocols* **8**, 1073-1087, doi:10.1038/nprot.2013.058 (2013).
99 Pai, M. *et al.* Gamma Interferon Release Assays for Detection of Mycobacterium tuberculosis Infection. *Clinical Microbiology Reviews* **27**, 3, doi:10.1128/CMR.00034-13 (2014).
100 Adetifa, I. M. *et al.* Interferon-γ ELISPOT as a Biomarker of Treatment Efficacy in Latent Tuberculosis Infection. *American Journal of Respiratory and Critical Care Medicine* **187**, 439-445, doi:10.1164/rccm.201208-1352OC (2013).
101 Pan, L. *et al.* Risk factors for false-negative T-SPOT.TB assay results in patients with pulmonary and extra-pulmonary TB. *Journal of Infection* **70**, 367-380, doi:https://doi.org/10.1016/j.jinf.2014.12.018 (2015).
102 Joshi, H. & Morley, S. C. Cells under stress: The mechanical environment shapes inflammasome responses to danger signals. *Journal of Leukocyte Biology* **106**, 119-125, doi:10.1002/jlb.3mir1118-417r (2019).

103 Bai, B. *et al.* NLRP3 inflammasome in endothelial dysfunction. *Cell Death & Disease* **11**, 776, doi:10.1038/s41419-020-02985-x (2020).
104 Altschuler, S. J. & Wu, L. F. Cellular Heterogeneity: Do Differences Make a Difference? *Cell* **141**, 559-563, doi:10.1016/j.cell.2010.04.033 (2010).
105 Heath, J. R., Ribas, A. & Mischel, P. S. Single-cell analysis tools for drug discovery and development. *Nature Reviews Drug Discovery* **15**, 204-216, doi:10.1038/nrd.2015.16 (2016).
106 Mastrogiovanni, M., Di Bartolo, V. & Alcover, A. Cell polarity regulators, multifunctional organizers of lymphocyte activation and function. *Biomedical Journal*, doi:https://doi.org/10.1016/j.bj.2021.10.002 (2021).
107 Avraham, R. *et al.* Pathogen Cell-to-Cell Variability Drives Heterogeneity in Host Immune Responses. *Cell* **162**, 1309-1321, doi:10.1016/j.cell.2015.08.027 (2015).
108 Lin, P. L. *et al.* Sterilization of granulomas is common in active and latent tuberculosis despite within-host variability in bacterial killing. *Nat Med* **20**, 75-79, doi:10.1038/nm.3412 (2014).
109 Logsdon, M. M. & Aldridge, B. B. Stable Regulation of Cell Cycle Events in Mycobacteria: Insights From Inherently Heterogeneous Bacterial Populations. *Frontiers in Microbiology* **9**, doi:10.3389/fmicb.2018.00514 (2018).
110 Thampy, L. K. *et al.* Restoration of T Cell function in multi-drug resistant bacterial sepsis after interleukin-7, anti-PD-L1, and OX-40 administration. *PLOS ONE* **13**, e0199497, doi:10.1371/journal.pone.0199497 (2018).
111 Moran, A. E. *et al.* T cell receptor signal strength in Treg and iNKT cell development demonstrated by a novel fluorescent reporter mouse. *J Exp Med* **208**, 1279-1289, doi:10.1084/jem.20110308 (2011).
112 <2011_Book_FlowCytometryProtocols.pdf>.
113 Maecker, H. T., Frey, T., Nomura, L. E. & Trotter, J. Selecting fluorochrome conjugates for maximum sensitivity. *Cytometry A* **62**, 169-173, doi:10.1002/cyto.a.20092 (2004).
114 Hulspas, R., O'Gorman, M. R., Wood, B. L., Gratama, J. W. & Sutherland, D. R. Considerations for the control of background fluorescence in clinical flow cytometry. *Cytometry B Clin Cytom* **76**, 355-364, doi:10.1002/cyto.b.20485 (2009).
115 Flores-Montero, J. *et al.* Fluorochrome choices for multi-color flow cytometry. *J Immunol Methods* **475**, 112618, doi:10.1016/j.jim.2019.06.009 (2019).
116 Hedley, B. D. & Keeney, M. Technical issues: flow cytometry and rare event analysis. *Int J Lab Hematol* **35**, 344-350, doi:10.1111/ijlh.12068 (2013).
117 Kishimoto, T. The biology of interleukin-6. *Blood* **74**, 1-10, doi:10.1182/blood.V74.1.1.1 (1989).
118 Dower, S. K. *et al.* Detection and characterization of high affinity plasma membrane receptors for human interleukin-1. *Journal of Experimental Medicine* **162**, 501 (1985).
119 Liu, J. *et al.* Interleukin-12: an update on its immunological activities, signaling and regulation of gene expression. *Current Immunology Review* **1**, 119 (2005).
120 Chattopadhyay, P. K. Quantum dot technology in flow cytometry. *Methods Cell Biol* **102**, 463-477, doi:10.1016/B978-0-12-374912-3.00018-3 (2011).
121 Reiss, P., Bleuse, J. & Pron, A. Highly Luminescent CdSe ZnSe core shell nanostructures of low size dispersion. *Nano Letters* **2**, 781 (2002).
122 Michalet, X. *et al.* Quantum Dots for Live Cells, in Vivo Imaging, and Diagnostics. *Science* **307**, 538 (2005).

123 Cheng, Y., Ling, S. D., Geng, Y., Wang, Y. & Xu, J. Microfluidic synthesis of quantum dots and their applications in bio-sensing and bio-imaging. *Nanoscale Adv* **3**, 2180-2195, doi:10.1039/d0na00933d (2021).
124 Gebhardt, C., Lehmann, M., Reif, M. M., Zacharias, M. & Cordes, T. Molecular and spectroscopic characterization of green and red cyanine fluorophores from the Alexa Fluor and AF series. doi:10.1101/2020.11.13.381152 (2020).
125 Cheng, D. & Xu, Q. H. Separation distance dependent fluorescence enhancement of fluorescein isothiocyanate by silver nanoparticles. *Chem Commun (Camb)*, 248-250, doi:10.1039/b612401a (2007).
126 Dulkeith, E., Ringler, M., Klar, T. A. & Feldman, J. Gold nanoparticles quench fluorescence by phase induced raditative rate suppression. *Nano Letters* **5**, 585 (2005).
127 Albert, M. L., Jegathesan, M. & Darnell, R. B. Dendritic cell maturation is required for the cross-tolerization of CD8+ T cells. *Nat Immunol* **2**, 1010-1017, doi:10.1038/ni722 (2001).
128 Gilboa, E. DC-based cancer vaccines. *J Clin Invest* **117**, 1195-1203, doi:10.1172/JCI31205 (2007).
129 Jin, P. *et al.* Molecular signatures of maturing dendritic cells implications for testing the quality of dendritic cell therapies. *Journal of Translational Medicine* **8** (2010).
130 Selecting Reagents for Multicolor Flow.
131 Arnspang, E. C., Brewer, J. R. & Lagerholm, B. C. Multi-color single particle tracking with quantum dots. *PLoS One* **7**, e48521, doi:10.1371/journal.pone.0048521 (2012).
132 Brando, B. & Sommaruga, E. Nationwide quality control trial on lymphocyte immunophenotyping and flow cytometer performance in Italy. *Cytometry* **14**, 294-306, doi:10.1002/cyto.990140310 (1993).
133 Dependence of the Enhanced Optical Scattering Efficiency Relative to That of Absorption for Gold Metal Nanorods on Aspect Ratio, Size, End-Cap Shape, and Medium Refractive Index.

Curriculum Vitae

PRIYA RATHI

Department of Chemistry

McDonnell International Scholars Academy

Soft Nanomaterials Lab

Washington University in St. Louis

priya.rathi@wustl.edu

EDUCATION

WASHINGTON UNIVERSITY IN ST. LOUIS (WashU) St. Louis, USA

Doctor of Philosophy (Ph.D.) in Chemistry,

PI: Dr. Srikanth Singamaneni *Aug 2017 – present*

Soft Nanomaterials group

INDIAN INSTITUTE OF TECHNOLOGY BOMBAY (IITB) Mumbai, India

Master of Science (MS) in Chemistry *Aug 2014 – Dec 2016*

ST. STEPHEN'S COLLEGE, DELHI UNIVERSITY New Delhi, India

Bachelor of Science (BS) with honors in Chemistry *Aug 2010 – May 2013*

WASHINGTON UNIVERSITY IN ST. LOUIS St. Louis, MO

Peer-reviewed publications:

(In order of preparation and submission)

1. **Rathi, P.**; Gupta, P.; Debnath, A.; Wang, Y.; Morrissey, J. J.; Raman, B.; Singamaneni, S., (**2022)** Plasmonic-fluor-enhanced Expansion Microscopy. *In preparation*
2. **Rathi, P.**; Seth, A.; Gupta, R.; Gupta, P.; Wang, Y.; Morrissey, J. J.; Brestoff, J.; Singamaneni, S., (**2022**) Plasmon-enhanced Flow Cytometry. *In preparation*
3. **Rathi, P.**; Feit, C.; Pathirana, S.; Gupta, P.; Wang, Y.; Baldi, H.; Banerjee, P.; Singamaneni, S., (**2022)** Ultra-thin, Free-standing, Atomic Layer Deposited ZnO Films. *In preparation*
4. Gupta, P.; **Rathi, P.**; Gupta, R.; Baldi, H.; Coquerel, Q.; Debnath, A.; Derami, H. G.; Raman, B.; Singamaneni, S., (**2022**) Neuronal Maturation-dependent Nano-Neuro Interaction and Modulation. *Submitted to Neuron*
5. Feit, C.; **Rathi, P.**; Singamaneni, S.; Banerjee, P. (**2022**) Hot Electron Generation in Plasmoresistor Devices Fabricated via Area-selective Atomic Layer Deposition. *In preparation*
6. Seth, A.; Mittal, E.; Luan, J.; Kolla, S.; Mazer, M. B.; Joshi, H.; Gupta, R.; **Rathi, P.**; Wang, Z.; Morrissey, J. J.; Ernst, J. D.; Portal-Celhay, C.; Morley, S. C.; Philips, J. A.; Singamaneni, S., (**2022)** High-resolution imaging of protein secretion at the single-cell level using plasmon-enhanced FluoroDOT assay. *Cell Reports Methods**,** 2* (8), 100267.
7. Wang, Z.; Zhou, Q.; Seth, A.; Kolla, S.; Luna, J.; Jiang, Q.; **Rathi, P.**; Gupta, P.; Morrissey, J. J.; Singamaneni, S. (**2022**) Plasmonically-enhanced competitive assay for ultrasensitive and multiplexed detection of small molecules. *Biosensors and Bioelectronics* 200, 113918, doi:10.1016/j.bios.2021.113918
8. Wang, Z.; Luan, J.; Seth, A.; Liu, L.; You, M.; Gupta, P.; **Rathi, P.**; Wang, Y.; Cao, S.; Jiang, Q.; Zhang, X.; Gupta, R.; Zhou, Q.; Morrissey, J. J.; Scheller, E. L.; Rudra, J. S.,

Singamaneni, S. (2021) Microneedle patch for the ultrasensitive quantification of protein biomarkers in interstitial fluid. *Nature Biomedical Engineering* 5, 64-76, doi:10.1038/s41551-020-00672-y

9. Cao, S.; **Rathi, P.**; Wu, X.; Ghim, D.; Jun, Y. S.; Singamaneni, S., (**2021)** Cellulose Nanomaterials in Interfacial Evaporators for Desalination: A "Natural" Choice. *Advanced Materials***,** *33* (28), e2000922.
10. Seth, A.; Gupta, R.; Wang, Z.; Mittal, E.; Kolla, S.; King, M.; **Rathi, P.**; Schmitz, A. J.; Pappu, R.; Vahey, M.; Ellebedy, A. H.; Fremont, D. H.; Parikh, A. B.; Genin, G. M.; Gandra, S.; Storch, G. A.; Philips, J. A.; George, I. A.; Singamaneni, S., (**2021)** Digital Plasmonic Fluoroimmunoassay for Sub-femtomolar Detection of Protein 1 Biomarkers, with Application to SARS-CoV-2 Variants.
11. Luan, J.; Seth, A.; Gupta, R.; Wang, Z.; **Rathi, P.**; Cao, S.; Gholami Derami, H.; Tang, R.; Xu, B.; Achilefu, S.; Morrissey, J. J.; Singamaneni, S., (**2020)** Ultrabright fluorescent nanoscale labels for the femtomolar detection of analytes with standard bioassays. *Nature Biomedical Engineering*, *4* (5), 518-530.
12. Seth, A.; Gholami Derami, H.; Gupta, P.; Wang, Z.; **Rathi, P.**; Gupta, R.; Cao, T.; Morrissey, J. J.; Singamaneni, S., (**2020**) Polydopamine-Mesoporous Silica Core-Shell Nanoparticles for Combined Photothermal Immunotherapy. *ACS Applied Materials and Interfaces*, *12* (38), 42499-42510.
13. Gholami Derami, H.; Gupta, P.; Gupta, R.; **Rathi, P.**; Morrissey, J. J.; Singamaneni, S., (**2020**) Palladium Nanoparticle-Decorated Mesoporous Polydopamine/Bacterial Nanocellulose as a Catalytically Active Universal Dye Removal Ultrafiltration Membrane. *ACS Applied Nano Materials***,** *3* (6), 5437-5448.

14. **Rathi, P.**; Jha, M. K.; Hata, K.; Subramaniam, C., Real-Time, Wearable, Biomechanical Movement Capture of Both Humans and Robots with Metal-Free Electrodes. *ACS Omega* **2017,** *2* (8), 4132-4142.

Presentations:

1. **Rathi, P.**; Epstein, J.; Gupta, P.; Gupta, R.; Seth, A.; Singamaneni, S., Overcoming the diffusion-limited kinetics of fluorescent nano-labels for rapid and ultrasensitive bio-detection, **ACS 2022**, Micro-and Nanosystems for Biology and Medicine
2. **Rathi, P.**; Feit, C.; Pathirana, S.; Gupta, P.; Wang, Y.; Baldi, H.; Banerjee, P.; Singamaneni, S., Ultra-thin, free-standing atomic layer deposited ZnO films, **ACS 2022**, Chemistry of Materials – Nanomaterials
3. **Rathi, P.**; Gupta, P.; Debnath, A.; Wang, Y.; Morrissey, J. J.; Raman, B.; Singamaneni, S., Plasmonic-fluor-enhanced Expansion Microscopy, **PhD in 3D 2022**, WashU-MISA